Atomic Level Study of Structural Changes of TiO_2 Based Photocatalysts During Solar Water Splitting Reactions Using TEM

by

Liuxian Zhang

A Dissertation Presented in Partial Fulfillment
of the Requirements for the Degree
Doctor of Philosophy

Approved November 2015 by the
Graduate Supervisory Committee:

Peter Crozier, Chair
David Smith
Candace Chan
Jingyue Liu

ARIZONA STATE UNIVERSITY

December 2015

ABSTRACT

Photocatalytic water splitting is a promising technique to produce H_2 fuels from water using sustainable solar energy. To better design photocatalysts, the understanding of charge transfer at surfaces/interfaces and the corresponding structure change during the reaction is very important. Local structural and chemical information on nanoparticle surfaces or interfaces can be achieved through characterizations on transmission electron microscopy (TEM). Emphasis should be put on materials structure changes during the reactions in their "working conditions". Environmental TEM with *in situ* light illumination system allows the photocatalysts to be studied under light irradiation when exposed to H_2O vapor. A set of *ex situ* and *in situ* TEM characterizations are carried out on typical types of TiO_2 based photocatalysts. The observed structure changes during the reaction are correlated with the H_2 production rate for structure-property relationships.

A surface disordering was observed *in situ* when well-defined anatase TiO_2 rhombohedral nanoparticles were exposed to 1 Torr H_2O vapor and 10suns light inside the environmental TEM. The disordering is believed to be related to high density of hydroxyl groups formed on surface oxygen vacancies during water splitting reactions.

Pt co-catalyst on TiO_2 is able to split pure water producing H_2 and O_2. The H_2 production rate drops during the reaction. Particle size growth during reaction was discovered with Z-contrast images. The particle size growth is believed to be a photo-electro-chemical Ostwald ripening.

Characterizations were also carried out on a more complicated photocatalyst system: Ni/NiO core/shell co-catalyst on TiO_2. A decrease of the H_2 production rate resulting from photo-corrosion was observed. The Ni is believed to be oxidized to Ni^{2+} by OH ·radicals which are intermediate products of H_2O oxidation. The mechanism that the OH ·radicals leak into the cores through cracks on NiO shells is more supported by experiments.

Overall this research has done a comprehensive *ex situ* and *in situ* TEM characterizations following some typical TiO_2 based photocatalysts during reactions. This research has shown the technique availability to study photocatalyst inside TEM in photocatalytic conditions. It also demonstrates the importance to follow structure changes of materials during reactions in understanding deactivation mechanisms.

DEDICATION

This thesis is dedicated to my parents, my girfriend, my friends for their support and encouragement.

ACKNOWLEDGMENTS

I thank my advisor, Dr. Peter A. Crozier, for providing me the opportunity to train myself with not only knowledge and skills but also rigorous attitude and cautious research manners. I am very grateful for all his patient guidance and high standard requirements throughout my Ph.D.

I would like to thank my committee members, Dr. Candace Chan, Dr. David Smith, Dr. Jingyue Liu, for their valuable suggestions. I would also like to thank Dr Karl Sieradzki for valuable advice on content of chapter 4 in this thesis. I also appreciate all the help from the Crozier group members. I'm very grateful for Benjamin K. Miller's contribution designing the *in-situ* light illumination system without which all the in-situ characterization in this thesis would not be possible. Adam Pocock has helped me with experiments in Chapter 5 and Chapter 6. I also appreciate Qianlang Liu's help in some of the experiments and valuable discussions.

I am grateful for the help I got from all the staff in John M. Cowley Center for High Resolution Electron Microscopy and LeRoy Eyring Center for Solid State Science. The use of experiment instruments in these facilities is gratefully acknowledged.

The financial support provided by the US Department of Energy grant DE-SC0004954 is gratefully acknowledged.

Finally, I would like to thank my parents, my girlfriend and my friends for encouraging me at some of the depressing moments during my Ph.D.

TABLE OF CONTENTS

LIST OF TABLES

TABLE Page

LIST OF FIGURES

FIGURE Page

FIGURE Page

FIGURE Page

FIGURE Page

CHAPTER 1

GENERAL INRODUCTION

1.1 Introduction to Photocatalytic Water Splitting.

The generation of secure, sustainable and clean energy has been widely accepted as one of the most important scientific and technical challenge in this new century. With a continuously increasing population and economy, total primary energy consumption is projected to grow by 8.6 quadrillion Btu (8.9%), from 97.1 quadrillion Btu in 2013 to 105.7 quadrillion Btu in 2040. Most of the energy consumption is still from fossil fuels, coal, oil and natural gas. The growth of the energy consumption is in natural gas and renewables, while renewables contribute less than 10% to the total consumption [1]. Even though the abundance of fossil fuels is sufficient to meet the demand for this century, the cumulative CO_2 as the product of combustions of fossil fuels brings climate change problems [2, 3]. In addition to this, pollution from impurities in fossil fuels like sulfur oxide and nitric oxide also drive the demand for clean energy sources.

Among all the clean renewable energy sources, solar energy is the most abundant but the least utilized source so far. The demand of large solar harvesting areas and the high cost to manufacturer high efficiency thin-film solar panels limit solar electricity's ability to compete with electricity generated by conventional power sources [4]. Besides, solar electricity generated in remote areas has to be transferred without much loss. The electricity has to be stored for night usage which demands reliable and efficient energy storage systems. To find a sustainable fuel source is compatible to today society's energy

consumption system which depends on combustion of fuels. Converting solar energy directly into chemical energy stored in fuels is one of the most promising techniques to overcome those difficulties for producing fuels with sustainable solar energy.

There are several techniques to produce fuels in sustainable pathways. The one that has been mostly commercialized is biofuels.[1] Biofuels are produced mainly from plants through agriculture anaerobic digestion process. They are hydrocarbon-based fuels and the combustion of these fuels still releases CO_2. However, CO_2 in the atmosphere will be retaken into the biological cycles when growing plants for biofuels production. Traditional biofuel production through crops has a large impact on agriculture through large usage of farm land, fertilizer and water. Alternatively, algae has become promising with advantages of easy growth and much less impact on agriculture [5, 6]. However, there is still a long way to go to have algae as a commercial available source of biofuels before algae can be efficiently grown in a comparatively large scale to meet the energy need.

Another pathway includes solar water splitting for H_2 production. H_2 has very high energy density compared to other fuels and is completely clean energy source with H_2O the only combustion product [7]. H_2 fuels generated from solar energy can be transferred easily and consumed anywhere anytime. Solar water splitting can be realized by different techniques: thermal-chemical process, photo-voltaic (PV)/electrolyser, photoelectrochemical cells and photocatalysts. A thermal-chemical water splitting process can be carried out to produce hydrogen and oxygen at 500-2000 ℃ temperatures gained from concentrated solar light or waste heat of nuclear power stations. With the

help of reducible oxide materials like $Ce(IV)O_2/Ce(III)_2O_3$, O_2 and H_2 can be released during the oxygen depletion/refill cycles on the materials when being heated up to 2000 ℃ and cooled down to 500 ℃. The durability of the reactant materials and the design of safe and reliable high-temperature reactors are the main engineering challenges for this technique [8].

Solar water splitting can also be done through the electricity produced by photo-voltaic panels. PV modules are coupled to electrolyser to provide voltage for H_2 and O_2 generation. The generic electrolyser requires an ideal 1.9V for water splitting which gives a maximum efficiency 1.23/1.9=65% conversion at the electrolyser [9]. The final solar to hydrogen efficiency would be the PV efficiency times this 64%. For a multicrystalline Si PV/electrolysis system, 9% solar to hydrogen efficiency is expected. Solar water splitting can alternatively be done without the step of electrolyser. A semiconductor can be directly used as an electrode to take photons generating electrons and holes for redox reactions in electrolyte. The electrons or holes are transferred through connections to the counter electrode made with a metal or another semiconductor to do the other half reaction. This technique is called photoelectrochemical cell water splitting. Or it can be even simplified by using photocatalyst nanomaterials where electron-hole pairs are generated on the semiconductor material and diffused to some sites of the material for hydrogen evolution and another sites for oxygen evolution. Compared to PEC and PV+electrolyser, the photocatalyst nanoparticle suspension technique is much less expensive.[10] The PEC or photocatalytic water splitting techniques put high

requirements on semiconductor materials stability, bandgaps, band positions and catalytic properties.

It was first discovered in 1972 that semiconductors like TiO_2 can take photons and generate electron-hole pairs which can be used for reduction/oxidation of H_2O producing H_2 and O_2 [11]. The reactions can be done at much lower temperatures thus in a safer circumstance. It does not need sophisticated design of reactors and mirrors. However, the most stable and efficient photocatalysts discovered so far are very much limited to UV light absorption. The commercialization of this technique depends on the efficiency of the photocatalyst to utilize larger range of solar light. This thesis is focused on understanding some fundamental science problems in photocatalyst during photocatalytic reactions.

1.1.1 Mechanism of Semiconductor Photocatalytic Water Splitting

The mechanism of photocatalytic water splitting is illustrated in Figure 1.1.

$$2H_2O \xleftrightarrow{photon\ energy > 1.23ev} 2H_2 + O_2$$

When a photon is absorbed by a photocatalyst semiconductor, an electron is excited into conduction band leaving a hole in the valence band. Photoexcited electrons and holes are then taken to reduce H^+ to H_2 and oxidize OH^- to O_2 respectively. The band gap of the semiconductor which can do photocatalytic water splitting has to be larger than 1.23eV, the energy difference between the hydrogen reduction level E_{H_2/H_2O} and the water oxidation level E_{H_2O/O_2} [12]. The bottom of the conduction band of the semiconductor

has to be more negative than E_{H_2/H_2O} and the top of the valence band has to be more positive than E_{H_2O/O_2}. Besides the requirements of band structure, the semiconductors used as photocatalysts have to be stable in water under photoreaction conditions. For example, CdS with proper band structure cannot be used directly as a photocatalyst without hole scavengers because of photo-corrosion issue: $CdS+h^+ \rightarrow Cd^{2+}+S$ [13]. Metal-oxide semiconductors such as TiO_2 are widely researched as photocatalysts for its abundance and stability. The main difficulties restricting photocatalyst from high energy conversion rates are [14]:

i. High e-h recombination rate: electron and hole pairs generated from photon excitation can recombine very fast if not separated efficiently and taken by absorbates for redox reactions.

ii. High back reaction rate: H_2 and O_2 produced from water splitting is thermodynamically preferred to recombine forming H_2O again. It is critical to have H_2 and O_2 produced at different sites and separated efficiently.

iii. Most of the stable photocatalyst substrates are metal oxide which have large band gaps only taking UV light. Solar energy utilization is low if the photocatalyst can only work in UV range. According to Shockley-Queisser limit, the theoretical maximum solar conversion efficiency of a semiconductor with bandgap 3.0 eV is only about 5%. Even within this 5%, only 1.23eV/3eV is converted into producing H_2 and O_2 making the efficiency too low. A photocatalyst with proper bandgap closer to the 1.23eV will dramatically increase the solar conversion efficiency.

Regarding the issues mentioned above, different techniques have been developed to better modify photocatalysts towards real industry applications. TiO_2, as one of the most stable and abundant oxide semiconductors, shows relatively good photocatalyst properties in UV range. It has been widely accepted as basic photocatalyst for further modification to overcome the issues mentioned above. The following discussion will be focused on TiO_2 and modifications to TiO_2 as typical examples of major methods to improve efficiency of photocatalysts for H_2 production.

1.1.2 Photocatalyst Modification Techniques.

One of the key factors influencing catalysts' properties is surface area. Small particles with high surface area to volume ratios help absorb reactants at high surface energy sites. Besides, electron-hole pairs travel less distance to reactants reducing the chance of recombination. Wang et al discovered an increase of photocatalytic activity of TiO_2 with particle size dropping from 21nm to 11nm and a decrease of activity with further size decrease from 11nm to 6nm [15,16]. Their explanation was that small particle size helps reduce bulk e-h recombination while too small particle size results in surface e-h re-combination happening much faster than interfacial charge transfer from TiO_2 to reactants.

Innovative nanostructures including mesoporous TiO_2, TiO_2 nanowires and TiO_2 nanotubes have been prepared to achieve better performance of TiO_2 photocatalysts. Gong et al. developed the technique of potentiostatic anodization of titanium to prepare highly ordered, vertically oriented TiO_2 nanotube-arrays - a material architecture that offers a large internal surface area without decrease in geometric and structural order

[17]. Liu et al. fabricated the innovative TiO_2 nanorods grown on transparent conductive glass fluorine-doped tin oxide (FTO) using a hydrothermal method [18]. This 1-dimensional highly oriented nanostructure on conductive glass substrate is suitable for electro-photocatalytical water splitting and allows light illumination from the back side of the electrode close to the connections.

Besides the innovation of novel nanostructures, TiO_2 is also commonly coupled with metal co-catalysts for better photocatalytic properties. As shown in Figure 1.2, a metal co-catalyst is believed to help attract photo-generated electrons therefore reducing e-h re-combinations [19]. The metal particles, such as Pt, also act as reduction catalysts via electron transfer to adsorbed protons, reducing them to H_2 which then desorbs from the surface [20]. Anpo et al. have applied electron spin resonance (ESR) to study the electrons transferred from TiO_2 to Pt. It was found that the amount of Ti^{3+} is increased if there is no loading of Pt. The loading of Pt absorbs photo-excited electrons from TiO_2 preventing reduction of Ti^{4+} [21]. Usually noble metals such as Pt, Au and Pd work the best as metal co-catalyst because of the work function, electron affinity and hydrogen absorption/desorption energy [22]. Efforts have been put into developing less expensive metal co-catalyst like Cu and Ag [23, 24].

Semiconductor coupling is also used to better separate the electron-hole pairs and utilize visible light for hydrogen generation. A common design is to have TiO_2 coupled with a smaller band-gap semiconductor which has a more negative conduction band. The electrons excited in small bandgap semiconductor will be transferred to TiO_2 conduction band and therefore separated from recombination. For example, So et al. have applied CdS/TiO_2 composite semiconductor for photocatalytic hydrogen production [25].

However, most of the small band-gap semiconductors are not resistant to photocorrosions. Hole scavengers like Na_2S have to be added to protect the CdS from photocorrosion [13]. Another example for the semiconductor coupling is TiO_2 coupled to SiC and WO_3 [26]. Excited electrons are transferred from SiC to TiO_2 and then to WO_3 according to their conduction band positions. Even though the semiconductor composites show an increase in the photocatalytic oxidation of methylethylketone because of charge separation efficiency, they cannot be applied for H_2 production because the CB of WO_3 is not more negative than the H_2O/H_2 redox potential.

Efforts have also been made to combine different modification techniques into one system. Domen et al. developed the Ni-NiO core-shell structure on $SrTiO_3$ semiconductors by reduction-partial oxidation method. This structure has shown enhanced H_2 production rate [27, 28]. The mechanism was later proposed to be that the protons were reduced at the Ni sites and H_2O oxidized at the NiO sites. Electrons transfer to Ni while holes transfer to NiO thus helping separate e-h pairs. Also since the H_2 and O_2 were produced at different sites, this system suppresses the back reactions [29]. Similarly, Maeda et al. prepared noble metal/Cr_2O_3 core/shell structure on $(Ga_{1-x}Zn_x)(N_{1-x}O_x)$ photocatalysts and observed enhanced water splitting under visible light [30, 31]. Yoshida et al. performed *in situ* infrared reflection absorption spectroscopy (IRAS) on electrodes prepared with noble-metal/Cr_2O_3 co-catalyst and discovered Cr_2O_3 is permeable to protons and hydrogen but not oxygen. The shell helps to prevent back reactions of H_2 and O_2 which is the reason for higher production of hydrogen [32]. Besides the innovative morphology of TiO_2, the loading of metal co-catalyst and the coupling of other semiconductors, other techniques such as dye-sensitization, doping of

ions and adding electron/hole scavengers have also been applied in an effort to improve photocatalytic properties [33-35]. All those modifications are targeted at resolving the 3 main issues about photocatalysis: e-h recombination, H_2 and O_2 back reaction, and visible light response.

1.1.3 Understanding fundamentals of photocatalysts during reactions using TEM.

While substantial improvements in performance have been realized for photocatalytic water splitting, better design of the photocatalyst requires more understanding of fundamentals in charge transfer to the catalyst surfaces or between co-catalyst/semiconductor interfaces, absorption/desorption of reactant molecules and corresponding surface structure changes. Photocatalytic properties are compared with limited discussion of materials microstructures and structure evolution during the reactions [12, 14, 36]. Domen et al. have used X-ray photoelectron spectroscopy (XPS) and extended X-ray absorption fine structure (EXAFS) to determine the NiOx compositions on $SrTiO_3$ after different heat treatment and found evidence of $Ni(OH)_2$ on the co-catalyst surface [27]. Henderson et al have used temperature programmed desorption (TPD) and high resolution electron energy loss spectrum (HREELS) to study the water absorption and dissociation on TiO_2 (110) surfaces [37]. These spectroscopy studies provided valuable information about material compositions and reactions on surfaces. Such analysis usually provide averaged information on nanomaterials but it would be useful to combine these approaches with visualization of local structural information on nanoparticles. Bikondoa et al. and Wendt et al. have performed valuable research for direct visualization of water dissociation on TiO_2 (110) using scanning tunneling microscopy (STM) [38-40]. STM research usually requires bulk single crystal

materials with flat terminated facets. Localized information, on nanoparticles with high surface, corresponding to specific facets or surface features like steps or vacancies are not available through such characterizations. Besides, these characterizations are usually done at high vacuum or with very small amount of water molecules which may not represent the real reaction conditions. Characterization using transmission electron microscope (TEM) overcomes these limitations providing localized information at the nanoscale. Environmental TEM can provide a photo-reaction conditions allowing the photocatalyst to be characterized in its "working conditions".

Considerable less work has been mentioned about materials deactivation in the review papers in this area [12, 14, 36]. Many researchers have developed new photocatalysts and tested their performance. The characterizations are emphasized on photocatalyst initial structures with less attention on structures during the reactions. This thesis summarizes comprehensive research work carried out by TEM to study typical photocatalysts during the reactions. The structure evolution during reactions were followed by *ex situ* and *in situ* TEM characterizations. The observed structure change is correlated to the photocatalytic properties of H_2 production. Working and deactivation mechanisms are revealed which shine light on a better understanding of fundamentals of photocatalytic water splitting and better design of photocatalyst.

1.2 Introduction to Environmental Transmission Electron Microscopy

Transmission electron microscope (TEM) was invented in 1932 by Ruska [41]. Since then transmission electron microscopy has been applied to achieve structural and chemical information of materials which could not be obtained by light or low energy

beams. The information that can be obtained includes not only the general microscopic morphologies like particle sizes and shapes, but also surface/interface atomic structure and chemical composition [42]. The atomic scale information at surfaces/interfaces are the most critical information for analysis of catalysts. However, the information achieved in a regular TEM at room temperature in vacuum may not be the same as the information in a reaction atmosphere. To design a better catalyst, the structure and chemical compositions of catalysts have to be studied when they are actually catalyzing reactions in "working conditions". This requires the presence of reactants and a proper temperature (enough to activate the reaction but not too high to challenge the instrument and materials stability). For photocatalysts, it also requires the light illumination. Those requirements can be met by utilizing environmental TEM (ETEM) in *in situ* experiments.

"*In-situ*" means "in the place" in Latin. In the "*in situ*" experiments, stimuli are applied to materials, the structural and chemical response of materials are characterized in the TEM. TEM sample holders are modified to introduce external stimuli such as heating, cooling, gas or liquid reactants, mechanical strains, electrical bias and light etc. [43-45]. However, due to the limited space and high stability requirement, it is an engineering challenging to apply both the reactants and more than two stimuli at a time on a single holder. Specific holders are restricted to a few specific experiments. Alternatively, TEM can also be equipped with environmental pumping cells to provide gas reactants around the sample materials. Certain temperature can be provided by hot-stage sample holders or cryo holders. For the *in situ* characterization of photocatalysts, a light illumination system was designed and attached to the environmental TEM FEI Tecnai F20 [46].

A regular TEM works in high vacuum condition (10^{-6} to 10^{-10} Torr) so as to avoid electron-gas scattering and the electron source being attacked by gas molecules. To view the *in-situ* reactions, gas reactants have to surround the TEM sample but must be confined only to the small spacing around the sample. Otherwise, gases will disturb the vacuum system and the electron gun. This configuration can be achieved by incorporating window cells into TEM sample holders [47-49]. The gas is injected from small tubes in the holder into the window cell with the TEM sample encapsulated between electron-transparent thin membranes. With this method, pressures even larger than ambient atmosphere can be achieved [50]. However, the membrane can significantly affect the quality of the high-resolution image.

An alternative technique is to build an environmental cell in the microscope around the sample stage [51-53]. As shown in Figure 1.3, the environmental cell is a special chamber which allows a certain gas pressure around the TEM sample. The electron beam goes through the pumping aperture on the upper and lower pole pieces. Gases are injected into this chamber and pumped through differential pumping systems. 20 Torr of gas can be accumulated around the sample material by controlling the pumping speed and optimizing the sizes of pumping apertures. This setup allows a reasonable gas pressures without sacrificing the spatial resolution [54, 55]. There will be some scattering of electrons by gas molecules affecting the resolution. However the effect is much smaller than the interactions with window materials for window cells. The environmental cell is usually very reliable for handling different gas atmospheres for different types of experiments. One other advantage is that gases can be sufficiently mixed before they are allowed into TEM columns with precise valves.

1.3 Outline

Chapter 2 introduces the main experimental methods used in this dissertation including the main characterization and instrumentation. Following that, examples of different types of TiO_2 based materials are discussed for their structure evolutions during the photocatalysis reactions characterized by *in situ* and *ex situ* experiments. Chapter 3 discusses the surface amorphization observed on pure TiO_2 anatase particles when exposed to H_2O vapor and light. After achievements of knowledge on basic TiO_2 materials, Pt/TiO_2 as an example of noble metal co-catalyst on TiO_2 is studied. Chapter 4 describes the light-induced Ostwald ripening of Pt on TiO_2 which is a special case of Gibbs-Thompson effect of noble metals on semiconductor. Then additional research is carried out on more complicated photocatalyst system-Ni/NiO core shell co-catalyst on TiO_2. Chapter 5 discusses the photo-corrosion of Ni/NiO core/shell structure on TiO_2 under light irradiation in liquid H_2O. Chapter 6 summarizes the research work and describes the future direction of this work. Graphene liquid cells are being prepared and the surface electronic structures of TiO_2 based photocatalyst can be explored using the ultra- high energy resolution electron energy-loss spectrum equipped on monochromated NION microscope.TiO_2 optical data together with the photon absorption calculation are discussed in Appendix I. Discussion of radiation damage is provided in Appendix II. Research work on CdS nanodots on TiO_2 nanorods and Ag nanoparticle coarsening are discussed in the appendix III and IV.

References

1. US Energy Information Administration (2015) Annual energy outlook (US Dept of Energy, Washington, DC).

2. Santer, B. D., Taylor, K. E., Wigley, T. M. L., Johns, T. C., Jones, P. D., Karoly, D. J., Mitchell, J. F. B., Oort, A. H., Penner, J. E., Ramaswamy, V., Schwarzkopf, M. D., Stouffer, R. J. & Tett. S. (1996). A search for human influences on the thermal structure of the atmosphere, *Nature*, 382, 39-46

3. Hegerl, G. C., Storch, H.V., Hasselmann, K., Santer, B. D., Cubasch, U. & Jones, P. D. (1996). Detecting Greenhouse-Gas-Induced Climate Change with an Optimal Fingerprint Method," *Journal of Climate*, 9, 2281-2306

4. US Energy Information Administration. (2015). Levelized cost and levelized avoided cost of new generation resources in the Annual Energy Outlook 2015.

5. Scott, S. A., Davey, M. P., Dennis, J. S., Horst, I., Howe, C. J., Lea-Smith, D. J., Smith, A. G. (2010). Biodiesel from algae: Challenges and prospects. Current Opinion in Biotechnology, 21 (3), 277–286.

6. Darzins, A., Pienkos, P. &Edye, L.(2010). Current status and potential for algal biofuels production. IEA Bioenergy Task 39.

7. Ronneau, C. (2004), Energie, pollution de l'air et developpement durable, Louvain-la-Neuve: Presses Universitaires de Louvain.

8. Perret. R. (2011) Solar Thermochemical Hydrogen Production Research: Thermochemical Cycle Selection and Investment Priority. *Sandia Report*

9. Conibeer, G.J. & Richards, B.S. (2007). A comparison of PV/electrolyser and photoelectrolytic technologies for use in solar to hydrogen energy storage systems. *International Journal of Hydrogen Energy*, 32,2703–271.

10. James, B. D., Baum, G. N., Perez, J., Baum, K. N. (2009). Technoeconomic analysis of photoelectrochemical (PEC) hydrogen production. *DOE Report GS-10F-009J*

11. Fujishima, A., & Honda, K. (1972). Electrochemical photolysis of water at a semiconductor electrode. *Nature*, 238, 37-38.

12. Kudo, A., & Miseki, Y. (2009). Heterogeneous Photocatalyst Materials for Water Splitting. Chemical Society Review, 38, 253–278

13. Vasileia, M. D., Maria, A., Gianlucali, P., Dimitris, I. K. & Panagiotis, L. (2010). Solar Light-Responsive Pt/CdS/TiO2 Photocatalysts for Hydrogen Production and Simultaneous Degradation of Inorganic or Organic Sacrificial Agents in Wastewater. *Environmental Science Technology*, 44, 7200–7205

14. Ni, M., Leung, M. K. H., Leung, D. Y. C., & Sumathy, K. (2007). A review and recent developments in photocatalytic water-splitting using TiO_2 for hydrogen production. *Renewable Sustainable Energy Review*, 11, 401–425.

15. Wang, C. C., Zhang, Z., & Ying, J. Y. (1997). Photocatalytic decomposition of halogenated organics over nanocrystalline titania. *Nanostructured Materials*, 9,583-586

16. Zhang, Z., Wang, C. C., Zakaria, R., & Ying, J. Y. (1998). Role of particle size in nanocrystalline TiO_2-based photocatalysts. *Journal of Physical Chemistry B*, 102, 10871-10878

17. Gong, D., Grimes, C.A., Varghese, O.K., Hu, W.C., Singh, R.S., Chen, Z., & Elizabrth C.D. (2001). Titanium oxide nanotube arrays prepared by anodic oxidation. *Journal of Materials Research*, 16 (12), 3331–3334

18. Liu, B., & Aydil, E. S. (2009). Growth of Oriented Single-Crystalline Rutile TiO_2 Nanorods on Transparent Conducting Substrates for Dye-Sensitized Solar Cells. *Journal of American Chemical Society,* 131, 3985–3990

19. Subramanian, V., Wolf, E., & Kamat, P.V. (2001). Semiconductor-metal composite nanostructures: to what extent do metal nanoparticles improve the photocatalytic activity of TiO_2 films? *Journal of Physical Chemistry B*, 105, 11439–11446.

20. Greeley, J., Jaramillo, T.F., Bonde, J., Chorkendorff, I., & Nørskov, J. K. (2005). Computational high-throughput screening of electrocatalytic materials for hydrogen evolution. *Nature Materials*, 5, 909-913.

21. Anpo, M., & Takeuchi, M. (2003). The design and development of highly reactive titanium oxide photocatalysts operating under visible light rrradiation. *Journal of Catalysis*, 216, 505-516

22. Sakthivel, S., Shankar, M. V., Palanichamy, M., Arabindoo, B., Bahnemann, D. W., & Murugesan V. (2004). Enhancement of photocatalytic activity by metal deposition: characterization and photonic efficiency of Pt, Au and Pd deposited on TiO_2 catalyst. *Water Research*, 38, 3001-3008.

23. Wu, N.L., & Lee, M.S. (2004). Enhanced TiO_2 photocatalysis by Cu in hydrogen production from aqueous methanol solution. *International Journal of Hydrogen Energy*, 29(15), 1601-1605.

24. Bardos, E.S., Czili, H., & Horvath, A. (2003). Photocatalytic oxidation of oxalic acid enhanced by silver deposition on a TiO_2 surface. *Journal of Photochemistry & Photobiology A*: Chemistry, 154, 195-201.

25. So, W.W., Kim, K.J., & Moon, S.J. (2004). Photo-production of hydrogen over the CdS-TiO_2 nano-composite particulate films treated with $TiCl_4$. *International Journal of Hydrogen Energy*, 29, 229-234.

26. Keller, V., & Garin, F. (2003). Photocatalytic behavior of a new composite ternary system: WO_3/SiC-TiO_2 effect of the coupling of semiconductors and oxides in photocatalytic oxidation of methylethylketone in the gas phase. *Catalysis Commun*ication, 4, 377-383.

27. Domen, K., Kudo, A., & Onishi, T. (1986). Photocatalytic decomposition of water into H_2 and O_2 over NiO-$SrTiO_3$ powder 1: Structure of the Catalyst. *Journal of Physical Chemistry, 90,* 292-295

28. Domen, K., Kudo, A., & Onishi, T. (1986). Mechanism of Photocatalytic decomposition of water into H_2 and O_2 over NiOx/$SrTiO_3$. *Journal of. Catalysis, 102,* 92-98.

29. Townsend, T. K., Browning, N. D., & Osterloh, F. E. (2012) Overall photocatalytic water splitting with NiOx–$SrTiO_3$ - a revised mechanism. *Energy Environmental Science*, 5, 9543

30. Maeda, K., Teramura, K., Lu, D., Takata, T., Saito, N., Inoue, Y., & Domen, K. (2006) Photocatalyst releasing hydrogen from water. *Nature*, 440, 295

31. Maeda, K., Hashiguchi, H., Masuda, H., Abe, R., & Domen K.(2008). Photocatalytic activity of $(Ga_{1-x}Zn_x)(N_{1-x}O_x)$ for visible-light-driven H_2 and O_2 evolution in the presence of sacrificial reagents. *Journal of Physical Chemistry C*, 112 (9), 3447–3452

32. Yoshida, M., Takanabe, K., Maeda, K., Ishikawa, A., Kubota, J., Sakata, Y., Ikezawa, Y., & Domen K. (2009) Role and function of noble-metal/Cr-layer core/shell structure cocatalysts for photocatalytic overall water splitting studied by model electrodes. *Journal of Physical Chemistry C*, 113, 10151–10157

33. Yamashita, H., Harada, M., Misaka, J., Takeuchi, M., Ichihashi, Y., & Goto, F., et al. (2001). Application of ion beam techniques for preparation of metal ion-implanted TiO_2 thin film photocatalyst available under visible irradiation: metal

ion-implantation and ionized cluster beam method. *Journal Synchrotron Radiation*, 8, 569-571.

34. Li, X., Lu, X., & Li, B. (2003). Photocatalytic production of hydrogen in single component and mixture systems of electron donors and monitoring adsorption of donors by in situ infrared spectroscopy. *Chemosphere*, 52(5), 843-850.

35. Dhanalakshmi, B., Latha, S., Anandan, S., Maruthamuthu, P. (2001). Dye sensitized hydrogen evolution from water. *International Journal of Hydrogen Energy*, 26. 669-674.

36. Fujishima, A., Zhang, X., Tryk, D. A., (2008). TiO_2 Photocatalysis and Related Surface Phenomena. *Surface Science Re*ports, 63, 515-582

37. Henderson, M. A. (1996). An HREELS and TPD study of water on TiO_2 (110): the extent of molecular versus dissociative adsorption. *Surface Science*, 355, 151−166.

38. Bikondoa, O., Pang, C. L., Ithnin, R., Muryn, C., Onishi, H., & Thorton, G. (2006). Direct visualization of defect-mediated dissociation of water on TiO_2 (110). *Nature Materials*, 5, 189−192.

39. Wendt, S., Matthiesen, J., Schaub, R., Vestergaard, E. K., Lagsgaard, E., Besenbacher, F., & Hammer, B. (2006). Formation and Splitting of Paired Hydroxyl Groups on Reduced TiO_2 (110). *Physical Review Letter*, 96, 066107.

40. Wendt, S., Schaub, R., Matthiesen, J., Vestergaard, E. K., Wahlstrom, E., Rasmussen, D., Thorstrup, P., Molina, L. M., Lagsgaard, E., Stensgaard, I., Hammer, B., & Besenbacher, F. (2005). Oxygen vacancies on TiO_2 (110) and their interaction with H_2O and O_2: A combined high-resolution STM and DFT study. *Surface Science*, 598, 226−245.

41. Knoll, M. & Ruska E. (1932). Das Elektronenmikroskop. *Zeitschrift fuer Physik*, 78, 318-339.

42. Williams, D. W., & Carter, C. B. (2009). Transmission electron microscopy. 2nd Edition. New York: Springer.

43. Wang, C. W., Xu, W., Liu, J., Choi, D.W., Arey, B., Saraf, L. V., Zhang, J.G., Yang, Z.G., Thevuthasan, S., Baer, D.R., & Salmon, N. (2010). *In-situ* transmission electron microscopy and spectroscopy studies of interfaces in Li ion batteries: Challenges and opportunities. *Journal of Materials Research*, 25(8), 1541-1547.

44. Minor, A. M., Asif, S. A. S., Shan, Z. W., Stach, E. A., Cyrankowski, E., Wyrobek, T. J., & Warren, O. L. (2006). A new view of the onset of plasticity during the nanoindentation of aluminium. *Nature Materials*, 5, 697-702

45. Cavalca, F., Laursen, A. B., Kardynal, B. E., Dunin-Borkowski, R. E., Dahl, S., Wagner, J. B. & Hansen, T. W. (2012) *In situ* transmission electron microscopy of light-induced photocatalytic reactions *Nanotechnology*, 23, 075705 (6pp)

46. Miller, B.K.; Crozier, P.A. (2013). System for In Situ UV-Visible Illumination of ETEM Samples *Microscopy & Microanalysis*, 19(2), 461-469.

47. G. M. Parkinson. (1989). High resolution, *in-situ* controlled atmosphere transmission electron microscopy (CATEM) of heterogeneous catalysts. *Catalysis Letters*, 2, 303-308

48. Creemer, J.F., Helveg, S., Hovelingc, G.H., Ullmannb, S., Molenbroekb, A.M., Sarroa, P.M. & Zandbergend, H.W. (2008) Atomic-scale electron microscopy at ambient pressure. Ultramicroscopy, 108, 9, 993–998

49. Giorgio, S., Sao Joao, S., Nitsche, S., Chaudanson, D., Sitja, G. & Henry, C.R. (2006). Environmental electron microscopy (ETEM) for catalysts with a closed E-cell with carbon windows. *Ultramicroscopy*, 106, 503-507

50. Yokosawa, T., Alan, T., Pandraud, G., Dam, B. & Zandbergen, H. (2012). *In-situ* TEM on hydrogenation of Pd at 0.5–4.5 bar hydrogen pressure and 20–400 ℃. *Ultramicroscopy,*112 (1), 47-52.

51. Hansen, T. W., Wagner, J. B., Hasen, P. L., Dahl, S., Topsoe, H., & Jacoboson, C.J.H. (2001). Atomic-resolution *in-situ* transmission electron microscopy of a promoter of a heterogeneous catalyst. *Science*, 294, 1508-1510.

52. Sharma, R. (2005). An environmental transmission electron microscope for *in-situ* synthesis and characterization of nano materials. *Journal of Materials Research*, 20(7), 1695-1707.

53. Li, P., Liu, J., Nag, N., & Crozier, P. A. (2005). Atomic-scale study of *in-situ* metal nanoparticles synthesis in a Ni/TiO2 system. *Journal of Physical Chemistry B*, 109(29), 13883-13890.

54. Gai, P. (1998). Direct probing of gas molecule—solid catalyst interactions on the atomic scale. *Advanced Materials*, 10, 1259-1263.

55. Gai, P., & Boyes, E. D. (2009). Advances in atomic resolution *in-situ* environmental transmission electron microscopy and 1Å aberration corrected *in-situ* electron microscopy. *Microscopy Research and Technique*, 72, 153-164

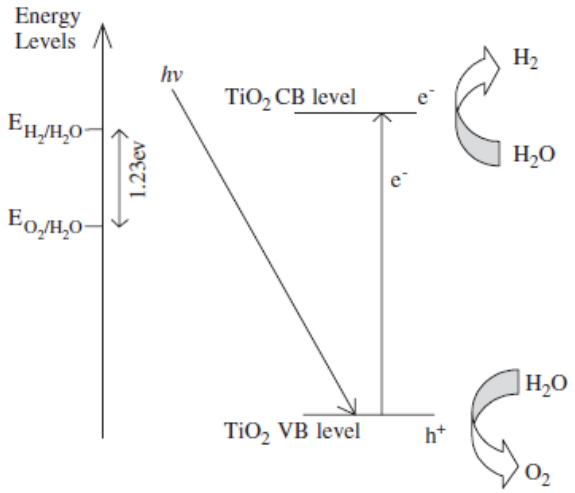

Figure 1.1 Schematic drawing of the photocatalytic watersplitting mechanisms [12]. Ni et al. Copyright 2007, Renewable Sustainable Energy Review

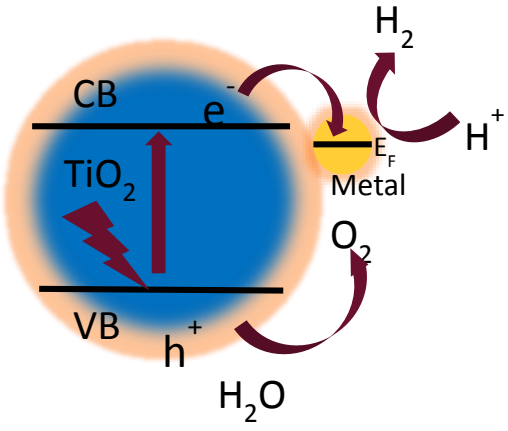

Figure 1.2 Schematic drawing of working mechanism for metal co-catalyst.

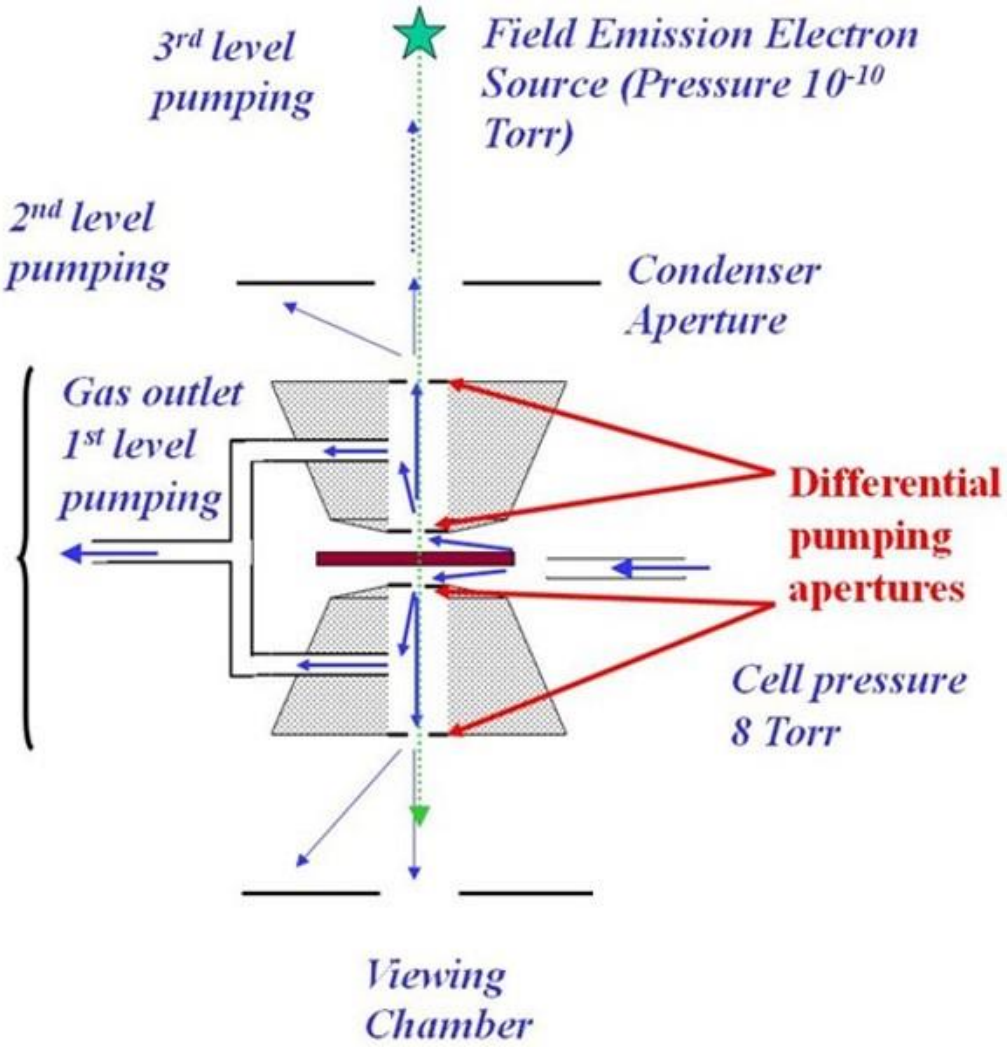

Figure 1.3 Schematic drawing of the construction of environmental cell in TEM.[52]

CHAPTER 2

INSTRUMENTATION AND EXPERIMENTAL METHODS

2.1 Introduction

Since this dissertation includes heavy characterization work, some detailed introduction of the main characterizations and instrumentations will be given in this Chapter. Photocatalytic reactions were carried out in a self-designed photo reactors. The products were measured in a Varian 450-GC Gas Chromatography (GC). The structural change of photocatalyst materials were carried out *in situ* in an environmental transmission electron microscope FEI Tecnai F20. *Ex-situ* experiments were carried out in a JEOL 2010F using TEM and STEM techniques for observation of structural change. Chemical information like reduction/oxidation states, surface band structures were explored using electron energy loss spectrum (EELS) on JEOL ARM 200F and NION UltraSTEM 100. X-ray photoelectron spectroscopy (XPS) was also applied to detect the valence states of surface atoms. Inductively coupled plasma mass spectrometry (IPS-MS) is applied to detect ions in water to understand photo-corrosion.

2.2 Catalytic Property Measurements

2.2.1 Photocatalysis Reactors

The self-designed photoreactor is shown as in Figure 2.1. The glass reactor is a 1.5 inch diameter cup with a 1/8 inch diameter inlet connected to a carrier gas tank and a 1/8 inch diameter outlet connected to a gas chromatography system. A 2 inch diameter quartz window together with an O-ring is clamped to the reactor to seal the top. Light is illuminated through the quartz window vertically from the top. The water suspended with

phototcatalysts was kept stirred during all the photocatalysis reactions. A 450W xenon research arc lamp house (Newport Inc.) was used as the light source for *ex situ* photocatalysis reactions. A 350nm to 450nm mirror together with a heat sink was used to filter off infrared light so the output port of the lamp house and the reactor did not get heated to high temperature. The light intensity can be calculated knowing the spectrum of the light bulb, the geometry and the reflectance of the filter. It was calculated to be 50mW/cm^2. The light intensity was also checked with Si-biased photo detector (THORLABS DET10A) to be consistent with the results from calculation.

2.2.2 Reaction Products Measurements.

The products of the photocatalysis reactions were measured by gas chromatography. Gas chromatography is a chemical analysis instrument which allows different components in a gas mixture to be separated and analyzed based on chromatographic separation principles. In gas chromatography, there are mobile and stationary phases. The mobile phase is usually an inert or unreactive carrier gas such as He, N_2 or Ar. The stationary phase is a layer of liquid or polymer on an inert solid support, inside a piece of glass or metal tubing called a column. When the gaseous compounds pass through the columns, they interact with the walls of the columns coated with stationary phases. Different gases pass through the columns in different time depending on the interactions between the gas and the column. This time is called the retention time of each gas. The gases having higher affinity to the surface of the stationary phase will pass the column in a longer retention time compared to gases with less affinity to the stationery phase. When the gas

chromatograph is plotted, the horizontal axis represents the retention time. Each different gas corresponds to a peak position along the -axis.

The intensities of the gases are measured by detectors in the GC. There are different kinds of detectors used in GC, such as thermal conductivity detector, flame ionization detector, mass spectrometer (MS) etc. Both TCD and FID were available on the Varian 3900 Gas Chromatography we used for our H_2 production rate measurement. TCD was used for our experiments. The TCD has two pathways, a sample path and a reference path. It measures the thermal conductivity difference from the sample side to the reference side. Carrier gas is continuously flowed through the reference path while different gases pass the sample path at a sequence dependent on the speed each gas is eluded from the column. The thermal conductivity of the carrier gas has to be very different from the gas needed to be measured. The thermal conductivity of different gases is summarized in Table 2.1 [1]. Ar was chosen as the carrier gas for H_2 detection while He was used for O_2 detection. For the gas chromatograph plotted from the GC, vertical-axis represents the intensity of different gases and the area under each peak is proportional to the amount of each gas. However, the peak areas cannot be directly interpreted as the amount of the gas because the thermal conductivity difference of each gas to the carrier gas gives different peak intensity ratio. The measured results has to be multiplied by a correction factor gained by the calibration from a known partial pressure of that pure gas mixed in the carrier gas. For H_2 detection using 3 cc/min Ar carrier gas, the integration of the area under the peak should be multiplied by correction factor 0.018 to get the real H_2 production rate with unit μmol/h.

2.3 Nanoscale Characterization

2.3.1 Observing structural changes using TEM and STEM

In a transmission electron microscope (TEM), high energy electron beam is transmitted through an ultrathin sample, interacting with materials, providing structural, chemical and electronic information of the sample materials. The first TEM was built by Max Knoll and Ernst Ruska in 1932 for the purpose of observing specimen smaller than the resolvable scale of the optical microscope [2]. A high-energy electron beam is used to illuminate the sample. An electromagnetic field was applied as lenses to focus or expand the beam and change the magnification. After interaction of the electron beam with the sample, the image is formed on a screen made with fluorescent materials or on a CCD camera.

Figure 2.2 shows the main components of a basic TEM. The electrons are emitted from electron guns. There are two kinds of electron gun-the thermionic gun and field emission gun (FEG). The thermionic guns are usually made with tungsten filaments or lanthanum hexaboride (LaB_6) crystals. The filament is heated to a high enough temperature to overcome the natural barrier preventing them from leaking out from the surface. The field emission gun tip is made of tungsten needles with sharp points so a high electric field $\mathrm{E} = \frac{V}{r}$ can be applied on to the tip with a very small radius r under a high voltage *V*. Field emission guns compared to thermionic guns have much better coherence and brightness which are critical to high-resolution TEM. Accordingly, the FEG is most popular on recent microscopes [3]. For FEG electron source, high extraction voltage is applied to pull out electrons from the tip and another ultra-high (usually 60kV-

300kV) voltage is applied to accelerate the electrons forming high energy electron beams. The electron beam is then adjusted by the condenser aperture and condenser lenses for needs of different intensity and convergent angles.

The electron beam will then pass the image forming system-objective lens and be transferred through intermediate lenses and projector lenses. The objective lens forms the first image and is thus most important for a good quality TEM image. The intermediate lenses change the magnifications and the projector lens transferred the image onto the screen or the camera. The images are projected onto a fluorescent screen for direct observation, or they can also be viewed and recorded on CCD cameras under the screen. There are two main types of TEM images-amplitude-contrast images and phase-contrast images, although they usually both contribute to one image [4]. The amplitude contrast results from the variation of mass or thickness of uniform samples, or when the objective aperture is used to form bright-field or dark-field images. At thicker areas where the beam interacts more with the materials, there will be more scattered beam and less transmitted beam than in thinner areas. When a bright field (BF) images is formed using the direct beam, thicker areas or areas with more mass of materials show darker contrast in the image. When a diffracted beam is used to form dark field (DF) images, the thicker areas will look lighter. The amplitude contrast allows us to distinguish material shapes, defects and morphology features. The phase-contrast images results from phase difference of the electron waves scattered by the thin specimen. For example, when a crystal material is oriented close to Bragg scattering angle for its certain crystal plane, electron beams which have gone through the Bragg's scattering interfere with (000) beam

and will form fringes with the distance of the d-spacing of the crystal planes. The phase contrast can be exploited at high magnifications for atomic structure of the samples. To detect the atomic phase contrast, it requires the microscope instrument to have optimum parameters so sufficient resolution can be achieved. For example, a common accepted information limit $r = 0.66 C_s^{\frac{1}{4}} \lambda^{\frac{3}{4}}$ relies on the spherical aberration Cs and the wavelength of the electron beam λ [5,6]. One may observe details in the scale smaller than this resolution but this resolution represents the interpretable resolution within which the image features can be trusted. This is related to the contrast transfer function (CTF). At a fixed C_s and optimum defocus (Scherzer defocus), the information limit corresponds to the first crossover of the CTF on the x axis.

Shown by the ray diagram of TEM image mode and diffraction mode in Figure 2.3, when the image plane of the objective lens is chosen as the objective plane of the intermediate lens, TEM images are formed on screen. TEM is used in diffraction mode when back focal plane of the objective lens is chosen as the objective plane of the intermediate lens. By measuring the distance between the diffracted spots to the center of the pattern, lattice spacings can be calculated knowing the wavelength and the camera length. Crystal structures can be determined with diffraction patterns. The lattice spacings achieved from the diffraction patterns can be compared with the lattice spacings of standard bulk materials for information of strain and impurities.

Another important mode of TEM is scanning transmission electron microscopy (STEM) which uses a focused electron beam probe to scan the specimen in a raster. The

electron beam is focused to a convergent probe and shifted across the sample by scanning coils located between condenser lens and the objective pole pieces. Bright-field or dark-field STEM images can be formed depending if the detector is placed to take un-scattered electrons or scattered electrons. High-angle scattered electron signals include more contribution from the scattering with heavier atoms. When a high-angle annular detector is used to capture scattered electrons, the heavy atoms show brighter contrast in the corresponding STEM images. This is so called the Z-contrast images where Z represents the atom number. Z-contrast images are very suitable for studying noble metal catalyst on supports [7, 8]. STEM is also preferred for studying localized chemical composition and electronic bonding with the help of energy-dispersive X-ray (EDX) spectroscopy and electron energy-loss spectocopy (EELS) techniques. The resolution of the STEM image depends on the probe size which relies on an optimum combination of electron source brightness, the convergent angle and spherical aberration [9]. The ex-situ study of Pt size distribution during the photocatalytic reactions using STEM was carried out with the JEOL JEM 2010 operated at 200kV with spherical aberration C_s=0.5mm.

Similar to the optical microscopes, resolutions of TEM/STEM are limited by the imperfections of electron beam source and electron lenses. There are many different aberrations but two important ones are chromatic aberration C_c and the spherical aberration C_s. The chromatic aberration results from the spread of the wavelength of electron beams. It is greatly improved by using monochromators with slits to filter or narrow the spread in wavelengths [10]. Spherical aberration is corrected by a set of specially designed auxiliary "lenses" which are called aberration correctors [11, 12].

These correctors produce negative spherical aberration cancelling out the positive spherical aberration of the objective lens. Some of the ex-situ characterization TEM images were taken on image-aberration-corrected FEI Titan.

2.3.2 *In-situ* Characterization in Environmental TEM

To better design photocatalyst we would like to understand charge transfer at surfaces/interfaces and the resulting structure changes that take place under working conditions. Different TiO_2-based photocatalysts were characterized *in situ* in FEI Tecnai F20 environmental TEM equipped with a light illumination system.

2.3.2.1 Environmental TEM

The environmental TEM FEI Tecnai F20 is a field-emission TEM operated at 200kV with an information limit 0.14 nm. Besides TEM, STEM and EELS capabilities, the F20 is equipped with gas handling and light illumination systems. The gas handling system is shown in Figure 2.4. It is composed with a gas mixing tank, a gas inlet to the TEM chamber and two outlets from first and second level differential pumping. The water is evaporated from a glass container on a branch of the gas inlet. The gas pressure is precisely controlled by a leak valve on the inlet to the chamber. The FEI Tecnai F20 is equipped with a differential pumping system shown in Figure 2.5. The gas is injected from the inlet at the same level of the sample. The leaking of gas into the remainder of the TEM column is controlled by the first and second level differential pumping apertures so the specimen can be surrounded by sufficient gas pressure while the gas will not be released to degrade the vacuum system and destroy the gun. The gas pressure which the

pumping system can handle is dependent on the weight and affinity of different gas molecules. For H_2O gas, *in situ* observation can be performed even with saturated H_2O vapor pressure at room temperature which is around 18 Torr. To avoid contamination and also generate a condition close to a practical vapor-phase water-splitting condition, a moderate heating of the sample to 150 ℃ was performed for some of the *in situ* experiments. Different heating holders can only be used with certain gases and temperatures. For example, heating holders with furnaces made of Ta cannot be used in strongly oxidizing gas mixture at high temperature. Some heating holders need water cooling above 500 ℃. The temperature at the sample is measured by the thermocouple on the holder. The temperature is controlled by changing the current running into the furnace under the specimen.

A very important factor to the success of *in situ* experiments is to minimize the contamination problem. Contamination could be any unwanted gas which may disturb the results of *in situ* experiments. A common contamination is hydrocarbon gases depositing amorphous carbon layers on samples under electron beam. The carbon contamination film will degrade the visibility of fine crystal structures and reduces the contact of surface atoms with reactant gases. There are multiple sources of contamination. The connections and valves of the gas-handling system may have leak problems exposing the system to air. Installation of the light illumination system requires venting the chamber also exposing the chamber to air. Very small amount of hydrocarbon in the air could cause serious carbon contaminations. Complex gas precursors may have been used for experiments like *in situ* characterization of Si wire or carbon tube growth [13-15]. The

precursors could stick to the walls of the chamber and the lines as a contamination source for later experiments. “Bake-out” is a regular procedure to deal with contamination. The lines and valves of the gas handling system are wrapped with heating tapes. When running a bake-out, electric current runs through the tapes, heating the gas handling system to 150 ℃- 200 ℃. Cooling water is cut off for the TEM column and the current running through the coils of the electro-magnetic lenses heats the column to about 80 ℃. The baking of the whole system helps to detach the residual contaminants from the walls and are then pumped out with all the valves open. It is important to keep both the gas-handling system and the microscope warm so contaminants baked out do not redeposit at cooler places. The contaminants will be greatly reduced after the bake-out. Further cleaning can be done with plasma cleaners generating an oxidative plasma to decompose the contaminants. The water and the water container which were exposed to air could also contain contaminants. Before *in situ* experiments, H_2O vapor is always bypassed from the TEM chamber and directly pumped for over 30mins before it was let into the TEM chamber. This procedure is to ensure that the initial accumulated contaminants attached to the container or dissolved in the liquid water get pumped out first.

2.3.2.2 *In situ* Light Illumination System.

In order to set up reaction conditions for *in situ* characterization of photocatalyst, light illumination is required. Not many works have been reported developing light illumination systems on TEM. Yoshida et al. developed a light illumination system where 10mW/cm^2 UV light was directed through an optical fiber from an outside light source onto the TEM sample. Photodecomposition of pre-deposited hydrocarbons on TiO_2 thin

films was observed when exposed to UV light [16]. With the same light illumination system, a single crystal to poly-crystalline transformation on TiO_2 thin films with oxygen release was observed during photocatalytic oxidation of hydrocarbons on TiO_2 [17]. Cavalca et al. developed a light illumination system on a TEM sample rod with a lens-based and a fiber optics-based design [18]. The lens-based design includes a laser diode along the axis of a feedthrough slightly above the sample plane. The light was focused and directed by lenses onto the bent TEM grid. The lens-based design has the advantage of high intensity and easy operations. However, it is limited to the narrow wavelength dependent on the laser diode which is hard to change once mounted on the holder and aligned. The fiber-based design allows light from an outside source to be directed through an optical fiber mounted with feedthrough in the TEM holder. The outside light source can be a white light source with broadened wavelength. The flexible light source allows photocatalysts with different band gaps to be studied under different wavelength. Both of the two designs have some restrictions on sample tilting which is very important in the study of single crystal materials. Photodegradation of Cu_2O in H_2O vapor and photodeposition of Pt on GaN:ZnO were observed under light illumination [18,19].

A different light illumination system totally separated from the TEM holder was designed by Miller et al. at Arizona State University [20]. The idea of this design is to allow the full ability of tilting and heating since the light illumination system is separated from the holder. This illumination system is attached to an FEI Tecnai F20 ETEM. It utilizes a port which was for installation of an energy-dispersive X-ray spectrometer. The port where the optic fiber goes through is perpendicular to the TEM sample rod axis. As shown in the drawing in Figure 2.6, the sample is sitting in the center of the 5.4mm

spacing between the upper and lower pole pieces. The fiber is directed through a brass tube slightly bent so the fiber can be brought as close as possible to the TEM sample from below. The reason that light is illuminated from below the sample stage is because the heating wires of the hot stage furnace block some sample areas and cause shadowing. A 600 μm silica core, silica clad, and solarization resistant optical fiber is used. It is clad with aluminum to avoid being charged by secondary and backscattered electrons. Ideally vertical illumination is desired to avoid shadowing from the hot stage furnace edges. In fact, due to the limiting spacing between pole pieces and the shallow angles of the pole pieces, the fiber is bent 15 °against the horizontal level so that the most intense area of the light beam falls onto the center of the optic axis of the TEM column as shown in Figure 2.7. The front of the fiber is cut to 30 ºto refract more light onto the TEM sample. The fiber is centered with a manipulator constructed with bellows in xyz directions. With micrometer manipulators on different directions, the position of the fiber can be optimized to the best position where the highest intensity falls on the center along the axis of the electron beam. The manipulator also provides vacuum feedthrough where the inside fiber is coupled to an outside fiber then to the external light source.

One of the advantages of this design is that any light source can be adapted to this light illumination system with an optical fiber. At present, the ASU system employs a broadband laser-driven Xenon lamp light source from Energetiq Technology Inc. The intensity distribution of the output of the light is plotted in Figure 2.8. 90% of the intensity is focused in the “hot zone” 0.2 X 0.4 mm large. The highest intensity is about 1400 mW/cm^2 which is about 10 suns. The optimum position of the optical fiber is checked by a photomultiplier tube (PMT) shown in Figure 2.9. Instead of connection to a

light source, the optical fiber is connected to a PMT. Fluorescent nanoparticles ZnS (P22) are used to emit light under excitation of the electron beam. According to reversibility of the optical path, PMT should capture more emitted light from fluorescent nanoparticles when closer to the optimum position. The electron beam can be focused on tiny area on fluorescent materials making it a spot light source. The PMT read out is thus very sensitive to the position change of the end of the optical fiber. In this way, the position at which the fiber gives maximum intensity of light to the center of the electron beam axis can be precisely adjusted.

2.3.3 Analysis of Chemical and Electronic States Using XPS and EELS

To understand mechanisms behind structure change, chemical information such as elemental composition, chemical state and electronic state have to be achieved by spectroscopic techniques. X-ray photoelectron spectroscopy (XPS) is applied for determining the chemical state of Ti on TiO_2 surfaces after photocatalytic reaction water splitting. XPS spectra are obtained in high vacuum (P ~ 10^{-8} millibar) or ultra-high vacuum (P < 10^{-9} millibar) atmosphere conditions. Material is exposed to a beam of x-rays and electrons are excited and escaped from the top 0 to 10 nm of material. The kinetic energy and number of electrons are analyzed simultaneously. The binding energy can be calculated knowing the energy of the incident X-ray E_{photon} , the measured kinetic energy of the excited electron and the work function ϕ, which is usually a constant depending on the instrument and the material: $E_{binding} = E_{photon} - (E_{kinetic} + \phi)$. The numbers of electrons per unit time are plotted against the binding energy of the electrons detected. Each element with certain chemical state is correlated to a characteristic peak

set of certain binding energies, and the number of electrons represent the amount of that element and its chemical state. The percentage of the element should be corrected by dividing the signal by a relative sensitivity factor and normalized over all the elements [21].

Since XPS technique uses a spot size in the range of 150-1000 μm, it is considered gentle and does not damage materials with strong interactions. However, it only interacts with the first 10nm surface of the material. It also does not have sufficient spatial resolution which allows atomic-level local chemical information to be detected. Electron energy-loss spectroscopy (EELS) technique available in many TEMs is used to explore atomic-scale local elemental composition, chemical bonding information and electronic structure. When electron beam is transmitted through thin specimens, it can interact with material with elastic and inelastic scattering. During inelastic scattering which is usually electron-electron collision, energy will be transferred from the incident electron beam to excite the inner shell or outer shell electrons of the material. As shown in Figure 2.10, after interaction with the specimen, the transmitted electron beam is selected by a variable entrance aperture. The electrons passing through the entrance aperture travel down a “drift tube” through the spectrometer and are deflected over 90° by the magnetic field [4]. The ones with more energy loss are deflected less than the ones with less energy loss. A spectrum is then formed on a dispersion plane with electron intensity versus energy loss.

The EELS can be divided into two regions, the core-loss region and the low-loss region. The core-loss spectrum is composed with electrons that have ionized the inner-shells of the atom. The near-edge structure in core-loss region spectrums can be exploited to determine valence and bonding states. The low-loss region is usually within ~50 eV of the zero-loss-energy peak (ZLP). It contains information from interactions of outer-shell electrons with the electron beam. This part reflects the dielectric response of the specimen to high-energy electrons and reveals the electronic structure and bonding information of the specimen. With the innovation of monochromated aberration corrected NION microscope, extraordinary high energy resolution of less than 12meV can be achieved making very fine electronic structures detectable [22]. Recent paper has been published demonstrating the capability to detect localized phonon vibrations [22]. Core-loss EELS was applied to determine Ti valence state on the TiO_2 surface after exposure to water and light. More details will be given in Chapter 3. Low-loss region with extraordinary high energy resolution is utilized to explore band gap and inter-band states on photocatalyst materials surface at atomic-scale level. Results are given in Chapter 6.

2.3.4 Detection of Metal in Solution During Photocatalytic Reactions Using ICP-MS

To check if Ni or Pt metal co-catalyst have been ionized and dissolved into solution, the amount of Ni or Pt in the water before and after the reactions were determined by inductively coupled plasma mass spectrometry (ICP-MS). This is achieved by ionizing the sample with inductively coupled plasma and then using a mass spectrometer to separate the ionized element and measure its quantity. By measuring the resulting isotopic composition, it is possible to calculate the amount of the analyte present

in the sample. A deionized water blank and initial samples were acidified in ~0.32 M nitric acid with trace metal grade nitric acid. A series of water samples (1ml each) were taken every 30mins from the total volume 50mL solution during the photo-reaction over a period of 4hrs after turning on the light. The water samples were diluted five-fold to keep them within the instrument's calibration range. Samples were analyzed by quadrupole ICP-MS (ThermoFisher Scientific iCAP Q, with CCT option). Ni, Pt and Ti were run in CCT-KED ("Collision Cell Technology-Kinetic Energy Discrimination") mode with high purity He as the collision cell gas. Samples were measured with isotopes ^{58}Ni, ^{60}Ni; ^{194}Pt, ^{195}Pt, ^{196}Pt and ^{62}Ni, ^{47}Ti, ^{48}Ti and ^{49}Ti, respectively to monitor for interferences, but only data from ^{60}Ni, ^{194}Pt and ^{47}Ti measurements are reported. These isotopes had the best detection limit and gave the most reliable and accurate results.

References:

1. Tennet, R.M. (1971). Science Data Book. Oliver & Boyd.

2. Knoll, M. & Ruska E. (1932). Das Elektronenmikroskop. *Zeitschrift fuer Physik*, 78, 318-339.

3 Orloff, J. (1989). Survey of Electron Sources for High-Resolution Microscopy, *Ultramicroscopy*, 58, 88-97.

4 Williams, D. W., & Carter, C. B. (2009). Transmission electron microscopy. 2nd Edition. New York: Springer.

5 Van Dyck, D. & De Jong, A. F. (1992). Ultimate resolution and information in electron microscopy: general principles. Ultramicroscopy, 47, 266-281

6 De Jong, A. F. & Van Dyck, D. (1993). Ultimate resolution and information in electron microscopy. II. The information limit of transimission electron microscope. Ultramicroscopy, 49, 66-80.

7 Treacy, M. M. J., & Howie, A. (1980). Contrast Effects in the Transmission Electron Microscopy of Supported Crystalline Catalyst Particles. *Journal of Catalyst*, 63, 265-269

8 Treacy, M. M. J., Howie, A., & Wilson, C. J. (2006). Z Contrast of Platinum and Palladium Catalysts. *Philosophical Magazine A*, 38(5), 569-585.

9 Micheal, J.R. and Williams, D.B. (1987). A consistent definition of probe size and spatial resolution in the analytical electron microscope. *Journal of Microscopy*, 147, 289-303

10 Kimoto, K. (2014). Practical Aspects of Monochromators Developed for Transmission Electron Microscopy. *Microscopy*, 63(5), 337-344.

11 Rose, H. H. (2008). Optics of high-performance electron-microscopes. *Science and Technology of. Advanced Materials*, 9, 014107 (30pp).

12. Tanaka, N. (2008). Present status and future prospects of spherical aberration corrected TEM/STEM for study of nanomaterials. *Science and Technology of. Advanced Materials*, 9, 014111 (11pp).

13. Sharma, R., Zafar, I. (2004). In situ observations of carbon nanotube formation using environmental electron microscopy (ETEM). *Applied Physics Letter*, 84, 990-992

14. Sharma, R., Rez, P., Brown, M., Du, G., Treacy, M. M. J. (2007). Dynamic observations of the effect of pressure and temperature conditions on the selective synthesis of carbon nanotubes. *Nanotechnology,* 18, 125602 (8pp).

15. Hannon, J.B., Kodambaka, S., Ross, F. M., Tromp, R. M. (2006). The influence of the surface migration of gold on the growth of silicon nanowires. *Nature*, 440, 69–71.

16. Yoshida K., Yamasaki J. & Tanaka N. (2004). In situ high-resolution transmission electron microscopy observation of photodecomposition process of poly-hydrocarbons on catalytic TiO_2 films. *Applied Physics Letters*, 84, 2542-2544

17. Yoshida K., Nanbara, T., Yamasaki J., Tanaka, N. (2006), Oxygen release and structural changes in TiO2 films during photocatalytic Oxidation, *Journal of Applied Physics*, 99, 084908

18. Cavalca F., Laursen A. B., Wagner, J. B., Damsgaard, C. D., Chorkendorff, I. & Hansen T. W. (2013) Light-induced reduction of cuprous oxide in an environmental transmission electron microscope. *ChemCatChem,* 5, 2667-2672.

19. Cavalca, F., Laursen, A. B., Kardynal, B. E., Dunin-Borkowski, R. E., Dahl, S., Wagner, J. B. & Hansen, T. W. (2012) *In situ* transmission electron microscopy of light-induced photocatalytic reactions *Nanotechnology*, 23, 075705 (6pp)

20. Miller, B.K.; Crozier, P.A. (2013). System for In Situ UV-Visible Illumination of ETEM Samples *Microscopy & Microanalysis*, 19(2), 461-469

21. Ray, S. & Shard, A.G. (2011). Quantitative Analysis of Adsorbed Proteins by X-ray Photoelectron Spectroscopy. *Analytical Chemistry*, 83(22), 8659-8666

22. Krivanek, O. L., Lovejoy, T. C., Dellby, N., Aoki, T., Carpenter, R. W., Rez, P., Soignard, E., Zhu, J., Batson, P. E., Lagos, M. J., Egerton R. F. & Crozier P. A. (2014). Vibrational spectroscopy in the electron microscope. *Nature*, 514, 209-212

23. Sharma, R. (2005). An environmental transmission electron microscope for in-situ synthesis and characterization of nanomaterials. *Journal of Materials Research*, 20(7), 1695-1707.

24. Zhang L., Miller B. K. & Crozier P.A. (2013). Atomic level in situ observation of surface amorphization in anatase nanocrystals during light irradiation in water vapor. *Nano Letters*, 13(2), 679–684.

Gas	Thermal Conductivity ($Wm^{-1}K^{-1}$)
Hydrogen	1684
Helium	1415
Nitrogen	243
Argon	162
Methane	302
Oxygen	244
Carbon monoxide	232
Carbon dioxide	145
Water vapor	158

Table 2.1 Thermal Conductivity of different gases [1].

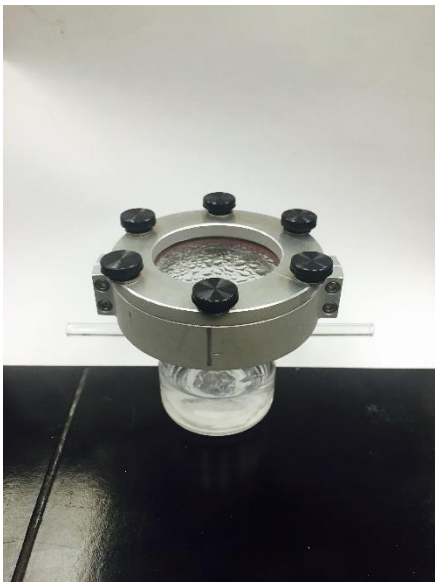

Figure 2.1 Photocatalytic reactor.

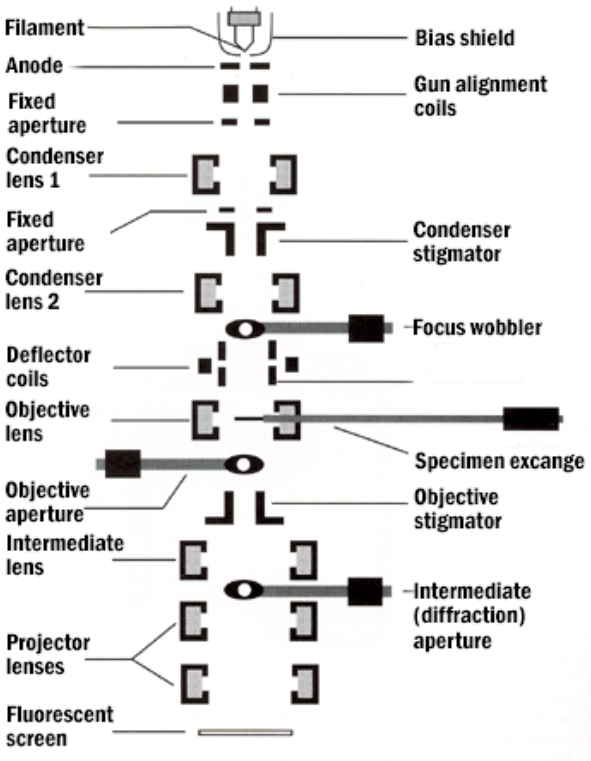

Figure 2.2 TEM components.

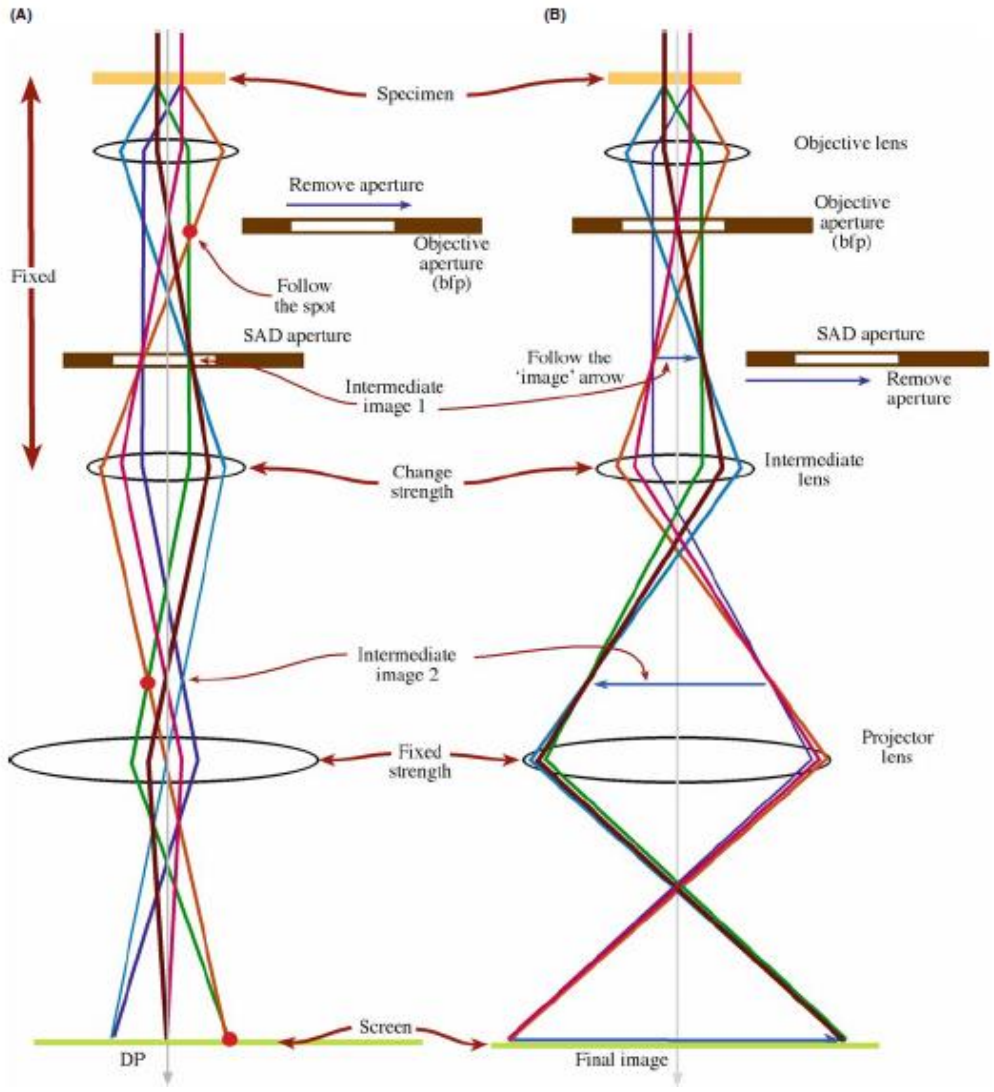

Figure 2.3 TEM ray diagram (a) Diffraction mode (b) TEM image mode [4].

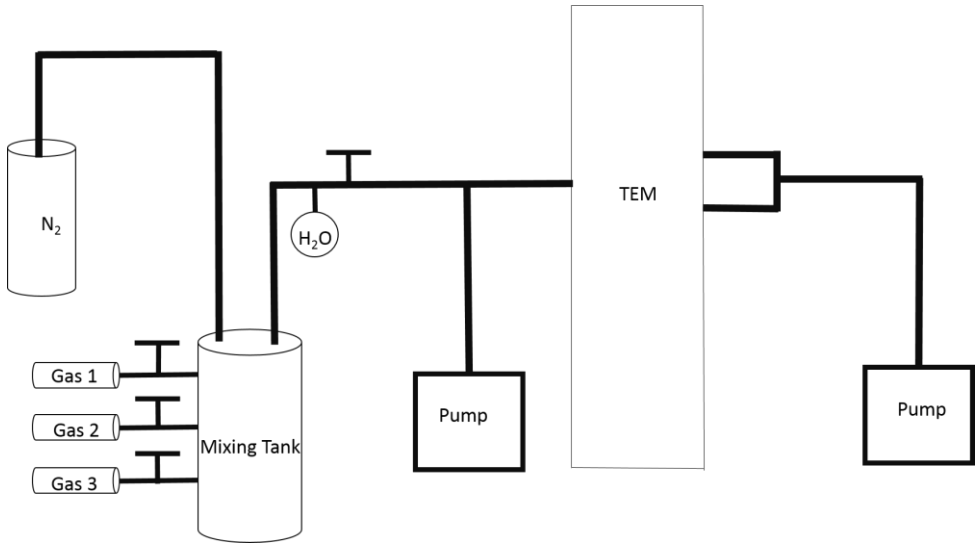

Figure 2.4 Gas handling system for environmental TEM.

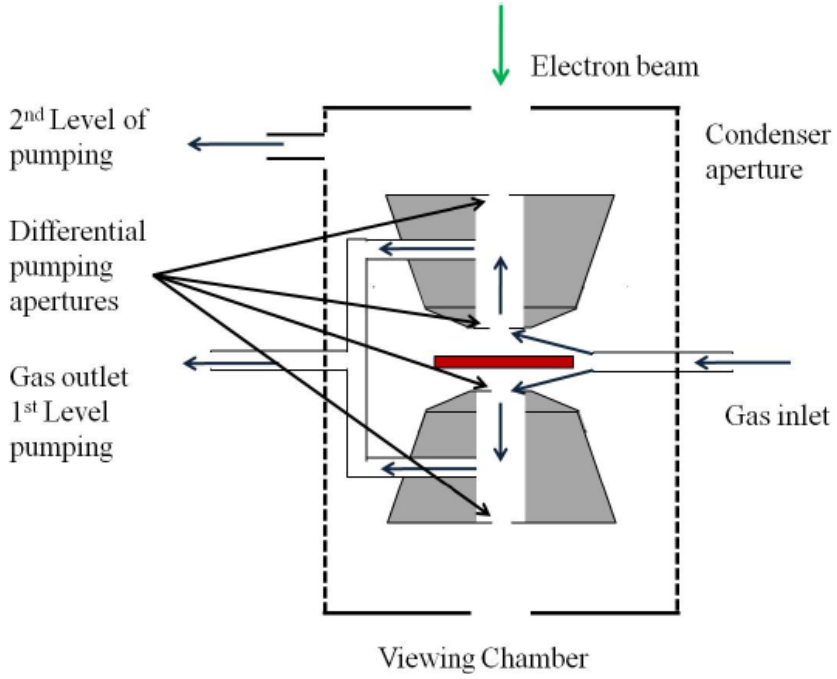

Figure 2.5 Differential pumping system [23].

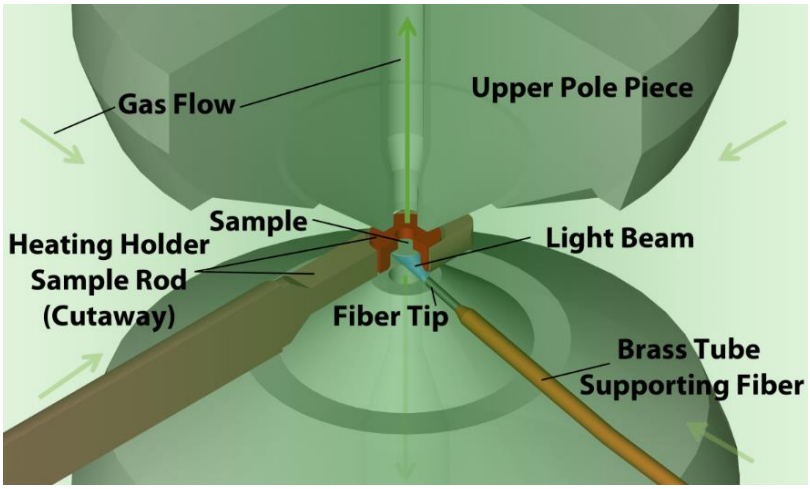

Figure 2.6 Schematic diagram of the overall geometry of in situ fiber illumination system [24].

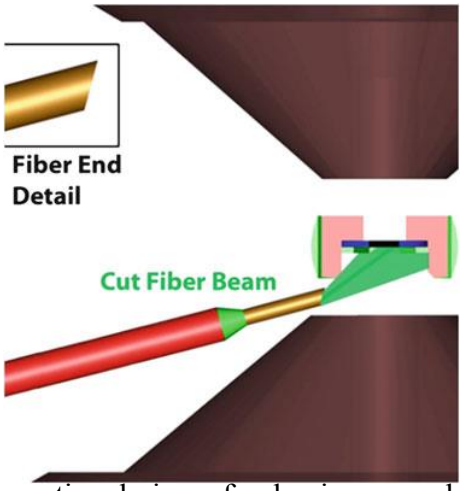

Figure 2.7 Cross sectional view of pole piece gap showing fiber orientation relative to upper and lower pole pieces.

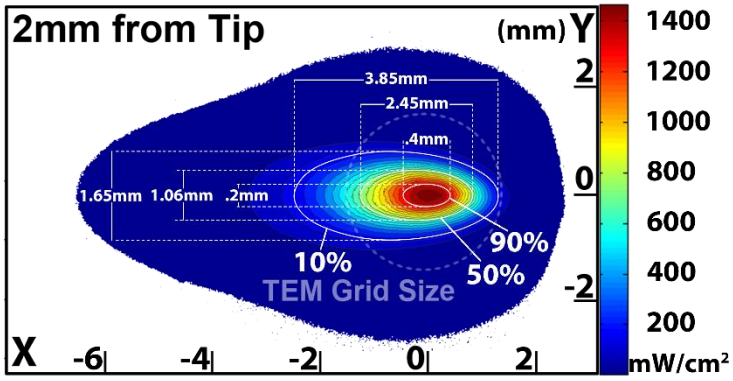

Figure 2.8 Light intensity incident on the sample as a function of position [20].

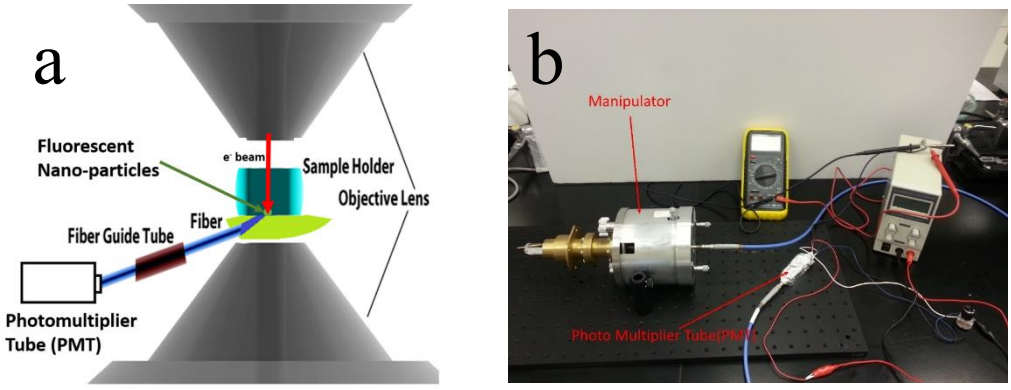

Figure 2.9 (a) Schematic diagram of checking the optimization position of optical fiber by using PMT. (b) Photograph showing the connections of the manipulator to the PMT.

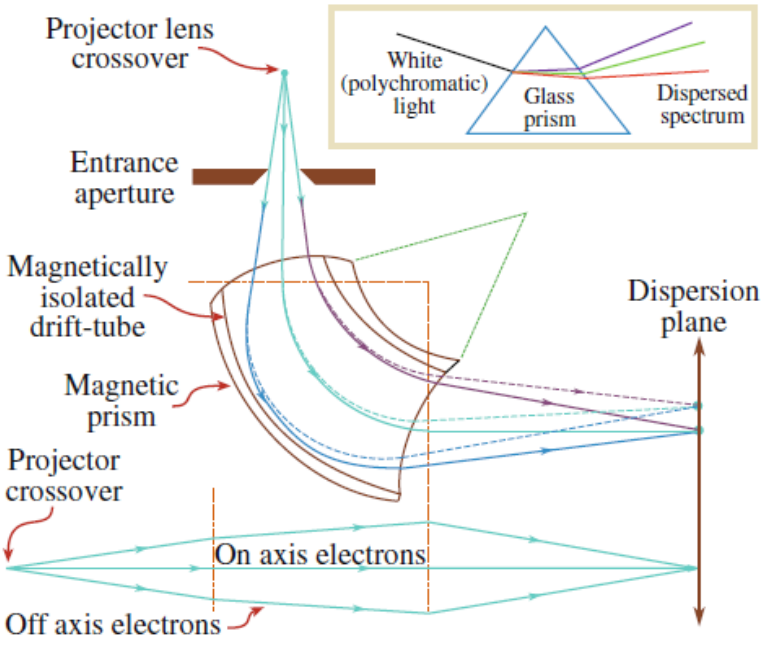

Figure 2.10 Schematic drawing of ray paths through a magnetic prism spectrometer with the insertion showing similarity to the dispersion of white light by a glass prism [4].

CHAPTER 3

STRUCTURE EVOLUTION OF HIGH SURFACE AREA WELL DEFINED TiO_2 ANATASE UNDER LIGHT IRRADIATION IN H_2O.

3.1 Introduction

While substantial improvements in performance have been realized for photocatalystic water splitting, a viable technology based on light-induced water splitting is not yet available [1-3]. It is now recognized that atomic-level *in situ* observations of catalytic materials are critical for understanding the structure-reactivity in catalysts. For many catalysts, the active form of the material may exist only under reaction conditions and must be characterized to develop a fundamental understanding of structure-reactivity relations. For photocatalysts, this requires that the system be observed not only in the presence of reactant and product species but also during *in situ* light illumination.

In this chapter, an *in situ* study of the surface for anatase nanoparticles under reaction conditions for vapor phase water splitting is reported. TiO_2 is very stable and it can be functionalized with other semiconducting and metal particles to increase absorption in the visible and improve its catalytic performance [4-7]. We would like to study the pure semiconductor TiO_2 with *in situ* characterization first and then expand to TiO_2-based photocatalyst functionalized by other semiconductors or metal co-catalyst.

To better design nano-TiO_2 for photocatalytic reactions, many fundamental studies have been carried out to understand the structure and photocatalytic property relationships [8]. For example, water dissociated at oxygen vacancies in ultrahigh vacuum conditions,

forming hydroxyl groups, were detected using temperature-programmed desorption (TPD), high resolution electron energy-loss spectrum (HREELS), and scanning tunneling microscopy [9-12]. However, most of these atomic surface studies were carried out on reduced (110) surfaces of bulk rutile crystals under UHV (10^{-10} Torr) conditions. To extend this understanding, it is necessary to perform *in situ* atomic level studies on nanoparticles under conditions more close to those present during photocatalytic reactions.

Here we employ atomic-resolution environmental transmission electron microscopy (ETEM) to study the structure of anatase nanoparticles subjects exposed to 1 Torr of water vapor and broad-band light illumination with a total intensity of 1430mw/cm^2 and a UV part which can be absorbed by anatase (200nm-800nm) with intensity of 122mw/cm^2. We show that significant changes take place in the first few monolayers of the anatase crystals in the presence of light and water vapor. This re-structured surface will be present on the anatase surface under reaction conditions relevant to photocatalytic splitting of water. This work was published in Nano Letters in 2013 [13].

3.2 Preparation of Well-Defined Anatase Particles.

Pure crystallized and shape-controlled anatase particles were transformed from Evonik P25 particles (80% anatase and 20% rutile) using a hydrothermal method [14, 15]. 2.5g of P25 powder was mixed with 60ml 10M NaOH aqueous solution followed by heating in a Teflon lined autoclave at 180 ℃ for 20hr. The resulting sodium titanate was then washed with 0.1M HNO_3 and water until the pH was close to neutral. The suspension was then subjected to another hydrothermal treatment in water with pH close to 7 at 180 ℃ for 48hr. The resulting slurry was washed and dried, and XRD showed that the final product powder was

pure anatase. The anatase nanocrystals showed rhombic and rod morphologies with well-defined {101} and {002} surface terminations.

3.3 *In-situ* Study of the Structure Evolution of TiO_2 Anatase under Light Irradiation in H_2O Vapor.

The samples were illuminated with UV and visible light from a bright, broadband source, via an optical fiber which directs the light onto the sample inside the ETEM (Figure 3.1). Technical details on the *in situ* light illumination were described in chapter 2. Here we summarize the more important characteristics of the system. The source produces a nearly blackbody spectrum, and so mimics the Sun's spectrum reasonably well. On the TEM sample, the intensity is about 10 times that of the sun on the earth's surface. Optical filters can optionally be used to specify a smaller wavelength range if needed for an experiment. The maximum intensity while using the full spectrum is 1460mW/cm^2 with 90% intensity in a 0.2x0.4mm region around optical axis if aligned correctly. The region is large enough to cover about 4x8 grids close to the optical axis for 300 -mesh TEM grids. High-resolution transmission electron microscopy (HRTEM) images were recorded using a Tecnai F20 (FEI) ETEM equipped with a differentially pumped environmental cell operated at 200KV. To facilitate the TEM analysis, anatase powders were dispersed onto Stober silica spheres and the spheres were then dispersed over Pt grids using a drop casting method [16]. The Pt grid was loaded into a Gatan hot stage and the *in-situ* TEM characterization was performed at a temperature of 150 ℃ to simulate the conditions for vapor phase water splitting.

Titania is well known to undergo radiolysis under electron-beam irradiation in the TEM [17, 18]. To extract accurate information about the active form of titania under

photoreactor conditions, it is important to minimize the electron dose and to fully understand the effects of electron irradiation during observation at temperature in the water vapor atmosphere. Control experiments must be designed to ensure that changes in the material from electron irradiation are clearly identified and not mistakenly attributed to photon irradiation. Three different experiments (Table 3.1) were conducted in which the electron dose, reactive gas and light flux were varied. In the first experiment (condition A), atomic-resolution TEM images were initially recorded with an electron dose of 3000e-/$Å^2$/s from selected anatase particles. The particles were then exposed to water vapor and subsequent images were recorded from the same particle after 1, 7, 20 and 40 hours. The electron beam was off during most of the experiment and was turned on only briefly to record images.

A typical set of images from this experiment is shown in Figure 3.2. The initial particle was well defined and bounded mainly by the low energy {101} and shorter {002} surfaces. The particles appear crystalline on the surface and the surface is smooth and atomically abrupt. There was no obvious evidence for any structural change taking place during this initial observation. After 1 hour of exposure to H_2O, the surface showed evidence for disorder and this effect became more pronounced after 7 hours with the particle showing significant disorder on the top monolayer. The disordered layer thickened slightly with time. After 40 hours, the width of the ordered crystal along the [101] direction was observed to decrease from 9.70 ± 0.05nm to 9.35 ± 0.05nm during the growth of the amorphous layer. This reduction of about 0.35 nm suggests that the top monolayer of each surface has become amorphous. This decrease in the width of the crystalline area was also

observed in samples irradiated with light and shows that the amorphous layer is not an overlayer of contamination.

The electron beam diameter is rather small and the imaging is typically conducted with a beam less than 50 nm in diameter. Consequently, most of the TEM sample was not irradiated with electrons and thus we were able to acquire images from fresh, unirradiated areas for each of four water exposure times (1, 7, 20 and 40 hours). A typical image from one of the fresh areas exposed only to H_2O for 40 hours is shown in Figure 3.2 f. These crystals showed clean crystalline (101) surfaces similar to the original starting materials and there was no evidence for any amorphous layer on the surface. This data shows that exposure only to 1 Torr of H_2O at 150^oC does not significantly impact the surface structure of the anatase. Disordered layers form only on crystals exposed to both the electron beam and water. This suggests that the formation of the amorphous layer is caused by the combination of electron irradiation and the H_2O atmosphere.

Both the electrons and the photons can generate electron-hole pairs in the anatase which may lead to the formation of reaction centers for water dissociation [19-21]. It is useful to consider the energy deposited into an anatase crystal from both electron and photon irradiation under the conditions present in the ETEM. The energy deposited from the electron beam can be determined by considering energy transfer associated with both elastic and inelastic scattering. The inelastic scattering contribution, which causes radiolytic damage, can be determined from the electron energy-loss spectrum from a thin anatase particle. The probability of an electron transferring ΔE_n into the specimen due to an inelastic collision is approximately the ratio of the $In(\Delta E_n)/I_{tot}$ where $In(\Delta E_n)$ is the intensity in the electron energy-loss spectrum corresponding to energy loss ΔE_n and I_{tot} is

the total integrated intensity in the spectrum [22]. We assume that only energy transfers greater than the band-gap energy Eg are important for exciting the anatase. With an electron fluence with number of Ne electrons/unit area, the total energy transferred per unit area can then be written as:

$$E = \sum_n N_e \Delta E_n \frac{I_n}{I_{tot}} \quad (3.1)$$

The total electron flux employed to record five atomic resolution TEM images within a total 100s (20s to take each image including the time adjusting focus) is about 3 x 10^5 e^- /Å^2 giving a final energy dose absorbed into the sample of about 3000 J/cm^2. That is a deposition rate of 30 W/cm^2. (The energy deposited by elastic scattering is small and is calculated to be about 0.65J/cm^2 which is negligible compared to the ionization damage. The calculation of energy deposition due to elastic scattering is provided in Appendix II.)

A simple Beer's law analysis can be used to show that the photon energy absorbed per unit surface area of anatase is given as

$$\int I_\lambda [1 - \exp(-\alpha_\lambda t)] d\lambda \quad (3.2)$$

where t is the thickness of the sample, I_λ is the photon intensity at wavelength λ and the integral is performed from 200 – 800 nm. α_λ is the corresponding absorption coefficient which is derived from the dielectric data of anatase [23]. The optical data is attached in Appendix I. Assuming a light intensity of 1460mW/cm^2 (10 suns) gives an energy deposition rate of 55mW/cm^2. For a light exposure experiment lasting 12 hours, this gives a total energy deposition of 2380 J/cm^2. A summary of the various electron and photon irradiation parameters for these experiments is given in Table 3.2.

This calculation shows that even under moderate electron irradiation conditions, the energy deposition rate by the electron beam is about 3 orders of magnitude greater than the energy deposition rate from photon illumination at an intensity close to 10 suns. Moreover, the experimental measurements of Figures 3a to 3e show that, in the presence of 1 Torr H_2O, this electron dose is sufficient to modify the surface structure of anatase. Consequently, if electron-beam effects are to be made negligible, it is not possible to follow the time evolution of individual anatase particles during photon irradiation. Instead, we take advantage of the relative uniformity of the anatase sample to look at the structure of different groups of anatase particles after a prescribed exposure to gas and light. After the initial period of light exposure, an initial set of anatase particles was examined. After a second period of light exposure, a second set of fresh anatase crystals, not previously exposed to the electron beam, was examined. This procedure (condition B from Table 3.1) was then repeated and allowed us to completely eliminate electron-beam effects during the *in situ* processing of the anatase.

Figure 3.3a shows results from experiments in condition B in which anatase particles were exposed to H_2O vapor and light. Disordered monolayers were observed on the anatase (101) and (002) surfaces after 12hrs. The first one or two layers at the anatase surface show roughening and amorphization. Over 30 fresh areas which were not previously exposed to the electron-beam were checked and all showed some degree of surface amorphization and roughness. The surface transformation was similar to those observed during electron-beam irradiation in H_2O suggesting that, at least in this case, the underlying transformation processes may be similar. Indeed, the total energy deposition during the electron-irradiation experiment and the extended irradiation in light were comparable.

Figure 3.4 shows the result of exposing anatase nanocrystals to light in a H_2 atmosphere. Once again only fresh anatase crystals which had not been previously exposed to the electron beam were examined. Even after 40 hours of light exposure, the crystal surface remained fairly smooth and showed no significant change in the surface crystallography. This shows that water plays a critical role in the observed phase change on the anatase surface.

3.4 Mechanisms of Surface Amorphization under Exposure to H_2O and Light

Spatially-resolved electron energy-loss spectroscopy on an aberration-corrected JEOL ARM 200F was performed to compare the oxidation state of the Ti in the center and surface of the anatase particle. The Ti L_{23} edges are shown in Figure 3.5a. The L_{23} edge from the center of the anatase shows the characteristic crystal-field splitting in which the L_3 line at 457 eV and L_2 line at 459 eV are split into doublets corresponding to excitations of the $2p_{3/2}$ and $2p_{1/2}$ subshells to unoccupied t_{2g} and e_g orbitals. The Ti L_{23} edge recorded from the surface layer shows pronounced broadening of the L_3 and L_2 lines and the relative peak height is consistent with Ti in the +3 oxidation state [24].

As a further check on the oxidation state of the anatase surface, X-ray photoelectron spectroscopy (XPS) was performed on a sample first calcined at 300^{o}C and then exposed to water vapor at room temperature (100% humidity) in a flux of 5mW/cm^2 of UV light (254 nm) for 2 hours. As a control, XPS was also performed on the calcined sample without water and light exposure (Figure 3.5b). The XPS from the sample exposed to water and light showed a secondary peak corresponding to Ti in the +3 state whereas the unexposed sample showed mainly a +4 oxidation state. The sample exposed to water and

light also showed broadening of the Ti 2p and O 1s peaks suggesting an increased variation in the bonding environments at the surface and thus more dispersion in the bonding energies. This would be consistent with the introduction of disorder in the surface of the anatase. The XPS showed changes similar to those determined with EELS suggesting that similar changes have taken place on the surface of the anatase nanoparticles even on exposure to water vapor at room temperature at atmospheric pressure.

The question arises about whether the observed amorphization is intrinsic to the hydroxylated layer or is a result of rapid electron-beam damage taking place during the time required to record the high-resolution image. To address this question, we make the assumption that it is possible to have an ordered hydroxilated structure on the surface of the titania. Electron-beam damage to the surface during imaging can occur either through radiolysis (inelastic collisions) or knock-on processes (elastic collisions). An analysis given in the appendix II shows that the cross section for radiolytic damage is many orders of magnitude greater than the cross section for knock-on damage. Moreover, if the ordered structure can be easily damaged by ionization with the electron beam, it will almost certainly be damaged by ionization with UV radiation. This suggests that the disorder structure observed by electron microscopy is not a consequence of electron irradiation but is caused by the combination of UV irradiation and water.

The observed surface amorphization and roughness can be explained by the photogeneration of oxygen vacancies and the resulting dissociation of water at these defect sites. The initial mechanism is illustrated schematically in Figure 3.6. For truncated TiO_2 surfaces, there are always 5-coordinated Ti sites and 2-coordinated bridging oxygen sites which are more reactive than the 6-coordinated Ti and 3-coordinated O sites in the bulk.

On exposure to UV light or high energy electrons, electron-hole pairs are generated which may diffuse to the crystal surface. The photogenerated electrons tend to reduce Ti^{4+} to Ti^{3+}, while trapped holes neutralize surface oxygen leading to emission from the surface and leaving behind oxygen vacancies [25]. High-resolution electron energy-loss spectroscopy (HREELS) and temperature-programmed desorption (TPD), have confirmed that water molecules are dissociatively adsorbed filling the vacancies forming hydroxyl groups [26]. Scanning tunneling microscopy (STM) results and density functional theory (DFT) calculation suggests that one bridging hydroxyl group at the original vacancy site and another at the adjacent bridging oxygen position are formed [10-12].

With continued irradiation, the degrees of hydroxylation of the surface increase and eventually destabilize the crystallinity of the top layer leading to the formation of a continuous amorphous layer of hydroxilated titania. We also believe this observation is related to the photo-induced hydrophilic effect in which the surface OH groups help to attract more water via hydrogen bonding [27, 28]. No amorphous layer was observed to form during irradiation in the presence of hydrogen. In principle, hydrogen could directly react with surface oxygen leading to hydroxylation of the surface. However, apparently, the hydrogen is not activated on the bare titania surface at 150^{o}C [29].

Our observations show that this process is self-limiting because the thickness of the disordered layer remains constant under continuous exposure to water and light. This is reasonable because anatase is known to be a stable photocatalyst in an aqueous environment during exposure to light. Continued irradiation of the hydroxilated surface will presumably result in the generation of additional oxygen vacancies on the surface. Since the amorphous layer thickness does not significantly increase with time, this implies

that most of these vacancies are filled by additional dissociation of water from the gas phase rather than by diffusion of oxygen from the interior of the anatase particle. Thus, the underlying bulk structure of the anatase is preserved although our TEM images show that the TiO_2 layer just below the surface is significantly perturbed by the amorphous top layer.

3.5 Summary

This chapter has summarized the first atomic-resolution study of the surface of anatase nanocrystals under conditions relevant to gas-phase photocatalytic splitting of water. The experiments were carried out in a modified environmental transmission electron microscope fitted with a high-intensity broadband light source. When the titania is exposed to light and water vapor, the initially crystalline surface converts to an amorphous phase one to two monolayers thick. EELS and XPS analysis show that the amorphous layer contains titanium in a +3 oxidation state. Similar changes were observed to occur under electron irradiation under conditions in which the total energy adsorbed in the anatase was held constant. From the time evolution of the electron-irradiated crystal, we were able to show that the amorphous layer results from direct photoreaction between the top one or two monolayers of the anatase crystal surface and adsorbed water. The amorphous layer appears to be stable and does not increase in thickness even after 60 hours exposure to reaction conditions. The surface layer shows no long-range order and is most likely a stabilized form of titania hydroxide. The amorphous layer is stable and does not increase in thickness with time and is heavily hydroxylated. This disorder layer will be present on the anatase surface under reaction conditions relevant to photocatalytic splitting of water.

In future work, we will investigate the changes taking place on functionalize titania and on other photocatalytic materials with enhanced absorption in the visible.

References:

1. Lu, D., Takata, T., Saito, N., Inoue, Y., Domen, K. (2006). Photocatalyst releasing hydrogen from water. *Nature*, 440, 295.

2. Maeda, K., Teramura, K., Domen, K. (2008). Effect of post-calcination on photocatalytic activity of $(Ga_{1-x}Zn_x)(N_{1-x}O_x)$ solid solution for overall water splitting under visible light. *Journal of Catalyst*, 254 (2),198−204.

3. Reece, S. Y., Hamel, J. A., Sung, K., Jarvi, T. D., Esswein, A. J., Pijpers, J. J. H., & Nocera, D. G. (2011). Wireless solar water splitting using silicon-based semiconductors and earth-abundant catalysts. *Science*, 334 (6056), 645−648.

4. Chen, X., & Mao, S. S. (2007). Titanium dioxide nanomaterials: synthesis, properties, modifications, and applications. *Chemical Review*, 107, 2891−2959.

5. Awazu, K., Fujimaki, M., Rockstuhl, C., Tominaga, J., Murakami, H., Ohki, Y., Yoshida, N., & Watanabe, T. (2008). A plasmonic photocatalyst consisting of silver nanoparticles embedded in titanium dioxide. *Journal of American Chemical Society*, 130, 1676−1680.

6. Slamet, Nasution, H. W., Purnama, E., Kosela, S., & Gunlazuardi, J. (2005). Photocatalytic reduction of CO_2 on copper-doped Titania catalysts prepared by improved-impregnation method. *Journal of Catalyst Community,* 6, 313−319.

7. Tseng, I. H., & Wu, J. C. S. (2004). Chemical states of metal-loaded titania in the photoreduction of CO_2. *Catalysis Today*, 97, 113−119.

8. Fujishima, A., Zhang, X. T., & Tryk, D. A. (2008). TiO_2 photocatalysis and related surface phenomena. *Surface Science Reports*, 63(12), 515−582.

9. Henderson, M. A. (1996). An HREELS and TPD study of water on TiO_2 (110): the extent of molecular versus dissociative adsorption. *Surface Science*, 355, 151−166.

10. Bikondoa, O., Pang, C. L., Ithnin, R., Muryn, C., Onishi, H., & Thorton, G. (2006). Direct visualization of defect-mediated dissociation of water on TiO_2 (110). *Nature Materials*, 5, 189−192.

11. Wendt, S., Matthiesen, J., Schaub, R., Vestergaard, E. K., Lagsgaard, E., Besenbacher, F., & Hammer, B. (2006). Formation and Splitting of Paired

Hydroxyl Groups on Reduced TiO_2 (110). *Physical Review Letter*, 96, 066107.

12. Wendt, S., Schaub, R., Matthiesen, J., Vestergaard, E. K., Wahlstrom, E., Rasmussen, D., Thorstrup, P., Molina, L. M., Lagsgaard, E., Stensgaard, I., Hammer, B., & Besenbacher, F. (2005). Oxygen vacancies on TiO_2 (110) and their interaction with H_2O and O_2: A combined high-resolution STM and DFT study. *Surface Science*, 598, 226−245.

13. Zhang L., Miller B. K. & Crozier P.A. (2013). Atomic level in situ observation of surface amorphization in anatase nanocrystals during light irradiation in water vapor. *Nano Letters*, 13(2), 679–684.

14. Zhu, H. Y., Lan, Y., Gao, X. P., Ringer, S. P., Zheng, Z. F., Song, D. Y., & Zhao, J. C. (2005). Phase transition between nanostructures of titanate and titanium dioxides via simple wet-chemical reactions. *Journal of American Chemical Society*, l (127), 6730−6736.

15. Deng, Q., Wei, M., Hong, Z., Ding, X., Jiang, L., & Wei, K. (2010). Selective synthesis of rutile, anatase, and brookite nanorods by a hydrothermal route. *Nanoscience*. 6, 479−482.

16. Banerjee, R., Crozier, P.A. (2012*). In situ* synthesis and nanoscale evolution of model supported metal catalysts: Ni on silica. *Journal of Physical Chemistry C*, 116 (21), 11486−11495.

17. Crozier, P. A., McCartney, M. R., & Smith, D. J. (1990). Observation of exit surface sputtering in TiO_2 using biased secondary electron imaging. *Surface Science.* 237 (1−3), 232−240.

18. McCartney, M. R., Crozier, P. A., Weiss, J. K., & Smith, D. J. (1991). Electron-beam-induced reactions at transition-metal oxide surfaces. *Vacuum*. 42 (4), 301−308.

19. Wang, L. Q., Baer, D. R., & Engelhard, M. H. (1994). Creation of variable concentrations of defects on TiO_2 (110) using low-density electron beam. *Surface Science*, 320,295−306.

20. Shultz, A. N., Jang, W., Hetherington, W. M., Baer, D. R., Wang, L. Q., & Engelhard, M. H. (1995). Comparative second harmonic generation and X-ray photoelectron spectroscopy studies of the UV creation and O_2 healing of Ti^{3+} defects on (110) rutile TiO_2 surfaces. *Surface Science.* 1995, 339, 114−124.

21. Wang, L. Q., Baer, D. R., Engelhard, M. H., & Shultz, A. N. (1995). The adsorption of liquid and vapor water on TiO_2 (110) surfaces: the role of defects. *Surface Science*. 344, 237−250.

22. Egerton, R. F. (2011). Electron Energy-Loss Spectroscopy in the Electron Microscope, 3rd ed.; Springer; New York.

23. Wang, Z., Helmersson, U., Kall P. (2002). Optical properties of anatase TiO_2 thin films prepared by aqueous sol–gel process at low temperature. *Thin Solid Film*, 405, 50-54.

24. Muller, D., Nakagawa, N., Ohtomo, A., Grazul, J., & Hwang, H. (2004). Atomic-scale imaging of nanoengineered oxygen vacancy profiles in $SrTiO_3$. *Nature*. 430, 657−661.

25. Sakai, N., Fujishima, A., Watanabe, T., & Hashimoto, K. (2001). Enhancement of the photoinduced hydrophilic conversion rate of TiO_2 film electrode surfaces by anodic polarization. *Journal of Physical Chemistry B*, 105 (15), 3023–3026

26. Henderson, M. A. (1996). Structural sensitivity in the dissociation of water on TiO_2 single-crystal surface. *Langmuir*, 12, 5093−5098.

27. Wang, R., Hashimoto, K., Fujishima, A., Chikuni, M., Kojima, E., Kitamura, A., Shimohigoshi, M., & Watanabe, T. (1998). Photogeneration of Highly Amphiphilic TiO_2 Surfaces. *Advanced Materials*, 10(2), 135−138.

28. Watanabe, T., Nakajima, A., Wang, R., Minabe, M., Koizumi, S., Fujishima, A., & Hashimoto, K. (1999). Photocatalytic activity and photoinduced hydrophilicity of titanium dioxide coated glass. *Thin Solid Films*, 351, 260−263.

29. Varghese, O. K., Gong, D., Paulose, M., Ong, K. G., Dickey, E.C., & Grimes, C. A. (2003). Extreme changes in the electrical resistance of titania nanotubes with hydrogen exposure. *Advanced Materials*, 15 (7−8),624−627.

Experiments	Temperature	Atmosphere	Light
Condition A	**150 ℃**	**H_2O gas (1 Torr)**	**Absent**
Condition B	**150 ℃**	**H_2O gas (1 Torr)**	**Full spectrum 1430mW/cm^2**
Condition C	**150 ℃**	**H_2 gas(0.5 Torr)**	**Full spectrum 1430mW/cm^2**

Table 3.1 Experiments conditions for *in-situ* characterization of anatase TiO_2.

Flux of electrons	**3000 e$^-$/Å^2/s**
Flux of Photons (E>Eg)	**390 photons/ Å^2 /s (18 photons/ Å^2/s for E>Eg)**
Incident Electron Power Density	**1 MW/cm^2**
Incident Photon Power Density	**1430mW/cm^2 (122mW/cm^2 for E>Eg)**
Electron Energy Absorbed (estimated acquisition time 100s)	**3000J/cm^2**
Photon Energy Absorbed (exposure time 12hours)	**2820J/ cm^2**

Tabel 3.2 Table of Relevant Irradiation Parameters for *in-situ* experiments.

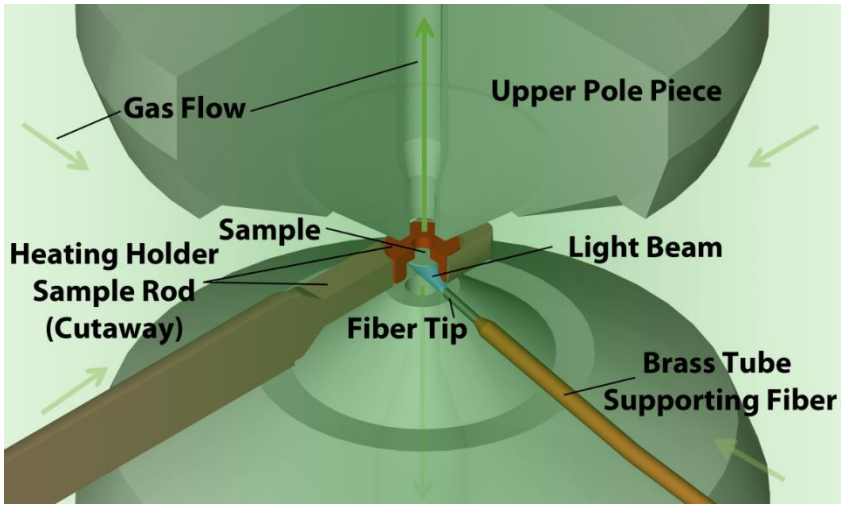

Figure 3.1. Schematic diagram on *in situ* TEM showing geometry of gases flows, light illumination and sample holder [13].

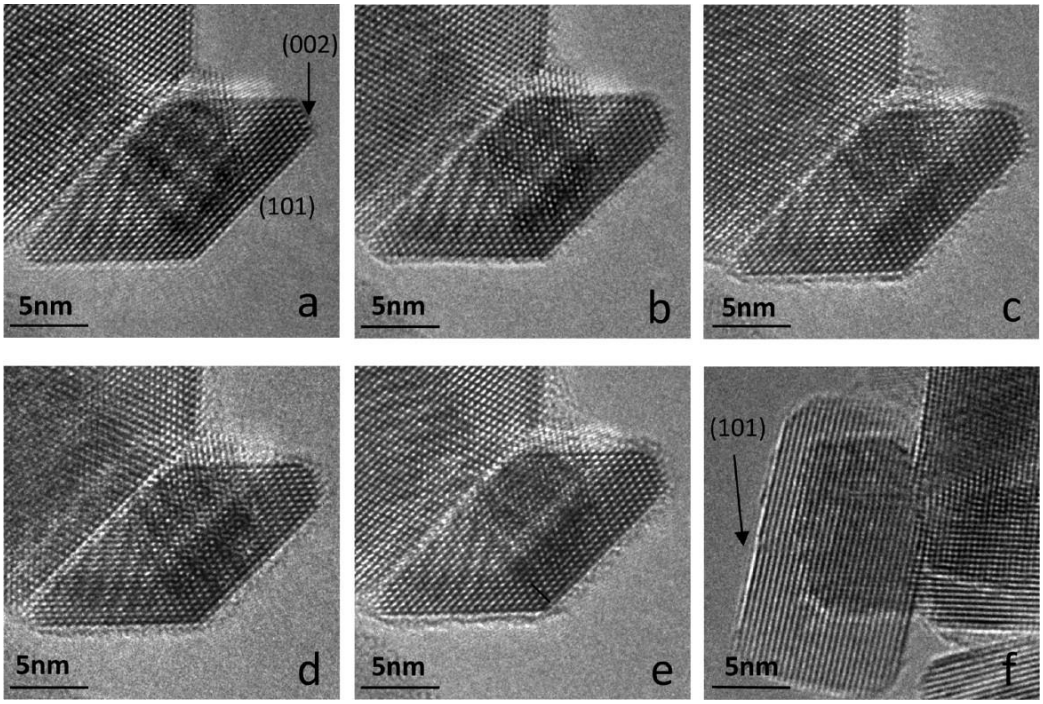

Figure 3.2. Anatase particles at 150 ℃ with/without 1 Torr water: (a)no water; (b)1hr water; (c)7hrs water; (d)20hrs water; (e)40 hrs water; (f) fresh area after 40hrs in water gas but not exposed to electron beam before.

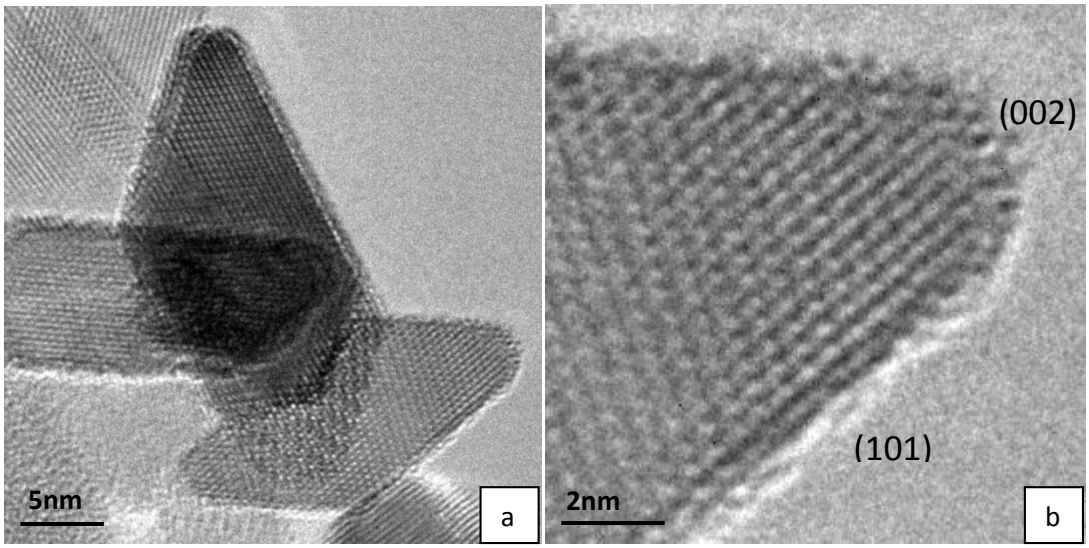

Figure 3.3 (a) Fresh anatase particles after 40 hrs in H_2O gas at 150 ℃, light exposure 12hrs; (b) magnified images of the (101) & (002) surfaces after illumination.

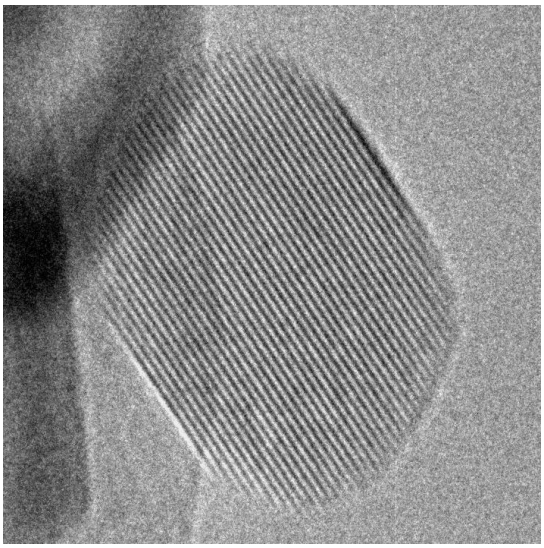

Figure 3.4. Fresh anatase particles after 40hrs in H_2 at 150 ℃, with 20hrs light exposure.

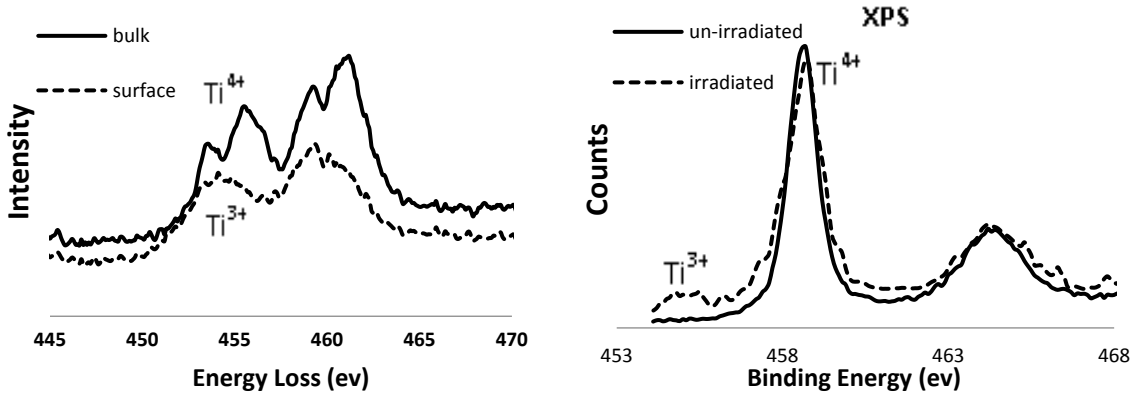

Figure 3.5 (a)EELS spectra from surface and bulk of the irradiated anatase samples; (b) XPS spectra of the irradiated and un-irradiated anatase samples.

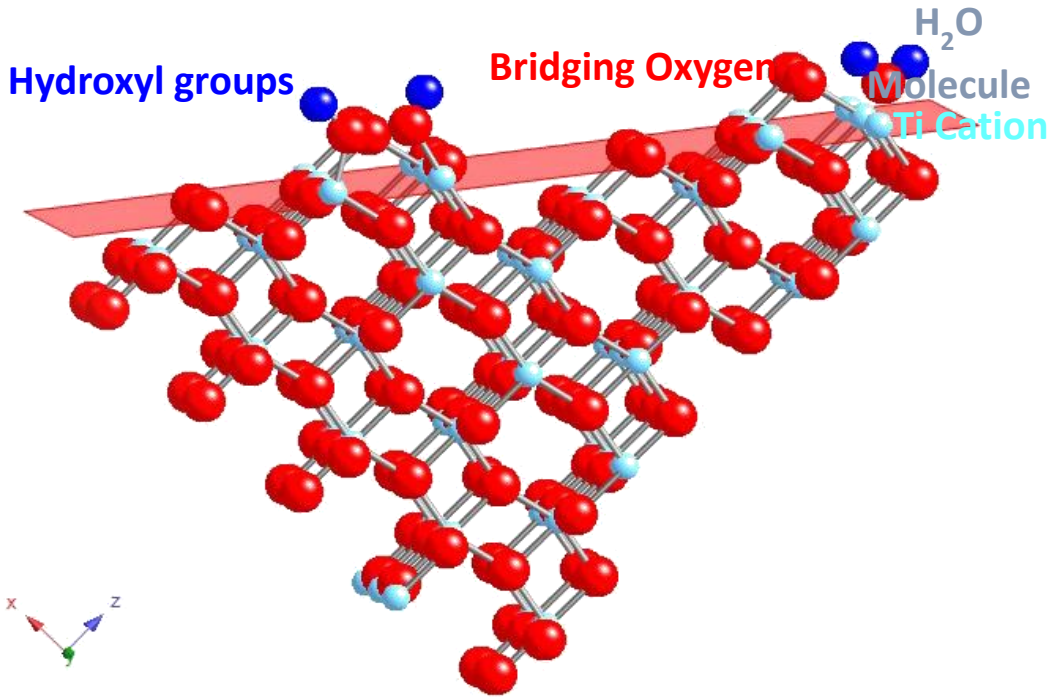

Figure 3.6. Schematic drawing of H_2O molecules dissociatively absorbed on anatase 101 planes forming hydroxyl groups.

CHAPTER 4

PHOTOINDUCED OSTWALD RIPENING OF Pt CO-CATALYST NANOPARTICLES ON TiO_2 FOR WATER SPLITTING

4.1 Introduction

With the success of *in situ* observation of just pure anatase samples, Pt co-catalyst as a good example for noble metal co-catalyst on seminconductor photocatalysts, will be explored for its structure evolution during photocatalysis reactions. Substantial efforts have been taken to improve the photocatalytic properties by functionalizing semiconductors with metal co-catalysts [1-3]. The metal co-catalysts can improve catalyst performance in two ways. They may attract the photoelectrons generated in the semiconductor to impede electron-hole pair recombination if the Fermi level of the metal lies below the conduction band-edge of the oxide [4,5]. Metal particles such as Pt also act as reduction catalysts via electron transfer to adsorbed protons, reducing them to H_2 which then desorbs from the surface [6]. The noble metal co-catalyst was believed to be efficient and stable. However, our observation revealed they are not so stable at nano scale that they have undergone photo-induced coarsening with resulting drop of catalytic properties.

When Pt nanoparticles are used as catalysts, the high surface areas associated with excess surface energy makes the system susceptible to coarsening, leading to deactivation due to loss of surface area [7, 8].For example, Pt sintering at high temperature is a key factor in deactivation for autocatalyst dealing with vehicle exhaust [9,10]. Moreover,

coarsening caused by dissolution and re-deposition of Pt nanoparticles on both the cathode and anode of proton exchange membrane fuel cells (PEMFC) are considered the main reason for deactivation of low-temperature fuel cells [11, 12]. These applications have motivated a great deal of research on processes affecting Pt particle coarsening due to thermal effects at high temperature and electro-chemical Ostwald ripening of Pt on electrodes at room temperature [13-17]. These studies provide a fundamental understanding of the way in which ripening occurs under a variety of thermal and electrochemical reaction conditions and may suggest approaches to slow or mitigate de-activation.

Considerably less work has been carried out on coarsening effects taking place on co-catalyst under photoreaction conditions in water. Here we investigate the materials changes that take place on Pt/TiO_2 photocatalysts performing water splitting with particular emphasis on the Pt-particle size evolution. TiO_2 was selected as the light-harvesting component because it is stable under reaction conditions, the catalyst is reasonably active and the changes in the Pt co-catalyst can be followed with electron microscopy. A Pt loading of 2 wt% was selected to minimize back reactions and light shadowing by the metal [18, 19]. We employed aberration-corrected *ex situ* transmission electron microscopy (TEM) and *in situ* environmental transmission electron microscopy (ETEM) to follow the evolution of the catalyst under liquid and vapor-phase water-splitting conditions. The observed coarsening is interpreted in terms of an Ostwald ripening model and correlated with the drop in H_2 evolution from the photocatalysts.

4.2. Materials Preparation

2 wt % Pt on high-surface-area anatase TiO_2 nanoparticles was prepared with a wet chemical impregnation method. The high surface area anatase particles were prepared following a hydrothermal method described in another paper [20]. The TiO_2 particles were suspended into 20 ml calculated concentration $PtCl_4$ (Sigma-Aldrich, 99.99%) aqueous solutions, stirred and dried. The particles were then calcined in air @500 ℃ for 3 hrs followed by a reduction in flowing 2% H_2/Ar @500 ℃ for 2 hrs.

The morphology of as prepared 2 wt% Pt on anatase was checked on aberration corrected FEI Titan microscope and is shown in Figure 4.1. Pt particles with 1-2 nm size are well dispersed on TiO_2 nanoparticles. Lattice fringes of 2.27 Å are observed on the particles which match the Pt (111) fringes. The Pt particles are not uniformly or randomly distributed on the surfaces of the TiO_2 support. Most of the Pt particles prefer to nucleate and grow at high surface energy sites including corners and steps as marked on the figure where suface support atoms are less coordinated.

4.3 Photocatalytic Performance

20 mg of the as-prepared 2 wt% Pt/TiO_2 materials were suspended in 50 ml de-ionized H_2O for the test of photocatalytic H_2 production. A 450W xenon lamp (Newport) with a 350-450nm band pass mirror was used as the light source with the light coming vertically through the top quartz window of the reactor. According to the manufacturer's manual, the incident light intensity into the reactor is about 50 mW/cm^2 and this was confirmed by a Si-biased photo detector (THORLABS DET10A). H_2 was detected using a gas-chromatography (GC) (Varian 450-GC) system connected to the photoreactor with Ar as the carrier gas continuously flowing at 5 cc/ min.

The H_2 production rate is plotted as in Figure 4.2. The maximum H_2 production rate reaches about 29 μmol/hr/g in about 80 minutes. This relates to the fact that H_2 has to reach saturation concentration, get released to the head space and then mix fully with Ar carrier gas. The photocatalyst starts to deactivate after the first 90 minutes with the H_2 production dropping fast in the following 2 hrs and then a more gradual drop to about 1/3 of the maximum production rate after 9 hrs light irradiation. In a separate experiment using He as the carrier gas, O_2 was detected proving the Pt/TiO_2 is doing water splitting, producing both H_2 and O_2 from neutral de-ionized water.

4.4 Structure Evolution during Reactions and Photo-induced Ostwald Ripening

Figures 4.3 shows a high-resolution TEM image of Pt/TiO_2 after 5 hrs light irradiation in pure water. The TiO_2 particles have significant surface roughening because the surface has been heavily hydroxylated, as described in Chapter 3 [20]. The fast Fourier transformation (FFT) of the TEM image shows spots representing 2.27 Å lattice fringes belonging to Pt (111). The Pt particles have gone through an obvious coarsening comparing to the fresh as-prepared sample shown in Figure 4.1.

The drop in the photocatalytic H_2 production rate may be simply related to the decrease of the Pt surface area due to coarsening. To achieve a quantitative surface area change from coarsening, high-angle annular dark-field imaging (HAADF) in a scanning transmission electron microscope (STEM) was employed to achieve more precise Pt particle sizes [21, 22]. This technique provides a clearer view of heavy metal Pt particle dispersion on a medium-atomic-number support like TiO_2. HAADF images were taken on a series of samples for fresh material and materials after 3hrs, 7hrs and 12hrs of

photocatalytic water splitting. The coarsening is very obvious by comparing the image from the 12 hrs light exposure sample and the initial fresh sample as seen in Figure 4.4. Over 300 particle sizes were measured from 15 to 20 images for each sample and particle size

Histograms in Figure 4.5 show a gradual particle size growth during the total light exposure after 3hrs, 7hrs, and 12 hrs in pure H_2O. The specific surface area (area per unit mass) for each sample was calculated by dividing the total surface area by the total mass of measured particles (each particle was treated as a hemisphere). Particle sizes and surface areas for each sample are summarized in Table 4.1. The average particle size increases from value of 1.69 nm ± 0.05 nm to a final value in 12 hrs of 2.06 nm ± 0.09 nm. (The error is taken to be three times the standard error in the mean). The specific surface area drops by a factor of 1.3 compared to its initial value after 12 hours reaction. H_2 production rate drops considerably faster with a factor of more than 3 after 9 hours of reaction. This suggests that, in addition to the surface area decrease, some other factors also contribute to the drop of photocatalytic properties.

Control experiments have also been carried out in the dark to prove that the coarsening is faster in the presence of light. The particle size distribution of a sample exposed to liquid water in dark for 12hrs is compared with a fresh catalyst and the result is shown in Figure 4.6. The particle size distribution is similar to the fresh sample with an average size to be 1.66 ± 0.05 nm.

Inductively-coupled plasma mass spectrometry (ICP-MS) was carried out to measure the time-dependent Pt concentration in solution. Combining the Pt concentration

determined by ICP-MS with the mass of catalyst used in the solution allows the percentage of the Pt^{2+} in solution to be calculated relative to the total mass of Pt. The results are summarized in Table 4.2 (in the table 100% is equivalent to 2 wt% Pt). The initial relative concentration of Pt^{2+} in solution is comparatively high, around 1 %, presumably as a result of residual soluble Pt chloride species from the chloride precursor which remained on the support even after the thermal reduction treatment. The Pt concentration drops quickly after the light is turned on because of photo-deposition and reaches less than 0.01% after 5 hours. The photo-deposition of the initial 1% relative concentration of Pt from solution onto the support cannot explain the observed particle size increase. To increase the mean particle size from 1.7nm to 1.8nm would require 20% additional mass deposition from solution, which is a factor of 20 higher than the measured Pt concentration. The concentration of the Pt^{2+} stays low and relatively constant after 5 hours during light irradiation which indicates that the particle size increase is not due to simple dissolution of small Pt particles. However, the observation of constant low concentration of Pt^{2+} in solution suggests a possible coarsening mechanism in which small Pt particles are initially oxidized to Pt^{2+} cations, and then re-deposited onto larger Pt particles.

Similar ageing experiments were performed on the same material using-vapor phase water. An *in situ* characterization of this Pt/TiO_2 sample in 17 Torr H_2O vapor under prolonged light irradiation was conducted in our environmental TEM Tecnai F20 with light irradiation system [20, 23]. Typical images showing the same area of the catalyst before and after exposure to water and light in Figure 4.7. There was no obvious

difference in the average particles size after up to 11 hrs light exposure. The coarsening was not observed presumably because vapor-phase H_2O cannot provide the pathway for Pt^{2+} to be transferred from small Pt to large Pt particles. In water-vapor Pt, mass transport cannot take place via dissolution, and presumably transport via diffusion across the TiO_2 surface is very slow under these photoreaction conditions.

4.5 Mechanism

The deactivation we observed is believed to result from the light-induced coarsening. The decrease of the surface area represents a decrease of surface reaction sites, which contributes to the drop of photocatalytic H_2 production. An additional decrease of the photocatalytic activity may also arise because the large particles provide-less overpotential for charge transfer to reactants. We hypothesize that the coarsening mechanism is a photo-electro-chemical Ostwald ripening. Ostwald ripening is a particle-coarsening process involving thermodynamically less stable small particles that, via kinetic pathways such as surface diffusion, volume diffusion or dissolution/deposition, transform to large particles. The driving force for this is the particle-size dependent chemical potential set by the surface-to-volume ratio of nanoscale particles. From an atomistic view, particles with smaller size have a larger number of under-coordinated atoms so there is a higher probability that these atoms can detach from the particle surface and migrate across a support or dissolve into solution. This leads to a net transfer of atoms from the small particles to the large particles resulting in time-dependent increases in the average particle size.

The initial concentration of Pt detected by ICP-MS and the use of the chloride precursor suggests that there is $PtCl_4^{2-}$ in solution. As discussed in detail by Tang et al., for a finite-sized single-component solid of radius *r* in equilibrium with a fluid phase containing that component (e.g., Pt^{2+}/Pt equilibrium), there is a difference in the chemical potentials of the component in the solid and fluid phases given by,

$$\mu_s - \mu_l = (f - \gamma)\Omega(2/r) \tag{4.1}$$

where f is the solid/fluid interface stress (assumed isotropic), γ is the solid/fluid interfacial free energy (assumed isotropic) and Ω is the molar volume of the solid [24]. For the reaction, $PtCl_4^{2-} + 2e^- = Pt + 4Cl^-$, (E=0.755 V., NHE), the chemical potential of Pt in the liquid phase is given by

$$\mu_l = \bar{\mu}_l\left(\overline{PtCl_4}^{2-}\right) + RTln(PtCl_4^{2-}/\overline{PtCl_4}^{2-}), \tag{4.2}$$

where the bar quantity indicates the saturation concentration associated with a planar ($r = \infty$) surface at equilibrium. The chemical potential of the Pt in the solid is given by

$$\mu_s = \bar{\mu}_l\left(\overline{PtCl_4}^{2-}\right) + f_{Pt}\Omega_{Pt}(2/r). \tag{4.3}$$

Using the equilibrium condition of eq(1) we obtain,

$$RTln(PtCl_4^{2-}/\overline{PtCl_4}^{2-}) = \gamma_{Pt}\Omega_{Pt}(2/r). \tag{4.4}$$

The left-hand side of this equation is the Gibbs free-energy difference for Pt in the liquid phase surrounding a Pt particle of radius *r* and that for a planar surface. Since $\Delta G = -nFE$, we obtain

$$E_{PtCl_4^{2-}}(r) = \overline{E}_{P_tCl_4^{2-}} - \gamma_{Pt}\Omega_{Pt}/Fr \quad (4.5)$$

where $\overline{E}_{P_tCl_4^{2-}}$ is the electrode potential for a planar surface; $E_{P_tCl_4^{2-}}(r)$ is the electrode potential for a particle with radius *r* surrounded by liquid phase; γ_{Pt} is the surface energy ; Ω_{Pt} is the molar volume of *Pt* and *F* is the Faraday constant [24]. From our ICP analysis, we estimate that the concentration of $PtCl_4^{2-}$ is ~ 10^{-7} giving a value of $\overline{E}_{P_tCl_4^{2-}} \sim 0.55V$. Taking $\gamma_{Pt} = 2.4$ Jm^{-2}, $\Omega_{Pt} = 9.09 \times 10^{-6}$ m^3, we obtain

$$E_{PtCl_4^{2-}}(r) \sim 0.55 - 0.23/\mathrm{r} \quad (4.6)$$

where r is in units of nanometers [25]. The extra term for small particles compared to the planar surface has a negative shift in the standard electrode potential of 0.23/r. The distributions of the negative potential shifts for each sample can be calculated from the particle size distributions and are plotted in Figure 4.8 for each reaction time.

The electrode potential shift is plotted against particle size in Figure 4.9. For a 1 nm diameter particle, the potential for initial dissolution of Pt is shifted down by 0.46V giving $E(r) \sim +0.1V$ which is low enough to make initial oxidation of small Pt particles possible. However, dissolution of Pt will be inhibited in the dark because charge transfer through the TiO_2 is very slow (see Figure 4.10). When the light is turned on, electron-hole pairs are generated in the TiO_2 putting electrons into the conduction band and holes into the valence band increasing the titania conductivity. Without irradiation, the conductivity of anatase TiO_2 is ~10^{-7} $\Omega^{-1}m^{-1}$. It can increase to ~ 10^0 $\Omega^{-1}m^{-1}$ under UV light irradiation [26, 27]. The number of electric charges can pass a distance *L* within time *t* under voltage *V* can be calculated as $n = V\sigma Lt/e$. Using 0.1V as the voltage difference

between small and large Pt particles, 10 nm as the distance, and 10^{-6} s as the life time for photo excited electrons before recombination, we can have ~10^3 electrons transferred from small particles to large ones under irradiation but negligible transfer in dark [28]. The conductivity and lifetime will vary depending on the incident light intensity and defect densities but greatly enhanced electron transfer will take place under illumination. We conclude that during illumination, the Pt particles are electrically connected via the TiO_2 substrate which is similar to the Ag coarsening on conductive substrates reported by Redmond et al [29].

The potential shift due to the Gibbs-Thompson effect is different for particles of different sizes leading to a net difference in the electrochemical driving force of:

$$E(\mathrm{r}) - E(\mathrm{R}) = \gamma_{Pt}\Omega_{Pt}/nFR - \gamma_{Pt}\Omega_{Pt}/nFr < 0 \qquad (4.7)$$

When small and large particles are connected by the photo-excited conducting TiO_2 substrate, thermodynamically, small Pt particles with more negative potential level will give electrons to large particles. The Pt in the small particles is oxidized and to maintain charge neutrality, Pt^{2+} ions from the small particles travel through the electrolyte to the large particle. Effectively, the two particles behave like the electrodes in a Galvanic cell as described by the schematic drawing in Figure 4.10. The driving force increases as the size difference increases. This photo-electrochemical Ostwald ripening process is the mechanism which leads to the observed coarsening of the particle size distribution.

Finally, the variation in overpotential with particle size will also influence the overall catalytic activity of the system. The smaller particles have a larger potential shift resulting in greater overpotentials for electrons to transfer from Pt to protons. The change

in the H_2 production rate taking both surface area and overpotential effects into account can be quantitatively estimated as follows. The rate of electron transfer is proportional to the factor $e^{\frac{-E_b+qv}{kT}}$ where E_b is the energy barrier for electrons to transfer from a bulk Pt surface to adsorbed protons; q is the charge of electron; v is the electrode potential shift of Pt particles compared to bulk Pt (i.e. the Gibbs-Thomson term in eq(4.5); k and T are Boltzmann's constant and temperature. The H_2 production rate (per unit mass) is thus proportional to

$$\frac{\sum A_n * e^{\frac{-E_b+qv_n}{kT}}}{\sum \rho V_n} \tag{4.8}$$

where A_n, v_n, and V_n are the surface area, electrode potential shift, and volume of particle n respectively and ρ is the density of Pt. A_n, v_n and V_n can all be calculated according to the particle sizes determined from STEM images. If we compare the ratio of H_2 production for the initial and final particle size distributions, the term involving E_b cancels and we find that the H_2 production rate drops by a factor of 1.8 over 12 hours. This is larger than the factor of 1.3 obtained by considering only the surface area decrease and is closer to the experimentally observed drop of a factor of 3.

4.6 Summary

We have observed H_2 production rate dropping for Pt/TiO_2 photocatalyst due to significant surface area decrease from Pt coarsening. This coarsening was studied by series of STEM images showing particle size distribution shifting from average 1.69 ± 0.05 nm to 2.06 ± 0.09 nm. The surface area per mass was accordingly calculated to have dropped by a factor of 1.3. Very small concentrations of Pt^{2+} were detected by ICP-MS

suggesting the particle size-shifting is not due to small particles dissolution but Ostwald ripening. *In situ* experiments in H_2O vapor showing no coarsening also suggest the liquid H_2O provides the pathway for transferring Pt ions. This light-induced coarsening in water is believed to be a photo-electro-chemical Ostwald ripening effect. Quasi-equilibrium is achieved in dark when no charge transfers are available through semiconducting TiO_2. The equilibrium will be broken by light when photons excite electrons and holes turning TiO_2 connecting small Pt particles and larger ones more conductive. Large Pt particles keep on growing at the sacrifice of small ones through Pt ions transferring due to the Pt electrode potential difference between different size particles. This understanding could also be applied to other metal co-catalyst on semiconductors. (See Appendix V for Ag nanoparticle coarsening)

References:

1. Jakob, M., Levanon, H. & Kamat, P.V. (2003). Charge distribution between UV-irradiated TiO_2 and gold nanoparticles: determination of shift in the fermi level. *Nano Letters*, 3(3), 353–358.

2. Liu, S., Qu, Z., Han, X. & Sun, C. (2004). A mechanism for enhanced photocatalytic activity of silver-loaded titanium dioxide. *Catalysis Today*, 93–95, 877–884.

3. Sakthivel, S., Shankar, M.V., Palanichamy, M., Arabindoo, B., Bahnemann, D.W. & Murugesan, V. (2004). Enhancement of photocatalytic activity by metal deposition: characterization and photonic efficiency of Pt, Au and Pd deposited on TiO_2 catalyst. *Water Research*, 38, 3001–3008.

4. Subramanian, V., Wolf, E. & Kamat, P.V. (2001). Semiconductor-metal composite nanostructures: to what extent do metal nanoparticles improve the photocatalytic activity of TiO_2 films? *Journal of Physical Chemistry B*, 105, 11439–11446.

5. Anpo, M. & Takeuchi, M. (2010), The design and development of highly reactive titanium oxide photocatalysts operating under visible light irradiation. *Journal of Catalysis*, 216, 505-516

6. Greeley, J., Jaramillo, T.F., Bonde, J., Chorkendorff, I. & Nørskov, J.K. (2005) Computational high-throughput screening of electrocatalytic materials for hydrogen evolution. *Nature Materials*, 5, 909-913.

7. Wynblatt, P. & Gjostein, N.A. (1975). Supported metal crystalletes, *Progress in. Solid State Chemitry.* 9, 21-58.

8. Bartholomew, C.H. (2001). Mechanisms of catalyst deactivation. *Applied. Catalysis A*, 212, 17-60.

9. Farrauto, R.J. & Bartholomew, C.H. (1997). Fundamentals of industrial catalytic processes, Chapman & Hall, Kluwer Academic Publishers, London, Chapter 5.

10. Bell, A.T. (2003). The impact of nanoscience on heterogeneous catalysis. *Science*, 299, 1688-1691.

11. Ferreira, P.J., la O' G. J., Shao-Horn Y., Morgan D., Makharia R., Kocha S. & Gasteiger H.A.(2005). Instability of Pt/C electrocatalysts in proton exchange

membrane fuel cells: A mechanistic investigation. *Journal of. Electrochemical. Society,* 152 (A), 2256–2271.

12. Shao-Horn, Y., Sheng, W. C., Chen S., Ferreira, P. J., Holby, E. F. & Morgan, D. (2007). Instability of supported platinum nanoparticles in low-temperature fuel cells. *Topics in Catal*ysis, 46(3-4), 285-305.

13. Wanke, S.E. & Flynn, P.C. (1975), The sintering of supported metal catalysts. *Catalysis Review,* 12, 93-135.

14. Simonsen, S.B., Chorkendorff, I., Dahl, S., Skoglundh, M., Sehested, J. & Helveg, S. (2011). Ostwald ripening in a Pt/SiO_2 model catalyst studied by i*n situ* TEM. *Journal of Catalysis,* 281,147–155.

15. Asoro, M.A., Kovar, D., Shao-Horn, Y., Allard, L.F. & Ferreira, P.J. (2010), Coalescence and sintering of Pt nanoparticles:in situ observation by aberration-corrected HAADF STEM. *Nanotechnology*, 21, 025701 (6pp).

16. Harris, P.J.F. (1986). The sintering of platinum particles in an alumina-supported catalyst: further transmission electron microscopy studies. *Journal of Catalysis*, 97(2), 527–542.

17. Parthasarathy, P. & Virkar, A.V. (2013). Electrochemical Ostwald ripening of Pt and Ag catalysts supported on carbon, *Journal of Power Sources*, 234, 82-90.

18. Ohtani, B., Iwai, K., Nishimoto, S. & Sato, S. (1997). Role of platinum deposits on titanium (IV) oxide particles: structural and kinetic analyses of photocatalytic reaction in aqueous alcohol and amino acid solutions. *Journal of Physical Chemistry B,* 101, 3349-3359.

19. Sayama, K. & Arakawa, H. (1997). Effect of carbonate salt addition on the photocatalytic decomposition of liquid water over catalyst. *Journal of Chemical Society, Faraday Transactions*, 93(8), 1647-1654.

20. Zhang L., Miller B. K. & Crozier P.A. (2013). Atomic level in situ observation of surface amorphization in anatase nanocrystals during light irradiation in water vapor. *Nano Letters,* 13(2), 679–684.

21. Treacy, M. M. J. & Howie, A. (1980). Contrast effects in the rransmission electron microscopy of supported crystalline catalyst particles. *Journal of Catalysis,* 63, 265-269.

22. Treacy, M. M. J., Howie, A. & Wilson, C. J. Z. (2006). Contrast of platinum and palladium catalysts. *Philosophical Magazine. A,* 38(5), 569-585.

23. Miller, B.K. & Crozier, P.A (2013). System for in *situ* UV-Visible illumination of ETEM samples. *Microscopy and Microanalysis*, 19(2), 461-469.

24. Tang, L., Li, X., Cammarata, R. C., Friesen, C. & Sieradzki, K. (2010). Electrochemical Stability of Elemental Metal Nanoparticles. *Journal of American Chemical Society*, 132, 11722-11726.

25. Diebold, U. (2003). The Surface Science of Titanium Dioxide**.** *Surface Science Reports*, 48, 53-229.

26. Pomoni, K., Sofianou, M.V., Georgakopoulos, T., Boukos, N. & Trapalis, C. (2013). Electrical Conductivity Studies of Anatase TiO_2 with Dominant Highly Reactive {001} Facets. Journal of Alloys Compounds. 548, 194-200.

27. Watanabe, Y., Muramoto, Y. & Shimizu, N.(2011) Electronic Conduction Properties of TiO_2 Thin Films Under UV Light Irradiation. *Annual Report Conference on Electrical Insulation and Dielectric Phenomena (CEIDP)*, 117-120.

28. Fujishima, A., Zhang, X. & Tryk, D. A. (2008). TiO_2 Photocatalysis and Related Surface Phenomena. *Surface Science Reports*. 63, 515-582.

29. Redmond, P. L., Hallock, A. J., & Brus, L. E. (2005). Electrochemical ostwald ripening of colloidal Ag particles on conductive substrates. *Nano Lett*ers, 5(1), 131- 135.

	fresh	3hrs	7hrs	12hrs
average particles size (nm)	1.69±0.05	1.77±0.07	1.93±0.07	2.06±0.09
surface area (m^2/g)	157	144	133	121

Table 4.1. Average particle sizes and surface areas per mass during different time period of irradiation.

Irradiation Time	Pt^{2+} Concentration (ppb)	% of Pt dissolved into H_2O
Initial	114.47	1.43%
1 hour	6.88	0.08%
3 hour	3.99	0.05%
5 hour	0.36	below 0.01%
7 hour	0.50	below 0.01%
12 hour	1.21	below 0.01%

Table 4.2. Pt^{2+} concentration in H_2O during different time periods of light irradiation.

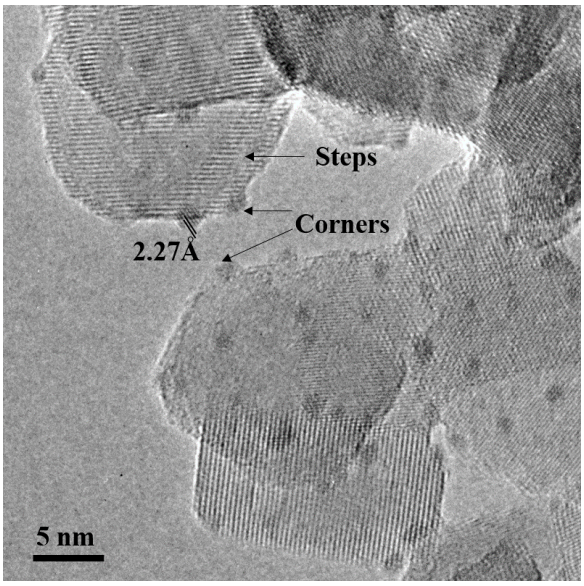

Figure 4.1. TEM image of as prepared 2 wt% Pt/TiO_2.

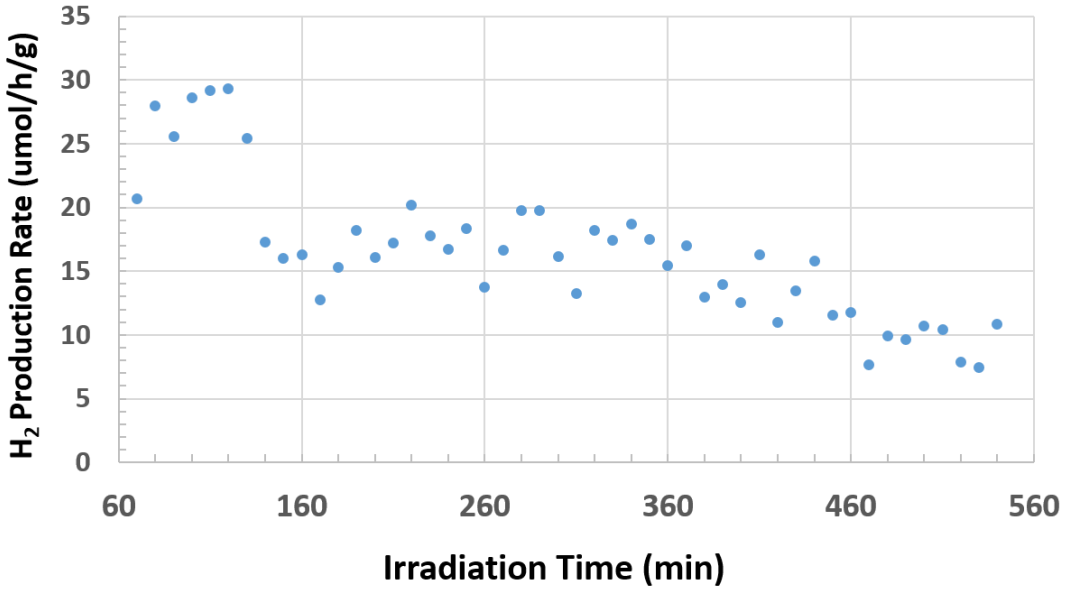

Figure 4.2. H_2 production rate vs light irradiaton time.

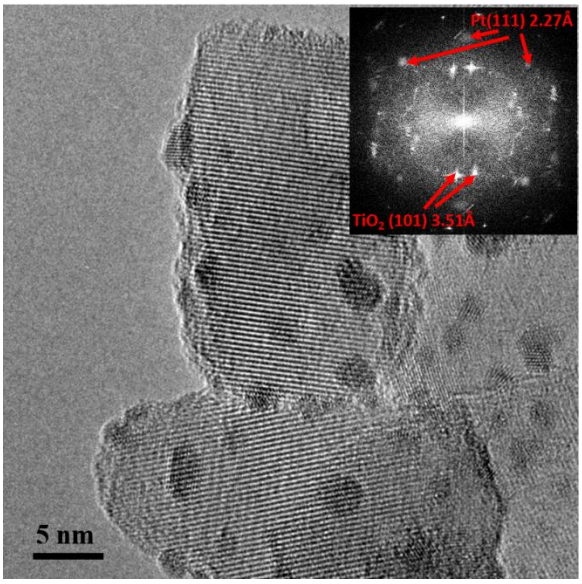

Figure 4.3. HRTEM image of 2%wt Pt/TiO_2 after 5 hrs light irradiation in pure H_2O with the insertion FFT of the TEM showing Pt (111) lattice fringes.

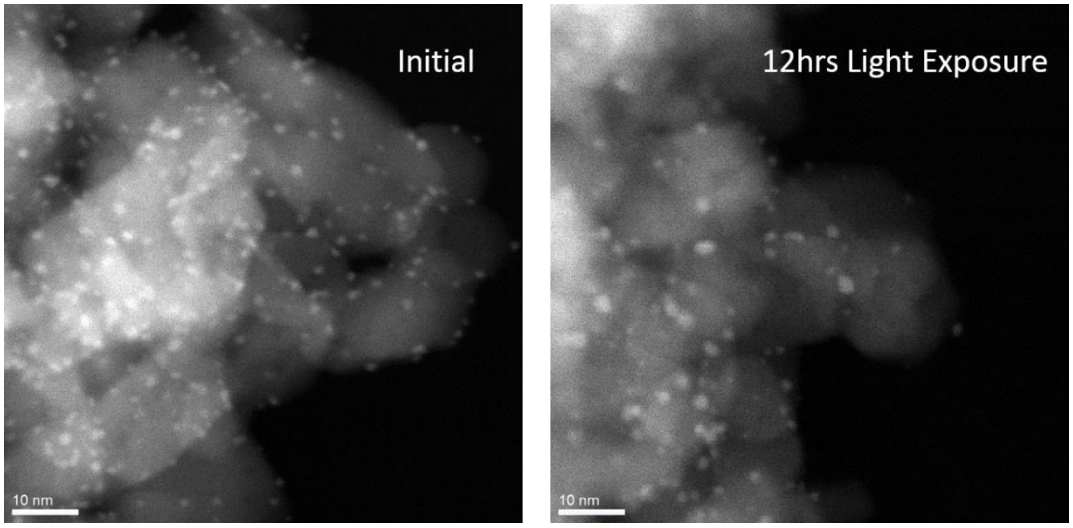

Figure 4.4 HAADF-STEM image of a) initial sample and b) after 12hrs light exposure in H_2O.

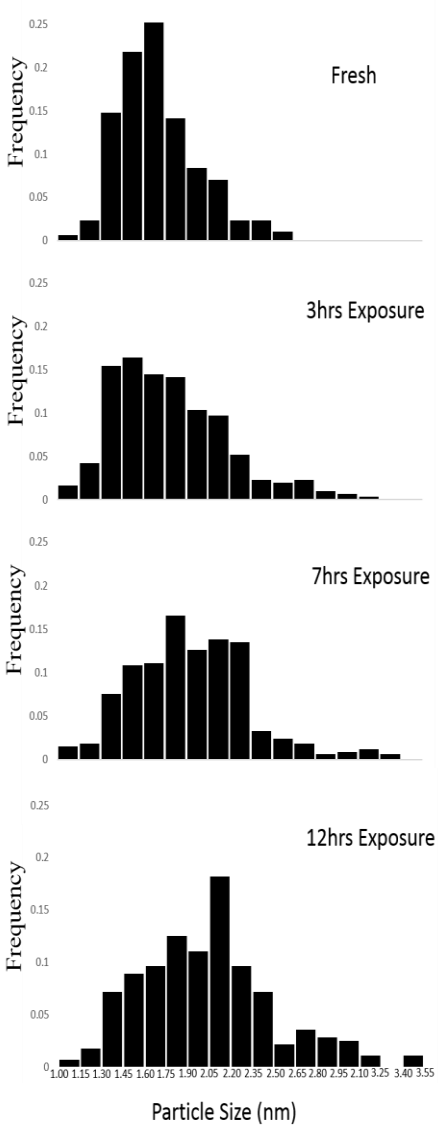

Figure 4.5. Particle distribution of samples after different lengths of time under irradiation.

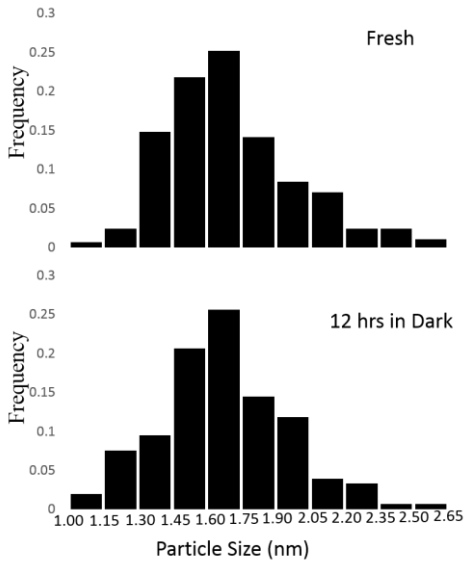

Figure 4.6. Particle size distribution of fresh sample and sample after 12hrs in H_2O in dark.

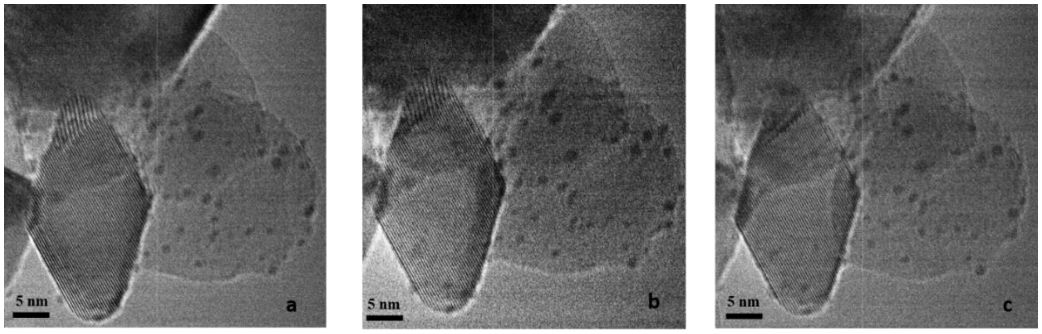

Figure 4.7. TEM images from *in-situ* experiments: a) fresh material; b) after 5hrs light exposure in 17 Torr H_2O vapor; c) after 11 hrs light exposure in 17 Torr H_2O vapor.

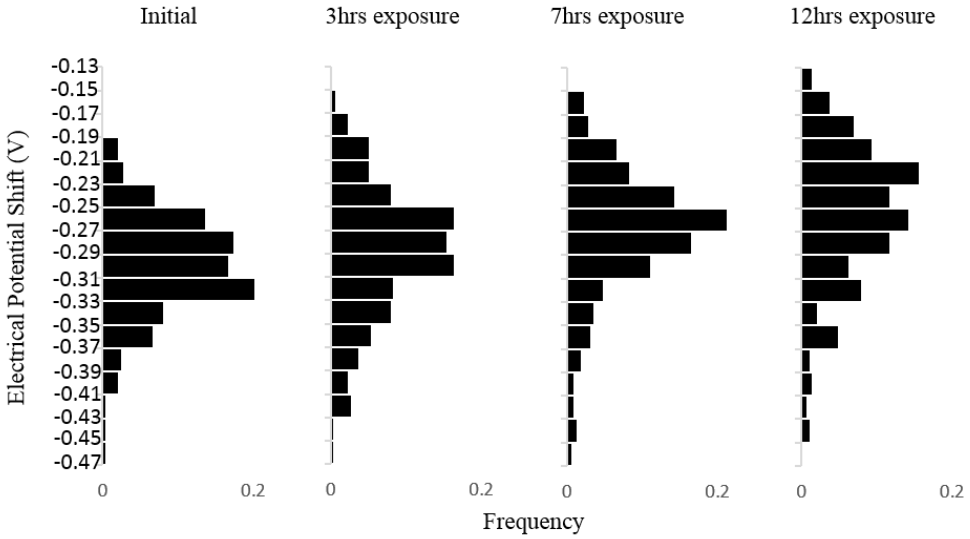

Figure 4.8. Electrical potential shift distribution of samples after different lengths of time under irradiation.

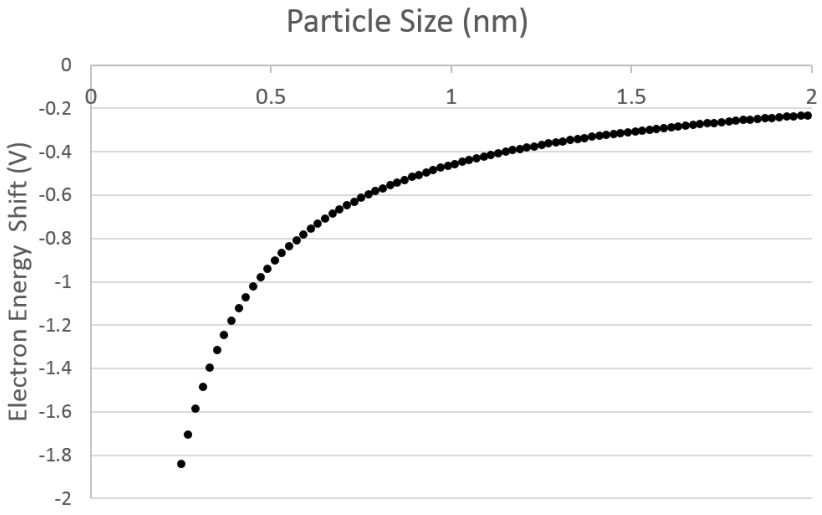

Figure 4.9. Electrical potential shift of Pt against particle size.

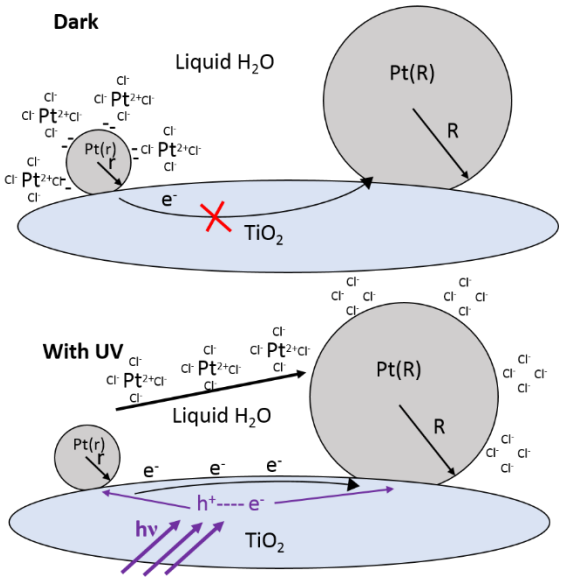

Figure 4.10. Schematic drawing of photo-electro-chemical Ostwald ripening progress.

CHAPTER 5

PHOTOCORROSION OF Ni/NiO CORE/SHELL STRUCTURES ON TiO_2 FOR WATER SPLITTING

5.1. Introduction

Following the study of structure evolution of pure TiO_2 anatase and metal/TiO_2, this chapter describes a study of structure-property relationship for TiO_2 modified with Ni/NiO core/shell co-catalyst. Simple oxide semiconductors like TiO_2 alone are poor photocatalysts for water splitting. The rate of water splitting can be increased by adding co-catalysts such as noble metals or coupled semiconductors [1-4]. Factors such as band positions, density of reactive sites, separation of electron-hole pairs and reverse reactions have critical impact on water-splitting efficiencies. Adding metal co-catalysts and coupling with other semiconductors can positively impact these factors by, for example, reducing e-h recombination and providing more reactive sites [5-10]. Among all the photocatalytic water-splitting co-catalyst systems, Ni-based co-catalysts have been extensively applied and show good photocatalytic properties [11-16]. It is also attractive because Ni is considerably less expensive than noble metals for water splitting and Ni has been extended to many different semiconductor such as oxides of Ti, Nb and Ta photocatalysts [17-19]. Ni/NiO core-shell structures have been shown to be one of the most active co-catalyst for water splitting [20]. The Ni/NiO core/shell structure has been shown to be more active than pure Ni metal, pure NiO or mixed dispersion of Ni metal and NiO nanoparticles (but not in a core/shell structure) [21, 22]. When first discovered, it was believed that the H_2 evolution site was NiO and the O_2 evolution site was $SrTiO_3$

[23]. Metallic Ni was believed to facilitate electron transfer by forming an Ohmic contact between the semiconductor and NiO, thus enhancing catalytic properties [19]. Following new experiments, this mechanism was recently revised to suggest that Ni metal is the co-catalyst for H_2 evolution and NiO is the O_2 evolution site [22].

One advantage of the core-shell structure is that it may inhibit the reverse reaction from taking place by preventing oxygen from reaching the metal surface. It has been hypothesized that it is easy for protons to diffuse through the NiO shell to reach the buried interface and the metal sites where reduction can take place. H_2 can then diffuse through the NiO multi-crystal domains shell and escape. On the other hand, NiO is well known as a good barrier for O diffusion [24, 25]. Thus, the NiO shell hinders the oxygen generated during water splitting from reacting with hydrogen on the metal surface and producing H_2O. A similar mechanism is supposedly taking place in the core/shell noble-metal/Cr_2O_3 system [26].

To date there has been few investigations of the atomic level structure of the Ni/NiO core/shell structure and its structural and compositional evolution during the water splitting processing. This structure-reactivity information can provide insight into likely mechanisms behind the functioning of the material and also provide details on the process for deactivation. There have been reports of H_2 evolution in pure aqueous water but no stoichiometric water-splitting for NiO_x on TiO_2. O_2 evolution was only observed with NaOH aqueous solutions or NaOH coated NiOx/TiO_2 pretreated materials. The H_2 evolution also decreases very quickly [19, 27]. No report has been published following the catalytic materials' structural evolution during the reaction to explain the absence of

O_2 and the drop of H_2 production. Photocorrosion is common in many non-oxide semiconductor co-catalysts which can result in rapid deactivation. For example, some sulfide semiconductors like CdS can be oxidized in photo-reactions [28, 29]. $AgCO_3$ photocatalyst undergo photo-corrosion by photo-reduction of Ag^{2+} [30]. However, no report has discussed photo-corrosion of metal co-catalysts.

Structure evolution of Ni/NiO core-shell on TiO_2 was studied with *ex situ* and *in situ* characterization in this chapter. Photocatalytic/photochemical property testing was performed under exposure to light from a xenon lamp in pure water. H_2 production was observed to drop during the reactions and no O_2 was detected. High-resolution transmission electron microscope (HRTEM) imaging was employed to investigate the structural changes taking place in the material during de-activation. A core-shell to void-shell morphological transformation was observed to take place as hydrogen evolution declined. A simultaneous increase in the Ni^{2+} ion concentration was detected in the water as the reaction proceeded, showing that photocorrosion of Ni was occurring. Analysis of the Ni ion concentration and the hydrogen evolution proves that a photochemical reaction between Ni and H_2O is primarily responsible for H_2 evolution in this case. Photo-corrosion of Ni metal and the resulting loss of Ni metal is believed to be the cause of deactivation.

5.2. Materials Preparation

Three different samples were prepared to give core-shell, NiO and mostly Ni metal particles on the TiO_2 support. NiO_x/TiO_2 was prepared with NiO 1wt% using a dry

impregnation method. The calculated volume of 0.5M $Ni(NO_3)_2 \cdot 6H_2O$ (99.999% Sigma-Aldrich) solution was dropped onto dry commercial anatase particles (99.8% Sigma-Aldrich) with continuing mixing until all the pores were saturated by solution. The mixture was dried at room temperature and calcined at 450 ℃ in air for 3 hrs. The calcined powders were then transferred into a tube furnace and reduced in flowing 5% H_2/Ar at 500 ℃ for 2 hrs followed by partial oxidation in 100 Torr O_2 for 1 hr at 200 ℃. This as-prepared material was labelled as R500-O200-TO. A second sample fully reduced in 5% H_2/Ar at 500 ℃ but not subject to the re-oxidation step was labelled as R500-TO. A third sample was fully oxidized at 500 ℃ in air and labelled as O500-TO.

For characterization of the as-prepared samples, high-resolution TEM images were taken on an aberration-corrected FEI Titan operating at 300kV and chemical analysis was performed using electron energy-loss spectroscopy (EELS) in an aberration-corrected NION microscope operating at 60kV with 0.4 eV/channel. Figure 5.1 shows TEM images of the as-prepared Ni/NiO core/shell R500-O200-TO materials. The images show clear core-shell structures. The d-spacing of the lattice fringes gained by Fast Fourier Transformation (FFT) of the high-resolution TEM images is 1.49 ± 0.02 Å at the shell which matches NiO (220), and 2.02 ± 0.02 Å at the core matching Ni (111). The FFT of the whole core-shell structure shows spots matching Ni cubic (111) and (220) and NiO cubic (111) and (200) planes. Electron energy-loss spectroscopy (EELS) line scans were performed to determine the spatially-resolved elemental composition across the interfaces between TiO_2, Ni and NiO, as well as confirming the core-shell structures as shown by Figure 5.2. A Ni L_{23} edge at 855 eV was observed from the shell to the core as expected

in Figure 5.2c. An EELS line scan showing the variation in the O K-edge intensity is also presented in Figure 5.2d. It shows an enhancement in the oxygen signal at the particle surface and is consistent with the projected O signal associated with a core-shell morphology. Interestingly, a Ti L_{23} edge was also observed on the surface of the shell (see Figure 5.2b). This is related to the strong metal-support interaction effect where in the H_2 reduction atmosphere, TiO_2 surface gets partially reduced by the proton from H_2 dissociation around Ni metal particles [31, 32]. The reduced TiO_x becomes mobile and diffuses onto the Ni metal surface and gets re-oxidized in the partial oxidation process. Apparently even after re-oxidation of Ni metal to NiO, the TiO_x remains on the outside of the NiO. The fresh R500-TO shows more rounded co-catalyst particles with fringes matching Ni metal but with a very thin NiO layer due to exposure to air.

The core-shell structured co-catalyst was uniformly dispersed among TiO_2 anatase particles with the metal particles more or less wetting the TiO_2. The length of the contact interface between the Ni metal is defined as the contact length. The metal/semiconductor contact length and the height of the particles are similar with average values of 15nm.

5.3. Photocatalytic Performance

0.2g of R500-O200-TO powders were sonicated, stirred and suspended in pure water in a self-designed photo reactor with a quartz window on top. A 450W xenon lamp (Newport) with a 350-450nm band-pass mirror was used as the light source with the light coming vertically through the top of the reactor. The incident light intensity into the reactor was calculated to be about 50mW/cm^2 from the manufacturer's manual and confirmed by a

Si-biased photo detector (THORLABS DET10A). H_2 detection was performed using a gas-chromatography (GC) (Varian 450-GC) system connected to the photoreactor with Ar as the carrier gas continuously flowing at 5 cc/ min. Reaction products in the head space above the water were sampled every 10 minutes with the GC. The same experiments were also carried out on O500-TO and R500-TO.

The photocatalytic/photochemical reactivities of R500-O200-TO, O500-TO and R500-TO are shown in Figure 5.3. Only the Ni/NiO core-shell R500-O200-TO showed detectable H_2 evolution in these experiments. The material activated relatively quickly once light was turned on with the initial H_2 being detected after 25 minutes. The maximum H_2 production rate reached about 5.5μmol/hr/g in about 100 minutes. This is partially explained by the progress H_2 reaching saturation concentration, being released to head space and then mixing fully with Ar carrier gas. After 100 minutes, the H_2 production rate started to fall as the catalyst began to deactivate with the rate dropping to about half of the initial value after 7 hrs. O_2 production was always below the detection limit in this experiment in agreement with the work of others.

5.4. Ni^{2+} concentration in H_2O during Reactions

The Ni^{2+} concentration in the water before and after the reactions were determined by inductively-coupled plasma mass spectrometry (ICP-MS) to check if the Ni metal cores dissolved into H_2O during the photoreaction. A deionized water blank and initial samples were acidified in ~0.32 M nitric acid with trace metal grade nitric acid. A series of water samples (1ml each) were taken every 30mins from the 50ml total volume solution during

the photo-reaction over a period of 4hrs after turning on the light. The water samples were diluted five-fold to keep them within the instrument's calibration range. Samples were analyzed by quadrupole ICP-MS (ThermoFisher Scientific iCAP Q, with CCT option). Ni and Ti were run in CCT-KED ("Collision Cell Technology-Kinetic Energy Discrimination") mode with high purity He as the collision cell gas. Samples were measured at isotopes ^{58}Ni, ^{60}Ni and ^{62}Ni, ^{47}Ti, ^{48}Ti and ^{49}Ti, respectively to monitor for interferences, but only data from ^{60}Ni measurements are reported here. This isotope had the lowest detection limit and gave the most reliable and accurate Ni determination. The initial pH of the solution was 7 rising to 7.5 after the photo reaction.

Figure 5.4 shows a steady rise of Ni^{2+} detected by ICP-MS in water and H_2 production detected by GC as a function of time during the reaction. Material which was suspended in the DI water, sonicated for 10mins and stirred for 20mins without the light exposure was used as the initial sample. The concentration of Ni^{2+} in this initial sample was below the detection limit. This shows that there was negligible loss of Ni without light indicating that the change is Ni photo-corrosion. The amount of Ni released into solution was compared with the total amount of H_2 produced. The amount of Ni in solution almost matched the H_2 production.

5.5. Structure Evolution during Reactions and Photocorrosion.

To study the mechanism for the deactivation and build a structure-reactivity relationship, another experiment was carried out under similar conditions. The H_2 production experiment was repeated without the reactor connected to gas chromatography. The

reactor was opened 3 times after 80mins, 120mins and 180mins of photo-reaction, suspensions of materials were taken from the reactor and dropped onto TEM grids to make a TEM sample. TEM images were taken in order to determine the structural evolution during activation/de-activation.

Figure 5.5a and 5.5b show two examples of the significant morphological changes that were observed in the core-shell material when close to 50% deactivation. Figure 5.5a shows that Ni metal has completely vanished from the center of the particle and that a void remains between the TiO_2 and NiO shell. Figure 5.5b shows a partial void formed at the interface of the Ni metal and TiO_2. In a partial void, some of the Ni metal remains but the contact area between the metal and the TiO_2 semiconductor is reduced. The percentages of complete void and partial void structures were measured based on over 30 different areas of each sample after 80 min, 120 min and 180 min of the reaction. The results are given in Table 5.1. The percentage of partial voids increased at the beginning and then decreased with longer exposure in water. The number of complete voids increased with light exposure time and reached 41% of the total areas checked after 180 mins. This indicates that the partial void structures are early stages of complete void-shell structures. From the TEM images, the void first forms at the interfaces of Ni metal and TiO_2 and then expands to replace the whole metal particle. Charge transfers from the TiO_2 to Ni metal will be impeded by the voids formed at the interface of Ni metal and TiO_2 semiconductors negatively impacting hydrogen production. The loss of contact between the Ni metal and TiO_2 is believed to be one reason for deactivation. Morphology was also checked for materials stirred for 4hrs without light exposure. No significant

voiding was observed which proves that the core-shell to void-shell conversion is a photo-induced change.

For the materials used in the reactions, 27 μmol of Ni was present on the TiO_2 in the form of both the NiO shell and Ni metal core. Based on the TEM image, the volume ratio of NiO and Ni is close to 1.5:1 and the density of NiO to Ni is about 0.75:1. So the ratio of Ni in NiO and in Ni metal is 1.15. That means there is 13 μmol of Ni metal in the material. According to the TEM observations, 41% of the 13 μmol (5.3 μmol) has been converted to Ni^{2+}. According to ICP, the amount of Ni^{2+} in solution after 180 mins reaction is 4 μmol. Thus, the TEM and ICP results are in reasonable agreement. . TEM images were also taken on R500-TO and O500-TO before and after 4hrs Xenon lamp irradiation in liquid water as shown in Figure 5.6. Figure 5.6a and 5.6b show rounded Ni metal particles on TiO_2 and the morphology is maintained after irradiation. NiO particles look more faceted and are more irregular in shape. The NiO morphology is unchanged before and after irradiation. HRTEM confirmed the particles are still Ni metal and NiO after irradiation for R500-TO and O500-TO respectively. The fact they do not show a structural change is consistent with the absence of photo-reaction activity.

Ni metal on R500-TO does not show the coarsening phenomenon observed on Pt/TiO_2 samples. The main reason for this could be because the average size of these Ni particles is about 20nm with which the electrode potential shift due to the Gibbs-Thompson effect is very small. There is not as much potential difference between the small and large Ni particles. Secondly, Ni metal after full reduction is easily to be

oxidized and forms thin NiO layers when exposed to air. The NiO layer protects Ni from dissolving into H_2O.

5.6. Mechanism

The microscopy, catalytic and ICP measurements suggest a possible mechanism for the photocorrosion of Ni. Hydroxyl radicals OH ·are known as major reactive species in photo reactions [33-35]. The standard reduction potential $E(Ni^{2+}/Ni)$ is -0.257V and $E(OH\cdot/OH^-)$ is 2.02V. So the Ni will be easily oxidized by OH · to Ni^{2+} [36]. This is consistent with the results from ICP-MS. A possible reaction pathway for the mechanism is:

$$TiO_2+h\nu \rightarrow TiO_2+e^-+h^+$$

$$2H^++2e^- \rightarrow H_2$$

$$H_2O+h^+ \rightarrow OH\cdot+H^+$$

$$2H^++Ni+2OH\cdot \rightarrow Ni^{2+}+2H_2O$$

This mechanism shows why the concentrations of Ni^{2+} and H_2 match. It also explains the absence of O_2 because most of the light-induced holes are used to oxidize the Ni to Ni^{2+} via the OH radical reaction. As shown in Figure 5.7 a, the OH ·radicals relevant to the Ni photocorrosion are produced from the holes accumulated in the NiO shell. These OH · radicals are produced in the vicinity of the Ni metal core. The much slower photocorrosion on the pure Ni sample highlights the importance of locally generated radicals. Those results also reflect the fact that Ni/NiO core/shell structures are critical to

catalyze the photoreactions. The observation and reaction mechanism show that H_2 is produced by a photochemical reaction. This reaction is not catalytic with respect to the Ni because Ni is consumed during the reaction.

There are two possible pathways Ni metal could be contacted by OH ·radicals and get oxidized and dissolved into the H_2O. One way is that OH ·radicals enter through cracks on NiO shell. The other one is that Ni diffuse through the NiO in a Kirkendall effect. Both of these two pathways are depicted in Figure 5.7 b.

5.6.1 Photocorrosion through Cracks on NiO Shell.

The examination about the partial void structures which is the early stage of the structural change suggests that the voids mostly nucleate at Ni, NiO and TiO_2 triple points. Analysis of the morphological evolution indicates that core-shell structure conversion to void-shell structure is more likely on particles having large height/length ratio and high contact angles, i.e. particles which are more weakly bonded to the TiO_2. It is possible that cracks or openings may occur at these weakly bonded interfaces which allow water to directly contact Ni metal facilitating the Ni oxidation reactions. However, among the many images recorded, not many obvious cracks can be directly observed.

To confirm or even locate the existence of cracks on NiO shells, it is critical to find an etchant solution which only etches the Ni core but does not react with the NiO. Then if similar void/shell structures were observed after submersing the materials in this etchant in the dark, that shows proof there are cracks on NiO shells allowing the contact of the Ni metal core to the etchant solution. Otherwise, the NiO shell should protect the

Ni core from being etched away. We have carried out experiments looking for a best recipe of etchant which would dissolve Ni wires but not Ni wires with a condensed NiO layer formed when heated to high temperature in air. After repeated experiments, a suitable recipe of 0.07M H_2O_2 + 0.07M HCl was found to be able to etch away a 0.12g Ni wire within 24 hrs while not change the weight of the same amount of Ni with a NiO layer developed at 700 ℃ for 1hr in air. The R500-O200-TO materials were submersed in this etchant for 15mins in dark and then checked under TEM. Figure 5.8 shows the void/shell structures similar to what have been observed during photo-reactions. This serves as evidence of cracks on NiO shells through which etchant can reach Ni metal core. However, there is still a significant amount of Ni/NiO core/shell structure maintained due to good protection from NiO shells which have less cracks.

5.6.2 Photocorrosion through Ni Diffusion.

The void/shell structures look similar to the morphology we observed during thermal treatment of Ni metal on silica at 400 ℃ in oxidative atmosphere [37]. Ni metal diffuses several orders of magnitude faster than O along the NiO grain boundaries at elevated temperatures [38].That results in a Kirkendall effect where Ni diffuses from the core through the NiO shell resulting in vacancy formation on the Ni metal which then coalesce and form voids. For this photoreaction, based on measurements of the thickness and outer diameter of NiO layers as a function of time, no change of the thickness of the NiO shell was observed in this case. If there is Ni diffusion through NiO, the Ni metal atoms are oxidized outside the NiO shell dissolved into H_2O.

However, the thermal diffusion rates of Ni and O through NiO are both very low at room temperature under which the photoreactions were performed. One possible explanation is that the light absorbed in the Ni particle results in local heating which can drive the Ni diffusion process. The temperature rises $\Delta T = \frac{I*A}{C\rho v}$., where I is the flux of the UV light 50mW/cm^2; A is the cross area of a Ni particle; C is the thermal capacity of Ni (0.44J/g ℃), ρ is the density of Ni and v is the volume of the particle. Taking a radius of 10nm particle, the absorption of light can result in a theoretical local temperature rise of ~10^3 K/s in an isolated Ni particle. However, all this excess heat is rapidly conducted away. The distance it requires to drop from 1000 K to 30 K is calculated to be: $d = \frac{I*A}{\sigma*970}$ where σ is the thermal conductivity for Ni 90.9Wm^{-1}K^{-1}. d is calculated to be ~ 10^{-18}m which is negligible small. Thus most of the local heat will be conducted very fast without resulting a local heat. Accordingly, it is preferable to believe that the OH ·radicals enter through the cracks on NiO shells and oxidize the Ni to Ni^{2+}.

5.7. Summary

Ni/NiO core/shell on TiO_2 was prepared and tested for photocatalytic/photochemical reactivity. H_2 evolution was detected but no O_2 was produced. The H_2 production rate gradually dropped because the core-shell structures transformed to hollow NiO shells. The loss of Ni metal from the core was believed to be the primary reason of deactivation. ICP-MS was utilized to determine Ni^{2+} concentration in the solution before and after reactions An increase of Ni^{2+} in the water was detected and matched the amount of H_2 produced. Thus, the void formation was the result of Ni oxidation and dissolution during

light illumination. This photocorrosion is now believed to occur due to Ni oxidized by OH ·radicals from direct contact with the water through cracks. Although the core/shell structure of Ni/NiO was effective in decreasing the back reaction and raising the H_2 production rate, it was not able to protect the Ni metal core from photocorrosion. The H_2 evolution was generated by a photochemical reaction which involved photocorrosion of Ni metal. To design a better photocatalyst with this core/shell structure, a layer resistant to both O diffusion and the metal diffusion should be considered.

References

1. Yamaguti, K., & S. Sato, S. (1985). Photolysis of water over metallized powdered titanium dioxide. *Journal of Chemical Society, Faraday Transactions 1,* 81, 1237-1246.

2. Sayama, K., & Arakawa, H. (1997). Effect of carbonate salt addition on the photocatalytic decomposition of liquid water over Pt–TiO_2 catalyst. *Journal of Chemical Society, Faraday Transanctions,* 93, 1647-1654.

3. Tabata, S., Nishida, H., Masaki Y. & Tabata, K. (1995). Stoichiometric photocatalytic decomposition of pure water in Pt/TiO_2 aqueous suspension system, *Catalysis Letters,* 34, 245–249.

4. Kudo A. & Kato. H. (2000). Effect of lanthanide-doping into $NaTaO_3$ photocatalysts for efficient water splitting. *Chemical Physics Letter,* 331 (5-6), 373-377.

5. John, M. R., Furgals, A. J. & Sammells. A. F. (1983). Hydrogen generation by photocatalytic oxidation of glucose by platinized n-TiO_2 powder. *Jounal of Physical Chemistry*, 87, 801-805.

6. Subramanian, V., Wolf, E. & Kamat, P. (2001). Semiconductor-metal composite nanostructures, to what extent do metal nanoparticles improve the photocatalytic activity of TiO_2 films? *Jounal of Physical Chemistry B,* 105, 11439-11446.

7. Jakob, M., Levanon, H., & Kamat, P.V. (2003). Charge distribution between UV-irradiated TiO_2 and gold nanoparticles: determination of shift in the fermi level. *Nano Letters*, 3(3), 353-358

8. Gurunathan, K., Maruthamuthu, P. & Sastri, V.C. (1997). Photocatalytic hydrogen production by dye-sensitized Pt/SnO_2 and Pt/SnO_2/RuO_2 in aqueous methyl viologen solution. *International Journal of Hydrogen Energy*, 22(1), 57-62.

9. Keller, V. & Garin, F. (2003). Photocatalytic behavior of a new composite ternary system: WO_3=SiC-TiO_2. effect of the coupling of semiconductors and oxides in photocatalytic oxidation of methylethylketone in the gas phase. *Catalysis Communications,* 4, 377-383.

10. Kang, M. G., Han, H. E., & Kim, K.J. (1999). Enhanced photodecomposition of 4-chlorophenol in aqueous solution by deposition of CdS on TiO_2. *Journal of Photochemical Photobiology A: Chemstry*, 125, 119-125

11. Wang, W., .Liu, S., Nie, L., Cheng, B. & Yu, J., (2013). Enhanced photocatalytic H_2-production activity of TiO_2 using $Ni(NO_3)_2$ as an additive. *Physcial Chemistry Chemical Physics*, 15, 12033-12039

12. Yu, J.; Hai, Y. & Cheng, B. (2011). Enhanced Photocatalytic H_2-Production Activity of TiO_2 by $Ni(OH)_2$ Cluster Modification. *Journal of Physical Chemistry C*, 115, 4953–4958.

13. Chen, S., Chen, X., Jiang, Q., Yuan, J., Lin, C. & Shangguan W. (2014). Promotion effect of nickel loaded on CdS for photocatalytic H2production in lactic acid solution. *Applied Surface Science*, 316, 590-594.

14. Lin J., Yana, S., Huang, Q., Fan, M., Yuan, Y., Tan T. & Liao, D. (2014). TiO_2 promoted by two different non-noble metal co-catalysts for enhanced photocatalytic H_2 evolution. *Applied Surface Science*, 309, 188-193.

15. Cui, E. & Lu, G. (2014). Enhanced surface electron transfer by fabricating a core/shell Ni@NiO cluster on TiO_2 and its role on high efficient hydrogen generation under visible light irradiation. *International Journal of Hydrogen Energy*, 39, 8959-8968.

16. Sreethawong, T., Suzuki, Y. & Yoshikawa, S. (2005). Photocatalytic evolution of hydrogen over mesoporous TiO_2 supported NiO photocatalyst prepared by single-step sol–gel process with surfactant template. *International Journal of Hydrogen Energy*, 30, 1053-1062.

17. Kim, J., Hwang, D. W., Kim, H. G., Bae, S. W., Lee, J. S., Li W. & Oh. S. H. (2005). Highly efficient overall water splitting through optimization of preparation and operation conditions of layered perovskite photocatalysts**.** *Topics Catalysis,* 35, 295-303.

18. Domen, K., Kudo, A., Shinozaki, A., Tanaka, A., Maruya, K., & Onishi, T. (1986) Photodecomposition of water and hydrogen evolution from aqueous methanol solution over novel niobate photocatalysts. *Journal of Chemical Society, Chemical Communication*s, 356-357

19. Kudo, A.; Domen, K.; Maruya, K.; Onishi, T. (1987), Photocatalytic Activities of TiO_2 Loaded with NiO. *Chemical Physics Letters*, 133, 517-519.

20. Kudo, A. & Miseki, Y. (2009). Heterogeneous photocatalyst materials for water splitting. *Chemical Society Review*, 38, 253–278

21. Domen, K., Kudo, A. & Onishi, T. (1986). Mechanism of photocatalytic decomposition of water into H_2 and O_2 over $NiOx/SrTiO_3$. *Journal of Catalysis.* 102, 92–98.

22. Townsend, T. K., Browning N. D. & Osterloh. F. E. (2012). Overall photocatalytic water splitting with NiO_x–$SrTiO_3$ – a revised mechanism. *Energy & Environmental Science*, 5, 9543-9550

23. Domen, K., Naito, S., Onishi, T. & Tamaru, K. (1982) Study of the photocatalytic decomposition of water vapor over a nickel(II) oxide-strontium titanate ($SrTiO_3$) catalyst. *Journal of Physical Chemistry*, 86, 3657–3661.

24. Matsumotoa, Y., Unala, U., Tanakaa, N., Kudob, A. & Kato, H. (2004) Electrochemical approach to evaluate the mechanism of photocatalytic water splitting on oxide photocatalysts. *Journal of Solid State Chemistry*, 177, 4205–4212

25. Hansen, K. K. (2008). Electrochemical reduction of O_2 and NO on Ni, Pt and Au. *Journal of Appled Electrochemistry*, 38, 591–595.

26. Yoshida, M., Takanabe, K., Maeda, K., Ishikawa, A., Kubota, J., Sakata, Y., Ikezawa, Y. & Domen, K. (2009). Role and function of noble-metal/Cr-layer core/shell structure cocatalysts for photocatalytic overall water splitting studied by model electrodes. *Journal of Physical Chemistry C*, 113, 10151–10157.

27. Kiwi, J. & Griltzel, M. (1984). Optimization of conditions for photochemical water cleavage. Aqueous platinum/TiO_2 (anatase) dispersions under ultraviolet light. *Journal of Physical Chemistry*, 88, 1302-1307

28. Meissner, D., Benndorf, C. & Memming R. (1987). Photocorrosion of cadmium sulfide: Analysis by photoelectron spectroscopy. *Applied Surface Science*. 27, 423-436

29. Ferm ń, D.J., Ponomarev E.A. & Peter, L.M. (1999). A kinetic study of CdS photocorrosion by intensity modulated photocurrent and photoelectrochemical impedance spectroscopy. *Journal of Electroanalytical Chemistr*, 473, 192–203

30. Dai, G., Yu, J. & Liu, G. (2012). A new approach for photocorrosion inhibition of Ag_2CO_3 photocatalyst with highly visible-light-responsive reactivity. *Journal of Physical Chemistry C*, 116, 15519−15524

31. Tauster, S. J., (1987). Strong metal-support interactions. *Accounts of Chemical Research*, 20(11), 389-394.

32. Sharma, V., Crozier, P. A., Sharma, R. & Adams， J. B. (2012). Direct observation of hydrogen spillover in Ni-loaded Pr-doped ceria. *Catalysis Today*, 180(1), 2-8.

33. Ishibashi, K., Fujishima, A., Watanabe, T. & Hashimoto, K., (2011), Detection of active oxidative species in TiO_2 photocatalysis using the fluorescence technique. *Electrochemitry Communications*, 47, 6906–6908.

34. Xiao, Q., Si, Z., Zhang, J., Xiao, C. & Tan, X. (2008), Photoinduced hydroxyl radical and photocatalytic activity of samarium-doped TiO_2 nanocrystalline. *Journal of Hazardous Materials*, 150, 62-67.

35. Xiang, Q., Yu, J., Wang, W. & Jaroniec, M. (2011). Nitrogen self-doped nanosized TiO_2 sheets with exposed {001} facets for enhanced visible-light photocatalytic activity. *Chemical Communications*, 47, 6906-6908.

36. Van ýsek, P. (2011). Electrochemical Series. Handbook of Chemistry and Physics: 92nd Edition

37. Chenna, S. & Crozier, P.A. (2012). In situ environmental transmission electron microscopy to determine transformation pathways in supported Ni nanoparticles. *Micron*, 43, 1188-1194

38. Peraldi, R., Monceau, D. & Pieraggi, B. (2002). Correlations between growth kinetics and microstructure for scales formed by high-temperature oxidation of pure nickel. II. growth kinetics. *Oxidation of Metals*, 58,275-295

Time of Reaction in liquid water under light	% of partially voids	% of fully voids
Initial	0%	0%
80mins	7%	5%
120mins	2%	11%
180mins	2%	41%

Table 5.1. Percentage of void/shell areas during deactivation of materials.

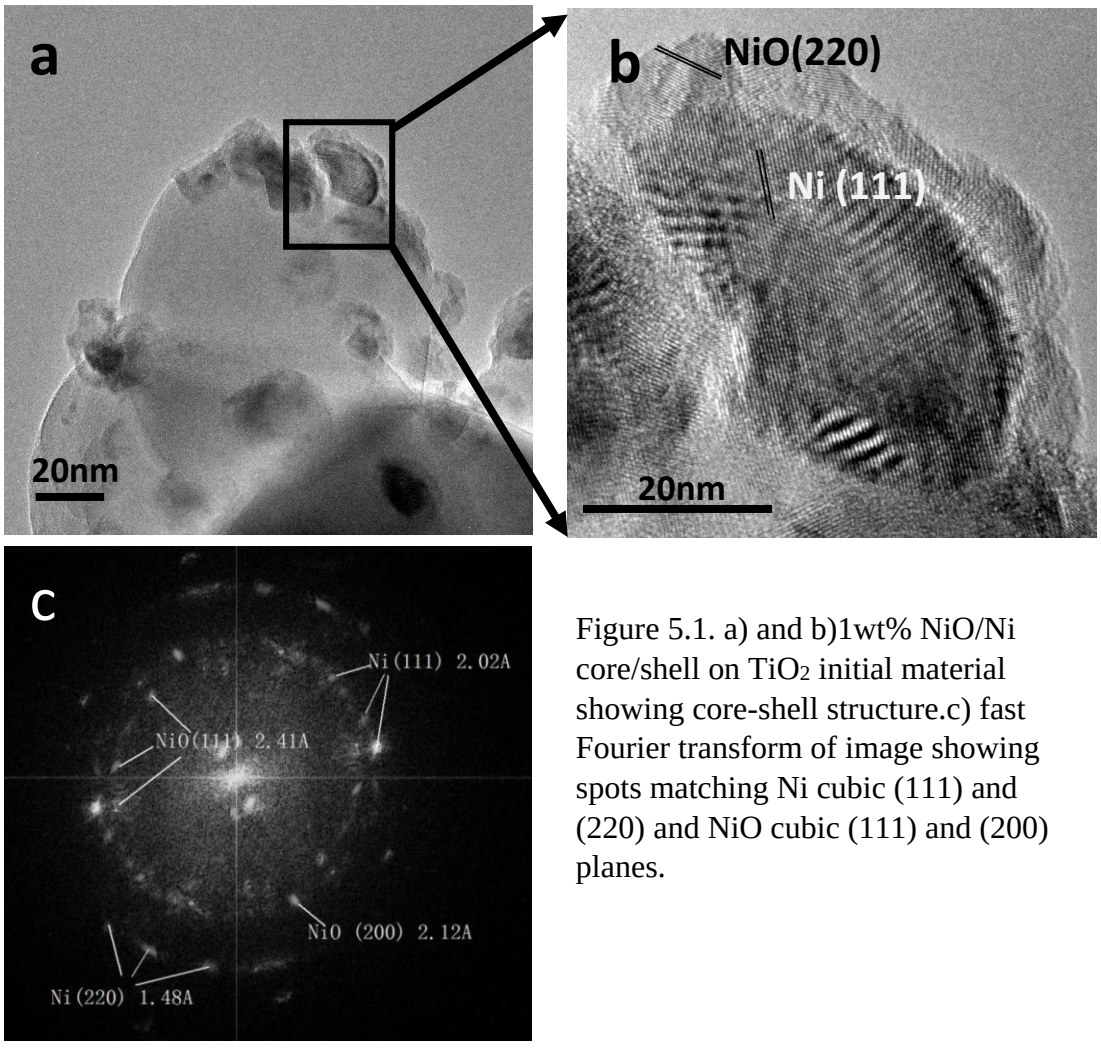

Figure 5.1. a) and b)1wt% NiO/Ni core/shell on TiO_2 initial material showing core-shell structure.c) fast Fourier transform of image showing spots matching Ni cubic (111) and (220) and NiO cubic (111) and (200) planes.

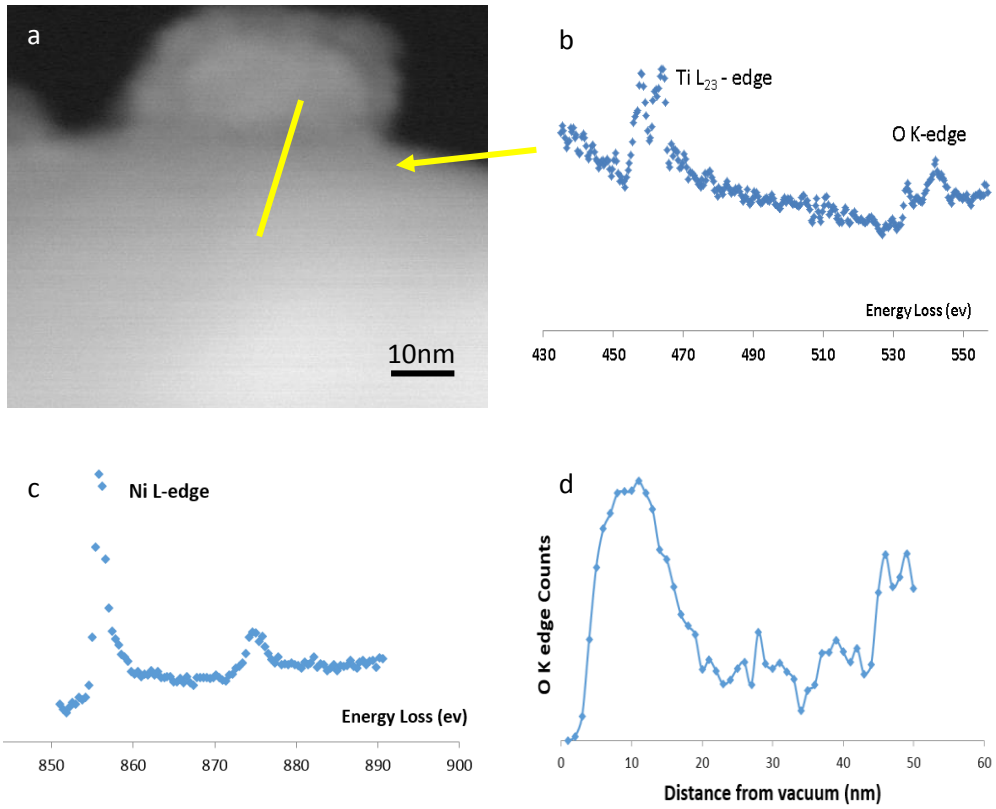

Figure 5.2. a) STEM Image of Ni/NiO core/shell structure on TiO_2; b) Ti L-edge peaks at the shell position; c) EELS Ni L-edge; d) O K-edge intensity as a function of position along line scan. The left side is interface with the vacuum and the right side in the interface with TiO_2.

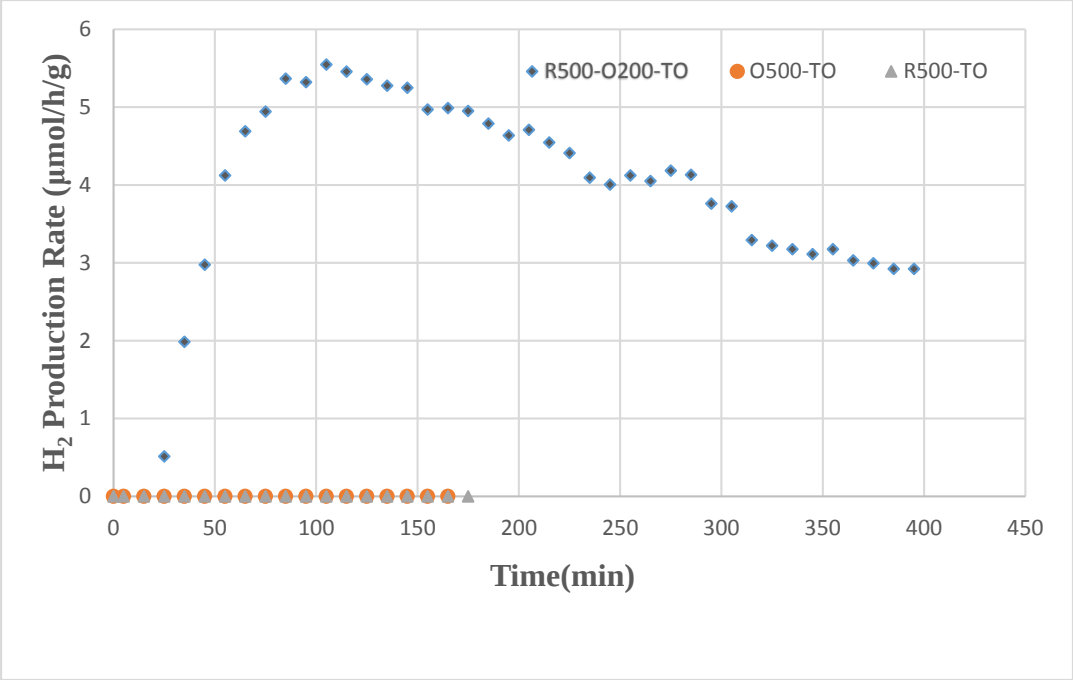

Figure 5.3. H_2 production rate versus time for three different materials. Ni and NiO overlap with zero H_2 production.

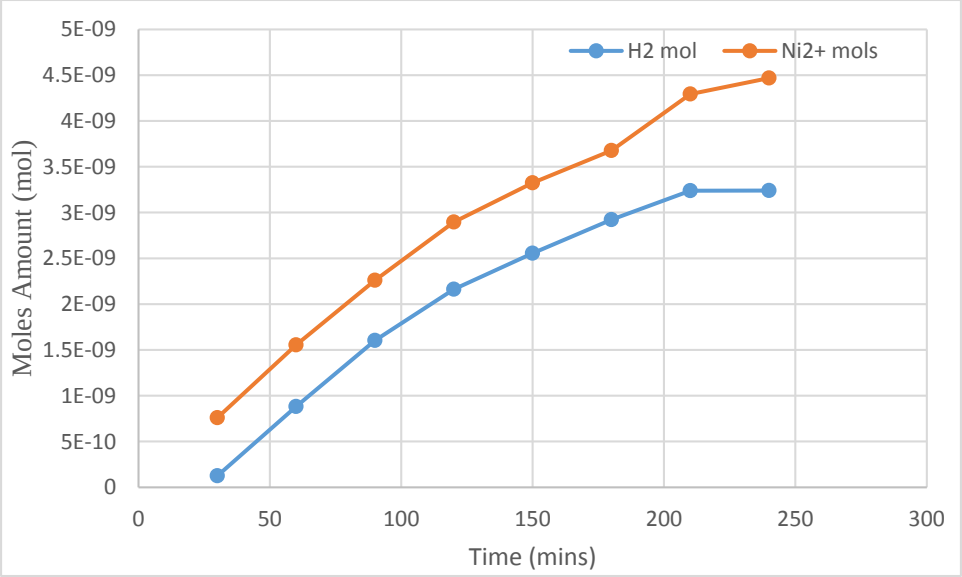

Figure 5.4. Plot of amounts of Ni^{2+} in 50ml water and H_2 producted during reaction

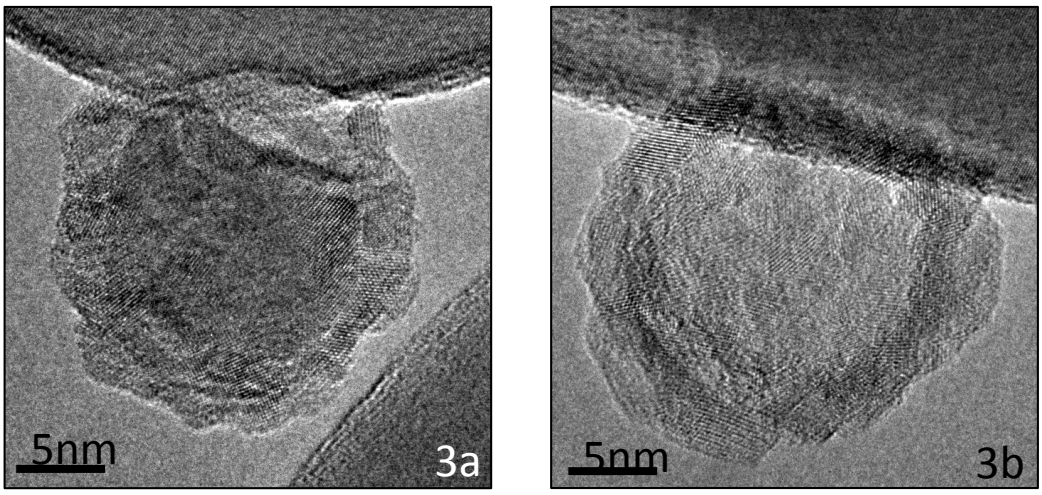

Figure 5.5. a). Partial void-shell structure areas of deactivated materials show cleavages in between TiO_2 and Ni metal b). Void/shell structures after 50% deactivation

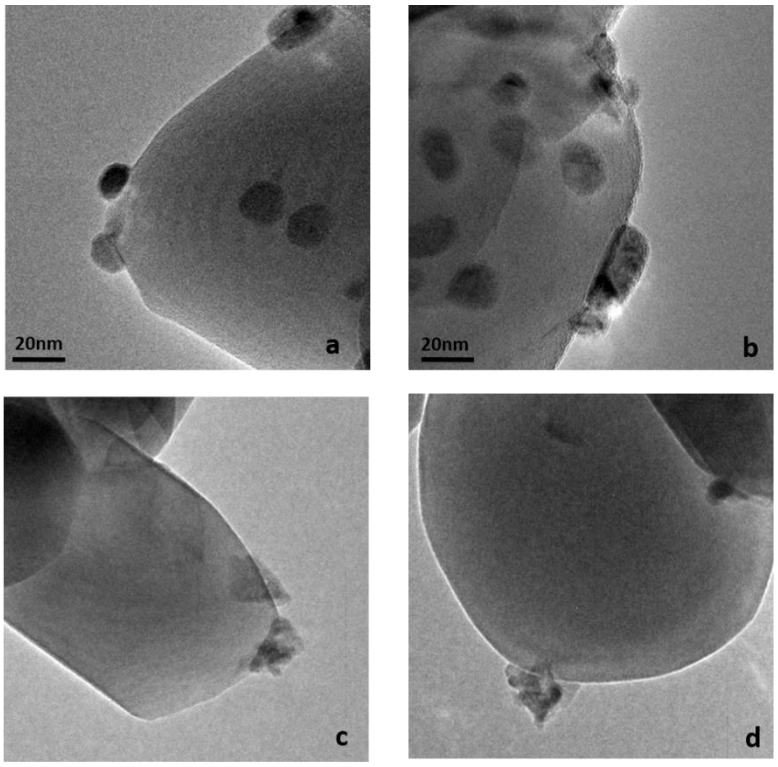

Figure 5.6. TEM images of R500-TO and O500-TO before and after light irradiation in water: a) initial R500-TO; b) R500-TO after 4 hrs light irradiation in liquid water; c) initial O500-TO; d) O500-TO after 4hrs light irradiation in liquid water.

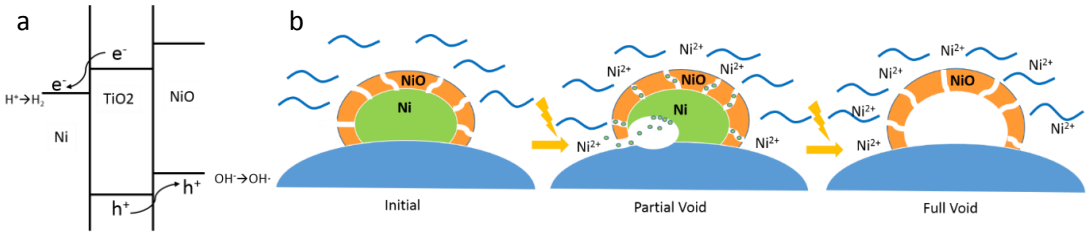

Figure 5.7. Schematic drawing of a) band diagrams, b) the mechanism for core-shell to void-shell conversion.

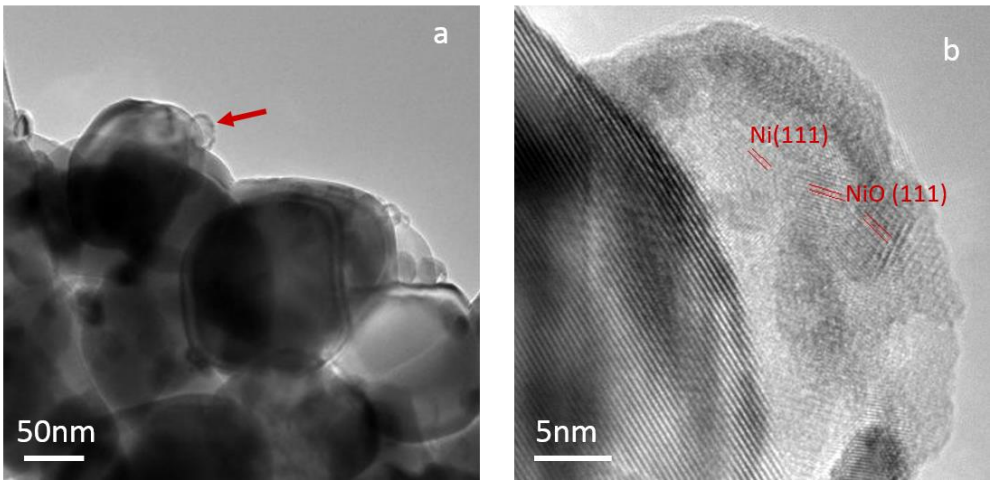

Figure 5.8. (a) Morphology of R500-O200-TO photocatalyst after 15mins submersed in etchant (b) zoom in of one of the core/shell structure generated from etching.

CHAPTER 6

SUMMARY AND FUTURE WORK

6.1. Summary

This thesis has summarized extensive nanoscale research on typical types of photocatalyst nanomaterials of their structure evolution during water splitting using TEM. The photocatalysts being studied included pure TiO_2 anatase, Pt onTiO_2 and Ni/NiO core/shell structures on TiO_2. Those materials serve as important examples of photocatalysts of oxide semiconductor, metal on semiconductor and more complicated metal/semiconductor on semiconductor photocatalysts. With the help of TEM, this research has provided structural and chemical information to the nanoscale level corresponding to high-surface-area nanomaterials, especially under water-splitting reaction conditions For example, oxide semiconductors like TiO_2 and noble metal co-catatalyst like Pt are well known as stable catalysts under reaction conditions. For the first time in this thesis, it is revealed that these materials are not so stable at the nanoscale. They have gone surface phase change or coarsening which affect the photocatalytic properties. Photo-corrosion was also observed on Ni/NiO core/shell on TiO_2. These structural evolutions explained the corresponding de-activation of photocatalytic properties. Structure changes observed are summarized by:

Photo-induced Surface Amorphization of Pure Anatase TiO_2

Well-defined anatase TiO_2 with rhombohedral or rod shapes terminated mostly by (101) and (001) facets were prepared using hydrothermal method. The nanoparticles were characterized in the environmental TEM exposed to 10 suns light intensity and 1 Torr

H_2O vapor. 1 to 2 surface monolayers of ordered TiO_2 were observed to change to disordering on particles exposed to hours of light and H_2O. Reduced Ti states accompanied with oxygen vacancies were found using XPS and EELS on the TiO_2 surfaces. The surface amorphization is believed to be related to the surface hydroxyl groups formed at the surface oxygen vacancies during the water-splitting reactions. The thickness of amorphization layers does not increase with longer exposure time. This suggests the density of surface hydroxyl groups reach to an equilibrium state in which the adsorption/desorption of dissociated H_2O is the same, and the dissociated H_2O will not penetrate the amorphous surface monolayers. In this sense, the TiO_2 materials are considered stable without the collapse of the bulk materials.

Photo-induced Ostwald Ripening of Pt Nanoparticle Co-catalyst on TiO_2

Pt is a very common noble metal co-catalyst for many different catalysis reactions. When it is used as photocatalyst, it helps to separate e-h pairs and lower the barrier for proton absorption and H_2 desorption. A drop of H_2 production rate to 1/3 after 9 hrs was observed when using 2%wt Pt on TiO_2 doing water splitting in DI water. Photo-induced coarsening of Pt nanoparticles was discovered by comparing their particle sizes in the ADF-STEM images taken from samples during different reaction periods. The average particle size grows from 1.69 ± 0.05nm to 2.06 ± 0.09nm. The deactivation is partially because of the surface area decrease and also the less overpotential for electron transfer from larger size Pt particles to the reactants. According to Gibbs-Thompson effect, the electrical potential is shifted to more negative potential when the particle size is smaller. Smaller Pt particles with more negative electrode potential are more likely to be oxidized

compared to larger particles. When exposed to light, small Pt particles are connected to larger Pt particles through more conductive TiO_2 as cathode and anode. Pt gets oxidized from small particles, dissolved into H_2O and redeposited on larger particles. Electrons are transferred from small Pt particles to larger ones in the mean time.The oxidation and reduction of Pt cannot happen in dark when TiO_2 is highly insulating. This photo-induced coarsening may also apply on other metal co-catalyst such as Ag (see Appendix) and result in some degradation of the catalytic activities.

Photo-induced Corrosion of Ni Metal on Ni/NiO Core/shell Co-catalyst on TiO_2

The Ni/NiO core shell structure co-catalyst is an important system which has been applied to many semiconductor photocatalyst and show good activities. It is beneficial for e-h separation and for inhibiting the H_2 and O_2 back-reaction. When coupled with TiO_2 and tested for H_2 production in DI water, a deactivation was observed during reactions with the H_2 production rate, dropping to half of the highest value after 7 hrs irradiation. Samples were prepared and characterized in TEM after different time periods during the water-splitting reaction. An increase of void/shell structures in which the Ni was etched away was observed as the reaction proceeded. Experiments in which the material was exposed to light and water vapor during *in situ* TEM characterizations showed no void/shell structures. This suggested that the Ni metal was oxidized to Ni^{2+} and dissolved into water. An increase of the number of Ni^{2+} ions in solution was detected by ICP-MS which matches the number of H_2 molecules produced. This proves the reduction half-reaction of H_2 production happened with the Ni metal oxidation as the other half-reaction rather than O_2 production. The Ni metal is believed to be oxidized by the OH ·radicals

generated by OH^- taking photo excited holes from the photocatalyst. The OH ·radicals in H_2O may have reached the Ni metal cores through cracks in the NiO shells. This was confirmed using a H_2O_2+HCl water solution which only etched Ni but not NiO. Similar void/shell structures were observed for samples submersed in this etchant in dark proving the existence of cracks on NiO shells allowing the contact of the oxidative etchant and the Ni core. A better protection layer has to be prepared for this system to overcome Ni being etched by the oxidative species.

6.2 Future Work

6.2.1 *In situ* Characterization of Liquid-phase Water Splitting Using Graphene Film Liquid Cells.

Several examples have been shown in which significant structure changes happen in liquid-phase water with the solid metal dissolved into H_2O in forms of ions. *In situ* TEM characterizations was carried out in vapor-phase H_2O. Same structural changes for Pt/TiO2 and Ni/NiO on TiO_2 in *ex situ* experiments in liquid phase H_2O were not observed. To better study the mechanisms, it is critical to observe the structure evolution happening *in situ* in liquid-phase H_2O atmosphere. A convenient cell with thin liquid layers allowing high resolution is required. Liquid cells on TEM grids can be prepared by enclosing liquid between two graphene films as shown in Figure 6.1 [1]. Free-floating graphene films were prepared by etching away the Cu substrates. Another graphene film deposited on TEM grids with nanoparticle/H_2O suspension on top was attached to the free-floating graphene film. The two films stick together by van de Waals forces. Liquid can thus be trapped in small pockets between two graphene films. Liquid cells with

suspensions of photocatalyst nanomaterials in water have been prepared following this procedure. Some preliminary results are shown in Appendix V.

6.2.2 Detection of Local Band-gap and Surface States on Photocatalyst Nanoparticles Using Monochromated EELS.

To perform bandgap engineering on photocatalysts for water splitting especially for visible light responsive water splitting, it is important to know the local band gap and interstates of the nanomaterials. With the recent achievements of monochromated STEM EELS, an ultra-high energy resolution of 15meV or better can be obtained in low-loss region [2]. Local band-gap changes at the interface can be determined by scanning the focused beam across the interface. Information about the band-gap and inter-band states at the surfaces are critical for photocatalytic reactions. They can be obtained using the ALOOF beam technique where the electron beam is parked several nm away from the surfaces of the sample when EELS is acquired. This technique tremendously minimizes the beam damage to the material. Some preliminary results are shown in Appendix VII.

References:

1. Yuk, J.M., Park, J., Ercius, P., Kim, K., Hellebusch, D.J., Crommie, M.F., Lee, J.Y., Zettl, A.& Alivisatos, A.P. (2012), High-Resolution EM of colloidal nanocrystal growth using graphene liquid cells, *Science*,336(6077), 61-64.

2. Krivanek, O. L., Lovejoy, T. C., Dellby, N., Aoki, T., Carpenter, R. W., Rez, P., Soignard, E., Zhu, J., Batson, P. E., Lagos, M. J., Egerton R. F. & Crozier P. A. (2014). Vibrational spectroscopy in the electron microscope. *Nature*, 514, 209-212

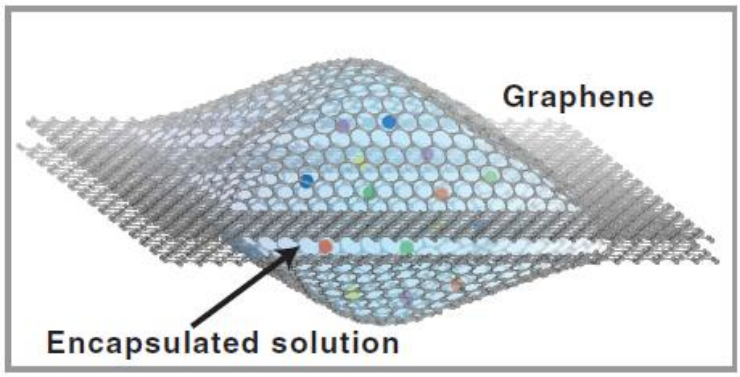

Figure 6.1. Graphene liquid encapsulation cell [1].

REFERENCES

US Energy Information Administration (2015) Annual energy outlook (US Dept of Energy, Washington, DC).

Santer, B. D., Taylor, K. E., Wigley, T. M. L., Johns, T. C., Jones, P. D., Karoly, D. J., Mitchell, J. F. B., Oort, A. H., Penner, J. E., Ramaswamy, V., Schwarzkopf, M. D., Stouffer, R. J. & Tett. S. (1996). A search for human influences on the thermal structure of the atmosphere, *Nature*, 382, 39-46

Hegerl, G. C., Storch, H.V., Hasselmann, K., Santer, B. D., Cubasch, U. & Jones, P. D. (1996). Detecting Greenhouse-Gas-Induced Climate Change with an Optimal Fingerprint Method," *Journal of Climate*, 9, 2281-2306

US Energy Information Administration. (2015). Levelized cost and levelized avoided cost of new generation resources in the Annual Energy Outlook 2015.

Scott, S. A., Davey, M. P., Dennis, J. S., Horst, I., Howe, C. J., Lea-Smith, D. J., Smith, A. G. (2010). Biodiesel from algae: Challenges and prospects. Current Opinion in Biotechnology, 21 (3), 277–286.

Darzins, A., Pienkos, P. &Edye, L.(2010). Current status and potential for algal biofuels production. IEA Bioenergy Task 39.

Ronneau, C. (2004), Energie, pollution de l'air et developpement durable, Louvain-la-Neuve: Presses Universitaires de Louvain.

Perret. R. (2011) Solar Thermochemical Hydrogen Production Research: Thermochemical Cycle Selection and Investment Priority. *Sandia Report*

Conibeer, G.J. & Richards, B.S. (2007). A comparison of PV/electrolyser and photoelectrolytic technologies for use in solar to hydrogen energy storage systems. *International Journal of Hydrogen Energy*, 32,2703–271.

James, B. D., Baum, G. N., Perez, J., Baum, K. N. (2009). Technoeconomic analysis of photoelectrochemical (PEC) hydrogen production. *DOE Report GS-10F-009J*

Fujishima, A., & Honda, K. (1972). Electrochemical photolysis of water at a semiconductor electrode. *Nature*, 238, 37-38.

Kudo, A., & Miseki, Y. (2009). Heterogeneous Photocatalyst Materials for Water Splitting. Chemical Society Review, 38, 253–278

Vasileia, M. D., Maria, A., Gianlucali, P., Dimitris, I. K. & Panagiotis, L. (2010). Solar Light-Responsive Pt/CdS/TiO2 Photocatalysts for Hydrogen Production and Simultaneous Degradation of Inorganic or Organic Sacrificial Agents in Wastewater. *Environmental Science Technology*, 44, 7200–7205

Ni, M., Leung, M. K. H., Leung, D. Y. C., & Sumathy, K. (2007). A review and recent developments in photocatalytic water-splitting using TiO_2 for hydrogen production. *Renewable Sustainable Energy Review*, 11, 401–425.

Wang, C. C., Zhang, Z., & Ying, J. Y. (1997). Photocatalytic decomposition of halogenated organics over nanocrystalline titania. *Nanostructured Materials*, 9,583-586

Zhang, Z., Wang, C. C., Zakaria, R., & Ying, J. Y. (1998). Role of particle size in nanocrystalline TiO_2-based photocatalysts. *Journal of Physical Chemistry B*, 102, 10871-10878

Gong, D., Grimes, C.A., Varghese, O.K., Hu, W.C., Singh, R.S., Chen, Z., & Elizabrth C.D. (2001). Titanium oxide nanotube arrays prepared by anodic oxidation. *Journal of Materials Research*, 16 (12), 3331–3334

Liu, B., & Aydil, E. S. (2009). Growth of Oriented Single-Crystalline Rutile TiO_2 Nanorods on Transparent Conducting Substrates for Dye-Sensitized Solar Cells. *Journal of American Chemical Society*, 131, 3985–3990

Subramanian, V., Wolf, E., & Kamat, P.V. (2001). Semiconductor-metal composite nanostructures: to what extent do metal nanoparticles improve the photocatalytic activity of TiO_2 films? *Journal of Physical Chemistry B*, 105, 11439–11446.

Greeley, J., Jaramillo, T.F., Bonde, J., Chorkendorff, I., & Nørskov, J. K. (2005). Computational high-throughput screening of electrocatalytic materials for hydrogen evolution. *Nature Materials*, 5, 909-913.

Anpo, M., & Takeuchi, M. (2003). The design and development of highly reactive titanium oxide photocatalysts operating under visible light rrradiation. *Journal of Catalysis*, 216, 505-516

Sakthivel, S., Shankar, M. V., Palanichamy, M., Arabindoo, B., Bahnemann, D. W., & Murugesan V. (2004). Enhancement of photocatalytic activity by metal deposition: characterization and photonic efficiency of Pt, Au and Pd deposited on TiO_2 catalyst. *Water Research*, 38, 3001-3008.

Wu, N.L., & Lee, M.S. (2004). Enhanced TiO_2 photocatalysis by Cu in hydrogen production from aqueous methanol solution. *International Journal of Hydrogen Energy*, 29(15), 1601-1605.

Bardos, E.S., Czili, H., & Horvath, A. (2003). Photocatalytic oxidation of oxalic acid enhanced by silver deposition on a TiO_2 surface. *Journal of Photochemistry & Photobiology A*: Chemistry, 154, 195-201.

So, W.W., Kim, K.J., & Moon, S.J. (2004). Photo-production of hydrogen over the CdS-TiO_2 nano-composite particulate films treated with $TiCl_4$. *International Journal of Hydrogen Energy*, 29, 229-234.

Keller, V., & Garin, F. (2003). Photocatalytic behavior of a new composite ternary system: WO_3/SiC-TiO_2 effect of the coupling of semiconductors and oxides in photocatalytic oxidation of methylethylketone in the gas phase. *Catalysis Commun*ication, 4, 377-383.

Domen, K., Kudo, A., & Onishi, T. (1986). Photocatalytic decomposition of water into H_2 and O_2 over NiO-$SrTiO_3$ powder 1: Structure of the Catalyst. *Journal of Physical Chemistry, 90*, 292-295

Domen, K., Kudo, A., & Onishi, T. (1986). Mechanism of Photocatalytic decomposition of water into H_2 and O_2 over NiOx/$SrTiO_3$. *Journal of. Catalysis*, *102*, 92-98.

Townsend, T. K., Browning, N. D., & Osterloh, F. E. (2012) Overall photocatalytic water splitting with NiOx–$SrTiO_3$ - a revised mechanism. *Energy Environmental Science*, 5, 9543

Maeda, K., Teramura, K., Lu, D., Takata, T., Saito, N., Inoue, Y., & Domen, K. (2006) Photocatalyst releasing hydrogen from water. *Nature*, 440, 295

Maeda, K., Hashiguchi, H., Masuda, H., Abe, R., & Domen K.(2008). Photocatalytic activity of $(Ga_{1-x}Zn_x)(N_{1-x}O_x)$ for visible-light-driven H_2 and O_2 evolution in the presence of sacrificial reagents. *Journal of Physical Chemistry C*, 112 (9), 3447–3452

Yoshida, M., Takanabe, K., Maeda, K., Ishikawa, A., Kubota, J., Sakata, Y., Ikezawa, Y., & Domen K. (2009) Role and function of noble-metal/Cr-layer core/shell structure cocatalysts for photocatalytic overall water splitting studied by model electrodes. *Journal of Physical Chemistry C*, 113, 10151–10157

Yamashita, H., Harada, M., Misaka, J., Takeuchi, M., Ichihashi, Y., & Goto, F., et al. (2001). Application of ion beam techniques for preparation of metal ion-implanted TiO_2 thin film photocatalyst available under visible irradiation: metal ion-implantation and ionized cluster beam method. *Journal Synchrotron Radiation*, 8, 569-571.

Li, X., Lu, X., & Li, B. (2003). Photocatalytic production of hydrogen in single component and mixture systems of electron donors and monitoring adsorption of donors by in situ infrared spectroscopy. *Chemosphere*, 52(5), 843-850.

Dhanalakshmi, B., Latha, S., Anandan, S., Maruthamuthu, P. (2001). Dye sensitized hydrogen evolution from water. *International Journal of Hydrogen Energy*, 26. 669-674.

Fujishima, A., Zhang, X., Tryk, D. A., (2008). TiO_2 Photocatalysis and Related Surface Phenomena. *Surface Science Re*ports, 63, 515-582

Henderson, M. A. (1996). An HREELS and TPD study of water on TiO_2 (110): the extent of molecular versus dissociative adsorption. *Surface Science*, 355, 151−166.

Bikondoa, O., Pang, C. L., Ithnin, R., Muryn, C., Onishi, H., & Thorton, G. (2006). Direct visualization of defect-mediated dissociation of water on TiO_2 (110). *Nature Materials*, 5, 189−192.

Wendt, S., Matthiesen, J., Schaub, R., Vestergaard, E. K., Lagsgaard, E., Besenbacher, F., & Hammer, B. (2006). Formation and Splitting of Paired Hydroxyl Groups on Reduced TiO_2 (110). *Physical Review Letter*, 96, 066107.

Wendt, S., Schaub, R., Matthiesen, J., Vestergaard, E. K., Wahlstrom, E., Rasmussen, D., Thorstrup, P., Molina, L. M., Lagsgaard, E., Stensgaard, I., Hammer, B., & Besenbacher, F. (2005). Oxygen vacancies on TiO_2 (110) and their interaction with H_2O and O_2: A combined high-resolution STM and DFT study. *Surface Science*, 598, 226−245.

Knoll, M. & Ruska E. (1932). Das Elektronenmikroskop. *Zeitschrift fuer Physik*, 78, 318-339.

Williams, D. W., & Carter, C. B. (2009). Transmission electron microscopy. 2nd Edition. New York: Springer.

Wang, C. W., Xu, W., Liu, J., Choi, D.W., Arey, B., Saraf, L. V., Zhang, J.G., Yang, Z.G., Thevuthasan, S., Baer, D.R., & Salmon, N. (2010). *In-situ* transmission electron microscopy and spectroscopy studies of interfaces in Li ion batteries: Challenges and opportunities. *Journal of Materials Research*, 25(8), 1541-1547.

Minor, A. M., Asif, S. A. S., Shan, Z. W., Stach, E. A., Cyrankowski, E., Wyrobek, T. J., & Warren, O. L. (2006). A new view of the onset of plasticity during the nanoindentation of aluminium. *Nature Materials*, 5, 697-702

Cavalca, F., Laursen, A. B., Kardynal, B. E., Dunin-Borkowski, R. E., Dahl, S., Wagner, J. B. & Hansen, T. W. (2012) *In situ* transmission electron microscopy of light-induced photocatalytic reactions *Nanotechnology*, 23, 075705 (6pp)

Miller, B.K.; Crozier, P.A. (2013). System for In Situ UV-Visible Illumination of ETEM Samples *Microscopy & Microanalysis*, 19(2), 461-469.

G. M. Parkinson. (1989). High resolution, *in-situ* controlled atmosphere transmission electron microscopy (CATEM) of heterogeneous catalysts. *Catalysis Letters*, 2, 303-308

Creemer, J.F., Helveg, S., Hovelingc, G.H., Ullmannb, S., Molenbroekb, A.M., Sarroa, P.M. & Zandbergend, H.W. (2008) Atomic-scale electron microscopy at ambient pressure. Ultramicroscopy, 108, 9, 993–998

Giorgio, S., Sao Joao, S., Nitsche, S., Chaudanson, D., Sitja, G. & Henry, C.R. (2006). Environmental electron microscopy (ETEM) for catalysts with a closed E-cell with carbon windows. *Ultramicroscopy*, 106, 503-507

Yokosawa, T., Alan, T., Pandraud, G., Dam, B. & Zandbergen, H. (2012). *In-situ* TEM on hydrogenation of Pd at 0.5–4.5 bar hydrogen pressure and 20–400 ℃. *Ultramicroscopy*,112 (1), 47-52.

Hansen, T. W., Wagner, J. B., Hasen, P. L., Dahl, S., Topsoe, H., & Jacoboson, C.J.H. (2001). Atomic-resolution *in-situ* transmission electron microscopy of a promoter of a heterogeneous catalyst. *Science*, 294, 1508-1510.

Sharma, R. (2005). An environmental transmission electron microscope for *in-situ* synthesis and characterization of nano materials. *Journal of Materials Research*, 20(7), 1695-1707.

Li, P., Liu, J., Nag, N., & Crozier, P. A. (2005). Atomic-scale study of *in-situ* metal nanoparticles synthesis in a Ni/TiO2 system. *Journal of Physical Chemistry B*, 109(29), 13883-13890.

Gai, P. (1998). Direct probing of gas molecule—solid catalyst interactions on the atomic scale. *Advanced Materials*, 10, 1259-1263.

Gai, P., & Boyes, E. D. (2009). Advances in atomic resolution *in-situ* environmental transmission electron microscopy and 1Å aberration corrected *in-situ* electron microscopy. *Microscopy Research and Technique*, 72, 153-164

Tennet, R.M. (1971). Science Data Book. Oliver & Boyd.

Knoll, M. & Ruska E. (1932). Das Elektronenmikroskop. *Zeitschrift fuer Physik*, 78, 318-339.

Orloff, J. (1989). Survey of Electron Sources for High-Resolution Microscopy, *Ultramicroscopy*, 58, 88-97.

Williams, D. W., & Carter, C. B. (2009). Transmission electron microscopy. 2nd Edition. New York: Springer.

Van Dyck, D. & De Jong, A. F. (1992). Ultimate resolution and information in electron microscopy: general principles. Ultramicroscopy, 47, 266-281

De Jong, A. F. & Van Dyck, D. (1993). Ultimate resolution and information in electron microscopy. II. The information limit of transimission electron microscope. Ultramicroscopy, 49, 66-80.

Treacy, M. M. J., & Howie, A. (1980). Contrast Effects in the Transmission Electron Microscopy of Supported Crystalline Catalyst Particles. *Journal of Catalyst*, 63, 265-269

Treacy, M. M. J., Howie, A., & Wilson, C. J. (2006). Z Contrast of Platinum and Palladium Catalysts. *Philosophical Magazine A,* 38(5), 569-585.

Micheal, J.R. and Williams, D.B. (1987). A consistent definition of probe size and spatial resolution in the analytical electron microscope. *Journal of Microscopy*, 147, 289-303

Kimoto, K. (2014). Practical Aspects of Monochromators Developed for Transmission Electron Microscopy. *Microscopy*, 63(5), 337-344.

Rose, H. H. (2008). Optics of high-performance electron-microscopes. *Science and Technology of. Advanced Materials*, 9, 014107 (30pp).

Tanaka, N. (2008). Present status and future prospects of spherical aberration corrected TEM/STEM for study of nanomaterials. *Science and Technology of. Advanced Materials*, 9, 014111 (11pp).

Sharma, R., Zafar, I. (2004). In situ observations of carbon nanotube formation using environmental electron microscopy (ETEM). *Applied Physics Letter*, 84, 990-992
Sharma, R., Rez, P., Brown, M., Du, G., Treacy, M. M. J. (2007). Dynamic observations of the effect of pressure and temperature conditions on the selective synthesis of carbon nanotubes. *Nanotechnology*, 18, 125602 (8pp).

Hannon, J.B., Kodambaka, S., Ross, F. M., Tromp, R. M. (2006). The influence of the surface migration of gold on the growth of silicon nanowires. *Nature*, 440, 69–71.

Yoshida K., Yamasaki J. & Tanaka N. (2004). In situ high-resolution transmission electron microscopy observation of photodecomposition process of poly-hydrocarbons on catalytic TiO_2 films. *Applied Physics Letters*, 84, 2542-2544

Yoshida K., Nanbara, T., Yamasaki J., Tanaka, N. (2006), Oxygen release and structural changes in TiO2 films during photocatalytic Oxidation, *Journal of Applied Physics,* 99, 084908

Cavalca F., Laursen A. B., Wagner, J. B., Damsgaard, C. D., Chorkendorff, I. & Hansen T. W. (2013) Light-induced reduction of cuprous oxide in an environmental transmission electron microscope. *ChemCatChem,* 5, 2667-2672.

Cavalca, F., Laursen, A. B., Kardynal, B. E., Dunin-Borkowski, R. E., Dahl, S., Wagner, J. B. & Hansen, T. W. (2012) *In situ* transmission electron microscopy of light-induced photocatalytic reactions *Nanotechnology*, 23, 075705 (6pp)

Miller, B.K.; Crozier, P.A. (2013). System for In Situ UV-Visible Illumination of ETEM Samples *Microscopy & Microanalysis,* 19(2), 461-469

Ray, S. & Shard, A.G. (2011). Quantitative Analysis of Adsorbed Proteins by X-ray Photoelectron Spectroscopy. *Analytical Chemistry*, 83(22), 8659-8666

Krivanek, O. L., Lovejoy, T. C., Dellby, N., Aoki, T., Carpenter, R. W., Rez, P., Soignard, E., Zhu, J., Batson, P. E., Lagos, M. J., Egerton R. F. & Crozier P. A. (2014). Vibrational spectroscopy in the electron microscope. *Nature*, 514, 209-212

Sharma, R. (2005). An environmental transmission electron microscope for in-situ synthesis and characterization of nanomaterials. *Journal of Materials Research*, 20(7), 1695-1707.

Zhang L., Miller B. K. & Crozier P.A. (2013). Atomic level in situ observation of surface amorphization in anatase nanocrystals during light irradiation in water vapor. *Nano Letters*, 13(2), 679–684.

Lu, D., Takata, T., Saito, N., Inoue, Y., Domen, K. (2006). Photocatalyst releasing hydrogen from water. *Nature*, 440, 295.

Maeda, K., Teramura, K., Domen, K. (2008). Effect of post-calcination on photocatalytic activity of $(Ga_{1-x}Zn_x)(N_{1-x}O_x)$ solid solution for overall water splitting under visible light. *Journal of Catalyst*, 254 (2),198−204.

Reece, S. Y., Hamel, J. A., Sung, K., Jarvi, T. D., Esswein, A. J., Pijpers, J. J. H., & Nocera, D. G. (2011). Wireless solar water splitting using silicon-based semiconductors and earth-abundant catalysts. *Science*, 334 (6056), 645−648.

Chen, X., & Mao, S. S. (2007). Titanium dioxide nanomaterials: synthesis, properties, modifications, and applications. *Chemical Review*, 107, 2891−2959.

Awazu, K., Fujimaki, M., Rockstuhl, C., Tominaga, J., Murakami, H., Ohki, Y., Yoshida, N., & Watanabe, T. (2008). A plasmonic photocatalyst consisting of silver nanoparticles embedded in titanium dioxide. *Journal of American Chemical Society*, 130, 1676−1680.

Slamet, Nasution, H. W., Purnama, E., Kosela, S., & Gunlazuardi, J. (2005). Photocatalytic reduction of CO_2 on copper-doped Titania catalysts prepared by improved-impregnation method. *Journal of Catalyst Community,* 6, 313−319.

Tseng, I. H., & Wu, J. C. S. (2004). Chemical states of metal-loaded titania in the photoreduction of CO_2. *Catalysis Today*, 97, 113−119.

Fujishima, A., Zhang, X. T., & Tryk, D. A. (2008). TiO_2 photocatalysis and related surface phenomena. *Surface Science Reports*, 63(12), 515−582.

Henderson, M. A. (1996). An HREELS and TPD study of water on TiO_2 (110): the extent of molecular versus dissociative adsorption. *Surface Science*, 355, 151−166.

Bikondoa, O., Pang, C. L., Ithnin, R., Muryn, C., Onishi, H., & Thorton, G. (2006). Direct visualization of defect-mediated dissociation of water on TiO_2 (110). *Nature Materials*, 5, 189−192.

Wendt, S., Matthiesen, J., Schaub, R., Vestergaard, E. K., Lagsgaard, E., Besenbacher, F., & Hammer, B. (2006). Formation and Splitting of Paired Hydroxyl Groups on Reduced TiO_2 (110). *Physical Review Letter*, 96, 066107.

Wendt, S., Schaub, R., Matthiesen, J., Vestergaard, E. K., Wahlstrom, E., Rasmussen, D., Thorstrup, P., Molina, L. M., Lagsgaard, E., Stensgaard, I., Hammer, B., & Besenbacher, F. (2005). Oxygen vacancies on TiO_2 (110) and their interaction with H_2O and O_2: A combined high-resolution STM and DFT study. *Surface Science*, 598, 226−245.

Zhang L., Miller B. K. & Crozier P.A. (2013). Atomic level in situ observation of surface amorphization in anatase nanocrystals during light irradiation in water vapor. *Nano Letters*, 13(2), 679–684.

Zhu, H. Y., Lan, Y., Gao, X. P., Ringer, S. P., Zheng, Z. F., Song, D. Y., & Zhao, J. C. (2005). Phase transition between nanostructures of titanate and titanium dioxides via simple wet-chemical reactions. *Journal of American Chemical Society*, l (127), 6730−6736.

Deng, Q., Wei, M., Hong, Z., Ding, X., Jiang, L., & Wei, K. (2010). Selective synthesis of rutile, anatase, and brookite nanorods by a hydrothermal route. *Nanoscience*. 6, 479−482.

Banerjee, R., Crozier, P.A. (2012*). In situ* synthesis and nanoscale evolution of model supported metal catalysts: Ni on silica. *Journal of Physical Chemistry C*, 116 (21), 11486−11495.

Crozier, P. A., McCartney, M. R., & Smith, D. J. (1990). Observation of exit surface sputtering in TiO_2 using biased secondary electron imaging. *Surface Science.* 237 (1−3), 232−240.

McCartney, M. R., Crozier, P. A., Weiss, J. K., & Smith, D. J. (1991). Electron-beam-induced reactions at transition-metal oxide surfaces. *Vacuum*. 42 (4), 301−308.

Wang, L. Q., Baer, D. R., & Engelhard, M. H. (1994). Creation of variable concentrations of defects on TiO_2 (110) using low-density electron beam. *Surface Science*, 320,295−306.

Shultz, A. N., Jang, W., Hetherington, W. M., Baer, D. R., Wang, L. Q., & Engelhard, M. H. (1995). Comparative second harmonic generation and X-ray photoelectron spectroscopy studies of the UV creation and O_2 healing of Ti^{3+} defects on (110) rutile TiO_2 surfaces. *Surface Science.* 1995, 339, 114−124.

Wang, L. Q., Baer, D. R., Engelhard, M. H., & Shultz, A. N. (1995). The adsorption of liquid and vapor water on TiO_2 (110) surfaces: the role of defects. *Surface Science*. 344, 237−250.

Egerton, R. F. (2011). Electron Energy-Loss Spectroscopy in the Electron Microscope, 3rd ed.; Springer; New York.

Wang, Z., Helmersson, U., Kall P. (2002). Optical properties of anatase TiO_2 thin films prepared by aqueous sol–gel process at low temperature. *Thin Solid Film*, 405, 50-54.

Muller, D., Nakagawa, N., Ohtomo, A., Grazul, J., & Hwang, H. (2004). Atomic-scale imaging of nanoengineered oxygen vacancy profiles in $SrTiO_3$. *Nature*. 430, 657−661.

Sakai, N., Fujishima, A., Watanabe, T., & Hashimoto, K. (2001). Enhancement of the photoinduced hydrophilic conversion rate of TiO_2 film electrode surfaces by anodic polarization. *Journal of Physical Chemistry B,* 105 (15), 3023–3026

Henderson, M. A. (1996). Structural sensitivity in the dissociation of water on TiO_2 single-crystal surface. *Langmuir*, 12, 5093−5098.

Wang, R., Hashimoto, K., Fujishima, A., Chikuni, M., Kojima, E., Kitamura, A., Shimohigoshi, M., & Watanabe, T. (1998). Photogeneration of Highly Amphiphilic TiO_2 Surfaces. *Advanced Materials*, 10(2), 135−138.

Watanabe, T., Nakajima, A., Wang, R., Minabe, M., Koizumi, S., Fujishima, A., & Hashimoto, K. (1999). Photocatalytic activity and photoinduced hydrophilicity of titanium dioxide coated glass. *Thin Solid Films*, 351, 260−263.

Varghese, O. K., Gong, D., Paulose, M., Ong, K. G., Dickey, E.C., & Grimes, C. A. (2003). Extreme changes in the electrical resistance of titania nanotubes with hydrogen exposure. *Advanced Materials*, 15 (7−8),624−627.

Jakob, M., Levanon, H. & Kamat, P.V. (2003). Charge distribution between UV-irradiated TiO_2 and gold nanoparticles: determination of shift in the fermi level. *Nano Letters*, 3(3), 353–358.

Liu, S., Qu, Z., Han, X. & Sun, C. (2004). A mechanism for enhanced photocatalytic activity of silver-loaded titanium dioxide. *Catalysis Today*, 93–95, 877–884.

Sakthivel, S., Shankar, M.V., Palanichamy, M., Arabindoo, B., Bahnemann, D.W. & Murugesan, V. (2004). Enhancement of photocatalytic activity by metal deposition: characterization and photonic efficiency of Pt, Au and Pd deposited on TiO_2 catalyst. *Water Research*, 38, 3001–3008.

Subramanian, V., Wolf, E. & Kamat, P.V. (2001). Semiconductor-metal composite nanostructures: to what extent do metal nanoparticles improve the photocatalytic activity of TiO_2 films? *Journal of Physical Chemistry B*, 105, 11439–11446.

Anpo, M. & Takeuchi, M. (2010), The design and development of highly reactive titanium oxide photocatalysts operating under visible light irradiation. *Journal of Catalysis*, 216, 505-516

Greeley, J., Jaramillo, T.F., Bonde, J., Chorkendorff, I. & Nørskov, J.K. (2005) Computational high-throughput screening of electrocatalytic materials for hydrogen evolution. *Nature Materials*, 5, 909-913.

Wynblatt, P. & Gjostein, N.A. (1975). Supported metal crystalletes, *Progress in. Solid State Chemitry*. 9, 21-58.

Bartholomew, C.H. (2001). Mechanisms of catalyst deactivation. *Applied. Catalysis A*, 212, 17-60.

Farrauto, R.J. & Bartholomew, C.H. (1997). Fundamentals of industrial catalytic processes, Chapman & Hall, Kluwer Academic Publishers, London, Chapter 5.

Bell, A.T. (2003). The impact of nanoscience on heterogeneous catalysis. *Science*, 299, 1688-1691.

Ferreira, P.J., la O' G. J., Shao-Horn Y., Morgan D., Makharia R., Kocha S. & Gasteiger H.A.(2005). Instability of Pt/C electrocatalysts in proton exchange membrane fuel cells: A mechanistic investigation. *Journal of. Electrochemical. Society,* 152 (A), 2256–2271.

Shao-Horn, Y., Sheng, W. C., Chen S., Ferreira, P. J., Holby, E. F. & Morgan, D. (2007). Instability of supported platinum nanoparticles in low-temperature fuel cells. *Topics in Catal*ysis, 46(3-4), 285-305.

Wanke, S.E. & Flynn, P.C. (1975), The sintering of supported metal catalysts. *Catalysis Review,* 12, 93-135.

Simonsen, S.B., Chorkendorff, I., Dahl, S., Skoglundh, M., Sehested, J. & Helveg, S. (2011). Ostwald ripening in a Pt/SiO_2 model catalyst studied by i*n situ* TEM. *Journal of Catalysis*, 281,147–155.

Asoro, M.A., Kovar, D., Shao-Horn, Y., Allard, L.F. & Ferreira, P.J. (2010), Coalescence and sintering of Pt nanoparticles:in situ observation by aberration-corrected HAADF STEM. *Nanotechnology,* 21, 025701 (6pp).

Harris, P.J.F. (1986). The sintering of platinum particles in an alumina-supported catalyst: further transmission electron microscopy studies. *Journal of Catalysis*, 97(2), 527–542.

Parthasarathy, P. & Virkar, A.V. (2013). Electrochemical Ostwald ripening of Pt and Ag catalysts supported on carbon, *Journal of Power Sources,* 234, 82-90.

Ohtani, B., Iwai, K., Nishimoto, S. & Sato, S. (1997). Role of platinum deposits on titanium (IV) oxide particles: structural and kinetic analyses of photocatalytic reaction in aqueous alcohol and amino acid solutions. *Journal of Physical Chemistry B*, 101, 3349-3359.

Sayama, K. & Arakawa, H. (1997). Effect of carbonate salt addition on the photocatalytic decomposition of liquid water over catalyst. *Journal of Chemical Society, Faraday Transactions,* 93(8), 1647-1654.

Zhang L., Miller B. K. & Crozier P.A. (2013). Atomic level in situ observation of surface amorphization in anatase nanocrystals during light irradiation in water vapor. *Nano Letters,* 13(2), 679–684.

Treacy, M. M. J. & Howie, A. (1980). Contrast effects in the rransmission electron microscopy of supported crystalline catalyst particles. *Journal of Catalysis,* 63, 265-269.

Treacy, M. M. J., Howie, A. & Wilson, C. J. Z. (2006). Contrast of platinum and palladium catalysts. *Philosophical Magazine. A,* 38(5), 569-585.

Miller, B.K. & Crozier, P.A (2013). System for in *situ* UV-Visible illumination of ETEM samples. *Microscopy and Microanalysis,* 19(2), 461-469.

Tang, L., Li, X., Cammarata, R. C., Friesen, C. & Sieradzki, K. (2010). Electrochemical Stability of Elemental Metal Nanoparticles. *Journal of American Chemical Society,* 132, 11722-11726.

Diebold, U. (2003). The Surface Science of Titanium Dioxide**.** *Surface Science Reports*, 48, 53-229.

Pomoni, K., Sofianou, M.V., Georgakopoulos, T., Boukos, N. & Trapalis, C. (2013). Electrical Conductivity Studies of Anatase TiO_2 with Dominant Highly Reactive {001} Facets. Journal of Alloys Compounds. 548, 194-200.

Watanabe, Y., Muramoto, Y. & Shimizu, N.(2011) Electronic Conduction Properties of TiO_2 Thin Films Under UV Light Irradiation. *Annual Report Conference on Electrical Insulation and Dielectric Phenomena (CEIDP),* 117-120.

Fujishima, A., Zhang, X. & Tryk, D. A. (2008). TiO_2 Photocatalysis and Related Surface Phenomena. *Surface Science Reports*. 63, 515-582.

Redmond, P. L., Hallock, A. J., & Brus, L. E. (2005). Electrochemical ostwald ripening of colloidal Ag particles on conductive substrates. *Nano Lett*ers, 5(1), 131-135.

Yamaguti, K., & S. Sato, S. (1985). Photolysis of water over metallized powdered titanium dioxide. *Journal of Chemical Society, Faraday Transactions 1*, 81, 1237-1246.

Sayama, K., & Arakawa, H. (1997). Effect of carbonate salt addition on the photocatalytic decomposition of liquid water over Pt–TiO_2 catalyst. *Journal of Chemical Society, Faraday Transanctions*, 93, 1647-1654.

Tabata, S., Nishida, H., Masaki Y. & Tabata, K. (1995). Stoichiometric photocatalytic decomposition of pure water in Pt/TiO_2 aqueous suspension system, *Catalysis Letters,* 34, 245–249.

Kudo A. & Kato. H. (2000). Effect of lanthanide-doping into $NaTaO_3$ photocatalysts for efficient water splitting. *Chemical Physics Letter,* 331 (5-6), 373-377.

John, M. R., Furgals, A. J. & Sammells. A. F. (1983). Hydrogen generation by photocatalytic oxidation of glucose by platinized n-TiO_2 powder. *Jounal of Physical Chemistry*, 87, 801-805.

Subramanian, V., Wolf, E. & Kamat, P. (2001). Semiconductor-metal composite nanostructures, to what extent do metal nanoparticles improve the photocatalytic activity of TiO_2 films? *Jounal of Physical Chemistry B*, 105, 11439-11446.

Jakob, M., Levanon, H., & Kamat, P.V. (2003). Charge distribution between UV-irradiated TiO_2 and gold nanoparticles: determination of shift in the fermi level. *Nano Letters*, 3(3), 353-358

Gurunathan, K., Maruthamuthu, P. & Sastri, V.C. (1997). Photocatalytic hydrogen production by dye-sensitized Pt/SnO_2 and Pt/SnO_2/RuO_2 in aqueous methyl viologen solution. *International Journal of Hydrogen Energy*, 22(1), 57-62.

Keller, V. & Garin, F. (2003). Photocatalytic behavior of a new composite ternary system: WO_3=SiC-TiO_2. effect of the coupling of semiconductors and oxides in photocatalytic oxidation of methylethylketone in the gas phase. *Catalysis Communications,* 4, 377-383.

Kang, M. G., Han, H. E., & Kim, K.J. (1999). Enhanced photodecomposition of 4-chlorophenol in aqueous solution by deposition of CdS on TiO_2. *Journal of Photochemical Photobiology A: Chemstry*, 125, 119-125

Wang, W., .Liu, S., Nie, L., Cheng, B. & Yu, J., (2013). Enhanced photocatalytic H_2-production activity of TiO_2 using $Ni(NO_3)_2$ as an additive. *Physcial Chemistry Chemical Physics*, 15, 12033-12039

Yu, J.; Hai, Y. & Cheng, B. (2011). Enhanced Photocatalytic H_2-Production Activity of TiO_2 by $Ni(OH)_2$ Cluster Modification. *Journal of Physical Chemistry C*, 115, 4953–4958.

Chen, S., Chen, X., Jiang, Q., Yuan, J., Lin, C. & Shangguan W. (2014). Promotion effect of nickel loaded on CdS for photocatalytic H2production in lactic acid solution. *Applied Surface Science*, 316, 590-594.

Lin J., Yana, S., Huang, Q., Fan, M., Yuan, Y., Tan T. & Liao, D. (2014). TiO_2 promoted by two different non-noble metal co-catalysts for enhanced photocatalytic H_2 evolution. *Applied Surface Science*, 309, 188-193.

Cui, E. & Lu, G. (2014). Enhanced surface electron transfer by fabricating a core/shell Ni@NiO cluster on TiO_2 and its role on high efficient hydrogen generation under visible light irradiation. *International Journal of Hydrogen Energy*, 39, 8959-8968.

Sreethawong, T., Suzuki, Y. & Yoshikawa, S. (2005). Photocatalytic evolution of hydrogen over mesoporous TiO_2 supported NiO photocatalyst prepared by single-step sol–gel process with surfactant template. *International Journal of Hydrogen Energy*, 30, 1053-1062.

Kim, J., Hwang, D. W., Kim, H. G., Bae, S. W., Lee, J. S., Li W. & Oh. S. H. (2005). Highly efficient overall water splitting through optimization of preparation and operation conditions of layered perovskite photocatalysts**.** *Topics Catalysis*, 35, 295-303.

Domen, K., Kudo, A., Shinozaki, A., Tanaka, A., Maruya, K., & Onishi, T. (1986) Photodecomposition of water and hydrogen evolution from aqueous methanol solution over novel niobate photocatalysts. *Journal of Chemical Society, Chemical Communication*s, 356-357

Kudo, A.; Domen, K.; Maruya, K.; Onishi, T. (1987), Photocatalytic Activities of TiO_2 Loaded with NiO. *Chemical Physics Letters*, 133, 517-519.

Kudo, A. & Miseki, Y. (2009). Heterogeneous photocatalyst materials for water splitting. *Chemical Society Review*, 38, 253–278

Domen, K., Kudo, A. & Onishi, T. (1986). Mechanism of photocatalytic decomposition of water into H_2 and O_2 over $NiOx/SrTiO_3$. *Journal of Catalysis.* 102, 92–98.

Townsend, T. K., Browning N. D. & Osterloh. F. E. (2012). Overall photocatalytic water splitting with NiO_x–$SrTiO_3$ – a revised mechanism. *Energy & Environmental Science,* 5, 9543-9550

Domen, K., Naito, S., Onishi, T. & Tamaru, K. (1982) Study of the photocatalytic decomposition of water vapor over a nickel(II) oxide-strontium titanate ($SrTiO_3$) catalyst. *Journal of Physical Chemistry*, 86, 3657–3661.

Matsumotoa, Y., Unala, U., Tanakaa, N., Kudob, A. & Kato, H. (2004) Electrochemical approach to evaluate the mechanism of photocatalytic water splitting on oxide photocatalysts. *Journal of Solid State Chemistry*, 177, 4205–4212

Hansen, K. K. (2008). Electrochemical reduction of O_2 and NO on Ni, Pt and Au. *Journal of Appled Electrochemistry*, 38, 591–595.

Yoshida, M., Takanabe, K., Maeda, K., Ishikawa, A., Kubota, J., Sakata, Y., Ikezawa, Y. & Domen, K. (2009). Role and function of noble-metal/Cr-layer core/shell structure cocatalysts for photocatalytic overall water splitting studied by model electrodes. *Journal of Physical Chemistry C*, 113, 10151–10157.

Kiwi, J. & Griltzel, M. (1984). Optimization of conditions for photochemical water cleavage. Aqueous platinum/TiO_2 (anatase) dispersions under ultraviolet light. *Journal of Physical Chemistry*, 88, 1302-1307

Meissner, D., Benndorf, C. & Memming R. (1987). Photocorrosion of cadmium sulfide: Analysis by photoelectron spectroscopy. *Applied Surface Science.* 27, 423-436

Fermín, D.J., Ponomarev E.A. & Peter, L.M. (1999). A kinetic study of CdS photocorrosion by intensity modulated photocurrent and photoelectrochemical impedance spectroscopy. *Journal of Electroanalytical Chemistr*, 473, 192–203

Dai, G., Yu, J. & Liu, G. (2012). A new approach for photocorrosion inhibition of Ag_2CO_3 photocatalyst with highly visible-light-responsive reactivity. *Journal of Physical Chemistry C*, 116, 15519−15524

Tauster, S. J., (1987). Strong metal-support interactions. *Accounts of Chemical Research*, 20(11), 389-394.

Sharma, V., Crozier, P. A., Sharma, R. & Adams，J. B. (2012). Direct observation of hydrogen spillover in Ni-loaded Pr-doped ceria. *Catalysis Today*, 180(1), 2-8.

Ishibashi, K., Fujishima, A., Watanabe, T. & Hashimoto, K., (2011), Detection of active oxidative species in TiO_2 photocatalysis using the fluorescence technique. *Electrochemitry Communications*, 47, 6906–6908.

Xiao, Q., Si, Z., Zhang, J., Xiao, C. & Tan, X. (2008), Photoinduced hydroxyl radical and photocatalytic activity of samarium-doped TiO_2 nanocrystalline. *Journal of Hazardous Materials*, 150, 62-67.

Xiang, Q., Yu, J., Wang, W. & Jaroniec, M. (2011). Nitrogen self-doped nanosized TiO_2 sheets with exposed {001} facets for enhanced visible-light photocatalytic activity. *Chemical Communications,* 47, 6906-6908.

Vaníysek, P. (2011). Electrochemical Series. Handbook of Chemistry and Physics: 92nd Edition

Chenna, S. & Crozier, P.A. (2012). In situ environmental transmission electron microscopy to determine transformation pathways in supported Ni nanoparticles. *Micron,* 43, 1188-1194

Peraldi, R., Monceau, D. & Pieraggi, B. (2002). Correlations between growth kinetics and microstructure for scales formed by high-temperature oxidation of pure nickel. II. growth kinetics. *Oxidation of Metals,* 58,275-295

Yuk, J.M., Park, J., Ercius, P., Kim, K., Hellebusch, D.J., Crommie, M.F., Lee, J.Y., Zettl, A.& Alivisatos, A.P. (2012), High-Resolution EM of colloidal nanocrystal growth using graphene liquid cells, *Science*,336(6077), 61-64.

Krivanek, O. L., Lovejoy, T. C., Dellby, N., Aoki, T., Carpenter, R. W., Rez, P., Soignard, E., Zhu, J., Batson, P. E., Lagos, M. J., Egerton R. F. & Crozier P. A. (2014). Vibrational spectroscopy in the electron microscope. *Nature*, 514, 209-212

APPENDIX A

TIO_2 OPTICAL DATA AND PHOTON ENERGY ABSORPTION

The Optical data of TiO_2 is gained from the reference by Wang, Z. et al.

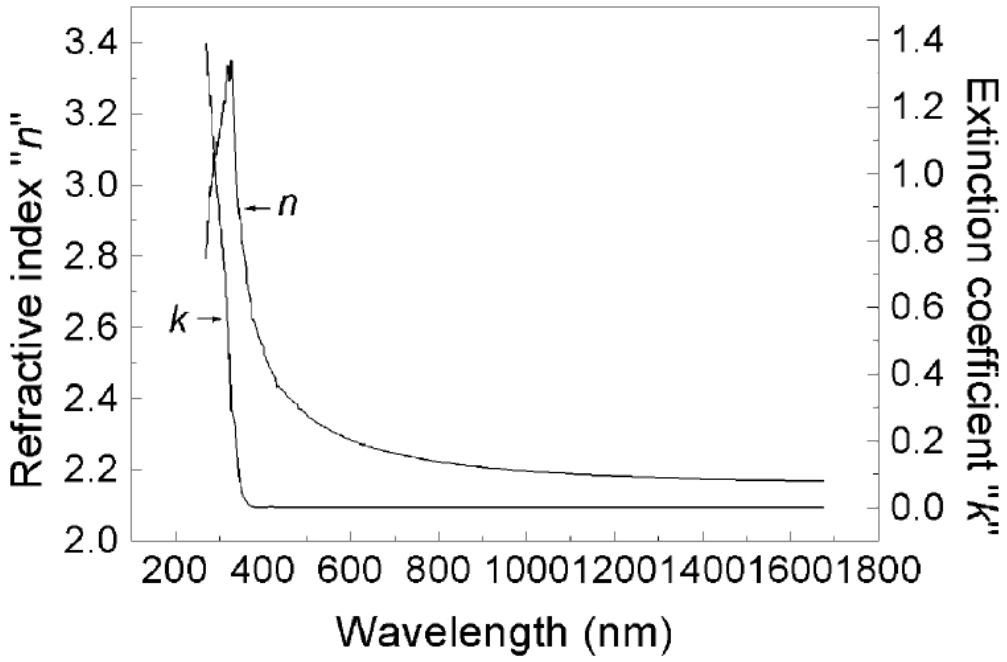

Figure Appendix A.1. Optical constants, n and *K*, of the 350 ℃ annealed TiO_2 thin film.

According to the n, *K* shown in the above graph, the real part ε_1 and imaginary part ε_2 of the relative permittivity can be calculated and plotted as following:

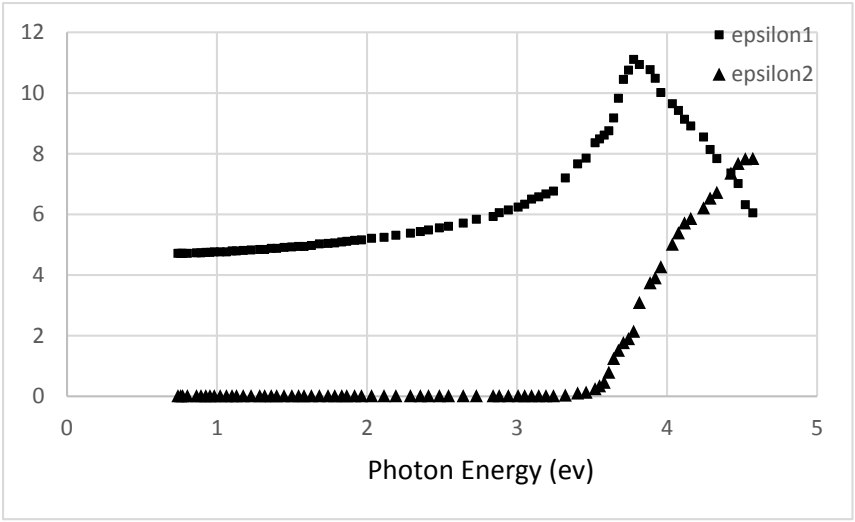

Figure Appendix A.2.TiO_2 anatase dielectric data.

The absorption coefficient can thus be calculated by $\alpha_\lambda = 4\pi K/\lambda$.

$$\int I_\lambda[1 - \exp(-\alpha_\lambda t)]d\lambda$$

where t is the thickness of the sample, I_λ is the photon intensity at wavelength λ

I_λ distribution is as follows:

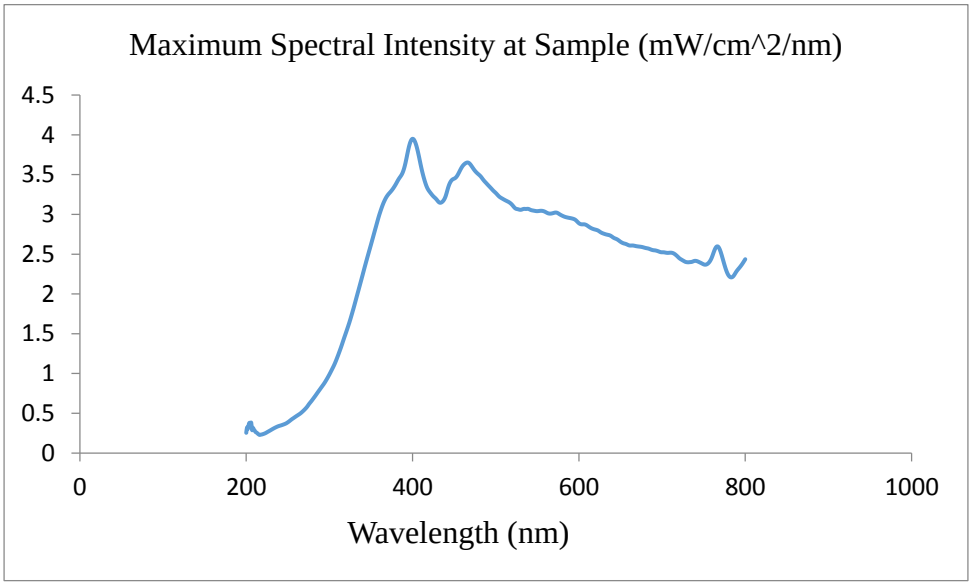

Wang, Z.; Helmersson, U.; Kall, P. Optical Properties of Anatase TiO_2 Thin Films Prepared by Aqueous Sol–gel Process at Low Temperature. *Thin Solid Films*, **2002**, 405, 50–54

More dielectric data can be found in following papers about the TiO_2 rutile and anatase:

Landmann, M.; Rauls, E.; Schmidt, W. G. The Electronic Structure and Optical Response of Rutile, Anatase and Brookite TiO_2. *J. Phys.: Condens. Matter*, **2012**, 24 195503 (6pp)

Glassford, K. M., & Chelikowsky, J. R. (1992). Structural and electronic properties of titanium dioxide. *Phys. Rev. B*, 46, 1284−1897.

APPENDIX B

IRRADIATION DAMAGE FOR *IN-SITU* CHARACTERIZATION

1. Calculation of the Energy Transfer Due to Elastic Scattering

For a thin film, the elastically scatter signal I_e can be related to the elastic cross section σ through the equation

$$I_e = I_o N_A \sigma \quad (1)$$

where N_A is the number of atoms per area.

The probability P_e of this event occurring is then given by

$$P_e = I_e/I_o = N_A \sigma \quad (2)$$

The energy transferred by a series of elastic collisions involving N_e electrons can then be calculated using the formula:

$$E=N_e \int_0^{Emax} N_A \frac{d\sigma}{d\Delta E} \Delta E \, d\Delta E \quad (3)$$

where ΔE is the certain energy loss caused by elastic collisions.

The quantity dσ/dΔE is the energy differential cross section for elastic collisions. Since the the elements of interest here are relatively light, we can ignore electron exchange effects and use a modified Rutherford cross section together with a simple Wentzel potential to take electron screening into account to get the form (see for example, reference Egerton et al. for details).

$$\frac{d\sigma}{d\Delta E} = \frac{1}{16\pi\varepsilon_0{}^2} \frac{Z^2 e^4}{m^2 c^4} \frac{1-\beta^2}{\beta^4} \frac{1}{Emax(\frac{\Delta E}{Emax}+sin^2\frac{\theta_0}{2})^2} \quad (4)$$

$$Emax=2E_0(E_0 + 2mc^2)/Mc^2 \quad (5)$$

$$\theta_0 = (2\pi k_0 r_0)^{-1} \quad (6)$$

E_0 is the energy of the incident electron. m is the rest mass of electron and M is the mass of the sample atom. β is ration of the velocity of incident electrons relative to speed of light. Z is the atom number.

θ_0 is a chasracteristic angle of elastic scattering where k_0 is the wavenumber of the incident electron beam and r_0 is the screening radius where r_0=$a_0 Z^{-1/3}$. a_0 is the Bohr radius which equals 0.529x10^{-10} m.

This expression is sufficiently accurate for the current purposes. For a 20nm thick anatase nanoparticle under a 200keV electron beam, the energy loss caused by elastic collisions is calculated to be 0.65J/cm^2 and 0.81 J/cm^2 for oxygen and titanium respectively. The energy transfer of approximately 1.5 J/cm^2 is negligible compared to energy transfers associate with inelastic scattering.

2. Discussion of Possible Damage Processes

The question arises about whether the amorphization that we observe is intrinsic to the hydroxylated layer or is a result of rapid electron beam damage taking place during the time required to record the high resolution image. To address this question, we make the assumption that it is possible to have an ordered hydroxylated structure on the surface of the titania. Electron beam damage to the surface during imaging can occur either through radiolysis (inelastic collisions) or knock-on processes (elastic collisions). We assume that if the energy transferred by the electron collision exceeds some fraction of the bond strength, denoted E_{min} (typical hydroxyl bond strengths are 4 – 5 eV), then

significant structural re-arrangements can occur. For knock-on damage due to elastic collisions, we can use the energy differential cross section expression in the previous section (eqn.(4)) and integrate it between E_{min} and E_{max} (given by eqn.(5)). The probability for knock-on damage is then given by eqn.(2). For an anatase crystal 20 nm in thickness, taking E_{min} to lie in the range 1 – 2.5 eV gives a probability on the order of 10^{-5} for primary collisions with hydrogen or oxygen. For damage due to ionization damage, most of the inelastic collisions result in energy transfers greater than 2.5 eV. Consequently, the energy-loss spectrum from a 10 nm crystal can be used to tells us that the probability of ionization occuring ($=I_n/I_o$) is about 0.2.

This analysis shows that the probability of damage via radiolysis is about 4 orders of magnitude higher than damage via knock-on regardless of the value of E_{min}. In reality, the surface amorphization may be triggered only by elastic or inelastic collisions with the surface layers. However, the cross section ratios for the elastic/inelastic scattering will not be very different from that calculated from the entire anatase nanocrystal. Consequently, radiolysis will be the dominant damage mechanism for surface amorphization.

The above analysis shows that the most likely source of damage occuring during imaging is due to ionization. However, if the structure can be damaged rapidly due to ionization by the electron beam, then it will almost certainly be damaged by 10 hours of UV irradiation in water. This suggests that the disorder structure that is observed by electron microscopy is not a consequence of electron irradiation but is caused by UV irradiation.

Egerton, R. F. (2011). Electron Energy-Loss Spectroscopy in the Electron Microscope, 3rd ed.; Springer; New York.

APPENDIX C

EX-SITU AND *IN-SITU* CHARACTERIZATION OF CdS ON TiO_2

CdS has been widely coupled to TiO_2 for purpose of enhancing visible light harvesting and e^- - h^+ separations. CdS/TiO_2 is an important photocatalyst system for visible light water splitting. We have prepared the CdS nanodots on TiO_2 rutile nanorods grown on transparent conductive glass-Fluorine doped Tin oxide (FTO). *Ex-situ* and *In-situ* characterizations were done on this sample.

1. Preparation of rutile TiO_2 nanorods.

Rutile TiO_2 nanorods on FTO were prepared following the hydrothermal method invented by Liu B. et al. 25 mL of deionized water was mixed with 25 mL of concentrated hydrochloric acid (36.5%-38% by weight).The 50 mL mixture was stirred for 5 mins before 1 mL of titanium butoxide (97% Aldrich) was added and stirred for another 10 mins. The mixture was then put in a 80ml volume Teflon-lined stainless steel autoclave with a 1 in by 1 in FTO glass submersed in the liquid phase but lean against the inside wall of the Teflon container. The hydrothermal synthesis was conducted at 200 ℃ for 20 hrs. After synthesis, the autoclave was cooled to room temperature before the FTO substrate is taken out. The typical morphology of the TiO_2 nanorods grown on FTO is shown in the SEM image below (Figure Appendix III.1):

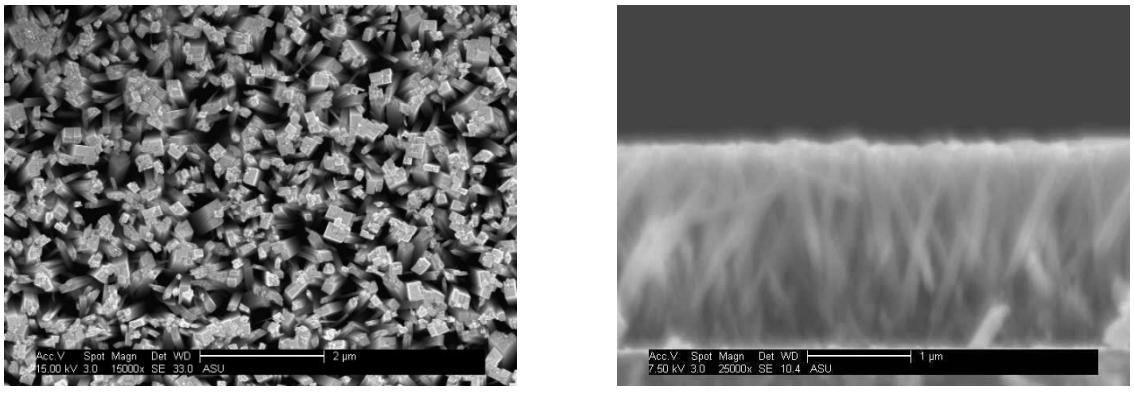

Figure Appendix C.1 SEM images of as-grown TiO_2 nanorods on FTO: (a) top view (b) side view.

2. Preparation of CdS nano dots on TiO_2 nanorods

The CdS nano dots were developed on the TiO_2 nanorods by sequential chemical bath deposition where the TiO_2 on FTO was immersed in 0.05M $Cd(NO3)_2$ aqueous solution for 30s followed by another immersion in 0.05M Na_2S aqueous solution for 30s. 30 cycles were repeated until the substrate becomes yellow. The TiO_2 on FTO glass substrate after 30 chemical bath cycles is shown in Figure Appendix III.2 a.

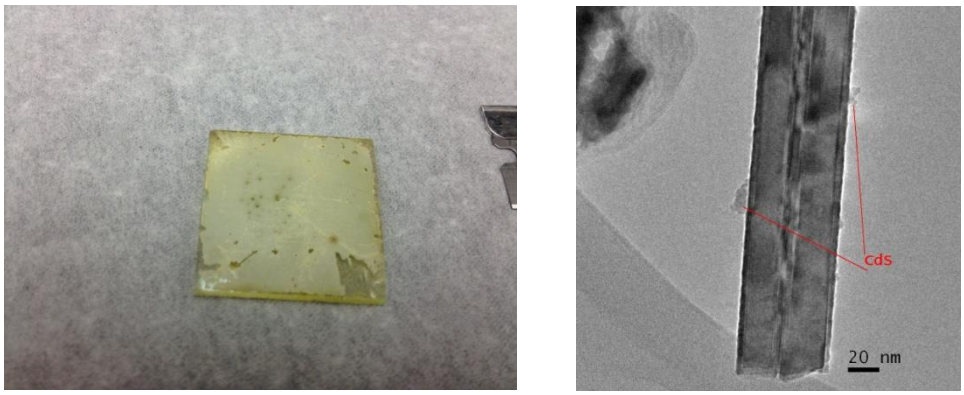

Figure Appendix C.2. (a). Photo of as-prepared CdS nano dots on TiO_2 nanorods grown on FTO. (b). TEM image of CdS on TiO2 nanorod after calcination

The sample was then calcined at 400 ºC in Ar for 3hrs. The nanorods were then scrapped off the substrate and characterized by TEM. The typical morphology of this material is shown in Figure Appendix III.2b.

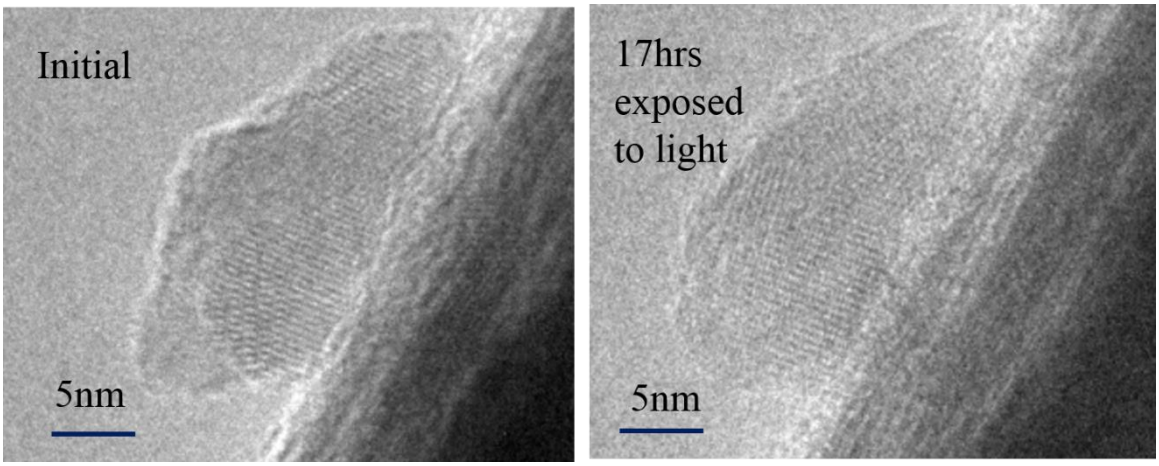

Figure Appendix C. 3. CdS on TiO_2 nanorods before and after 17hrs exposure to light and 1 Torr H_2O vapor.

Figure Appendix III. 3 shows CdS surfaces are smoothened and the aggregates become smaller after 12 hrs light exposure for the calcined CdS quantum dots on rutile TiO_2 nanorods. Besides surface smoothening CdS is wetting the TiO_2 forming a stronger interaction. Such observation is probably because light-induced e^-–h^+ pair recombination generates thermal energy for atoms to move forming new shape with minimum energy state. And the excited holes can oxidize the CdS with the reaction: $S^{2-} + 2h^+ \rightarrow S$. This is very often called the photocorrosion may also cause the reshaping of the CdS particles.

Liu, B., & Aydil, E. S. (2009). Growth of Oriented Single-Crystalline Rutile TiO_2 Nanorods on Transparent Conducting Substrates for Dye-Sensitized Solar Cells. *Journal of American Chemical Society*, 131, 3985–3990

APPENDIX D

Ag COARSENING

Some metals like Ag show properties of plasma enhanced photo absorption which help utilize solar energy when used as co-catalyst on semiconductor photocatalysts. Ag nanoparticles were sputtered on continuous carbon film TEM grids and anatase particles for study of their structural evolution in water splitting.

Figure Appendix D.1 shows the images of as-prepared Ag particles on continous carbon film TEM grid and after 8hrs UV exposure in DI water. Significant coarsening was observed after the process.

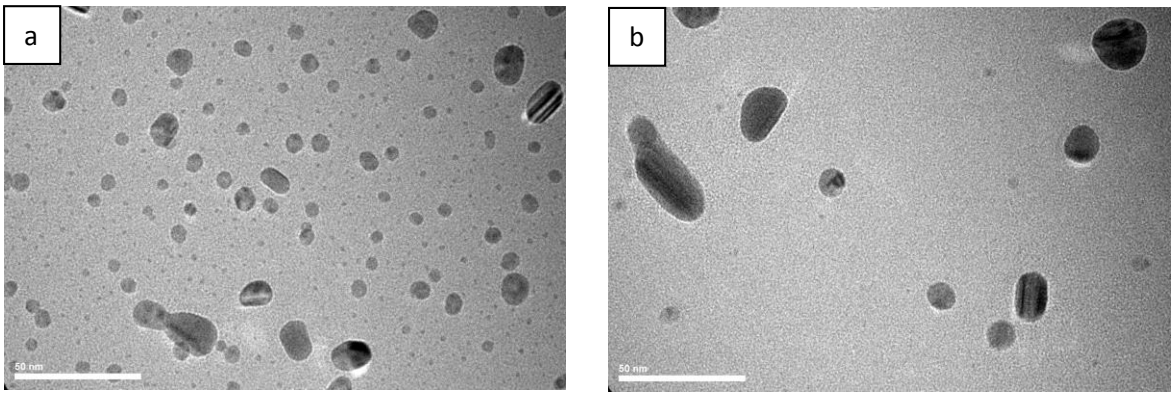

Figure Appendix D.1. (a) Initial as sputtered Ag particles on continuous carbon film (b) After 8hrs submersed in DI H_2O under UV exposure.

A control experiment was carried out on another sample prepared with the same method only exposed to 10hrs UV light but no H_2O. Resulsts are shown in Figure Appendix D.2. bellow:

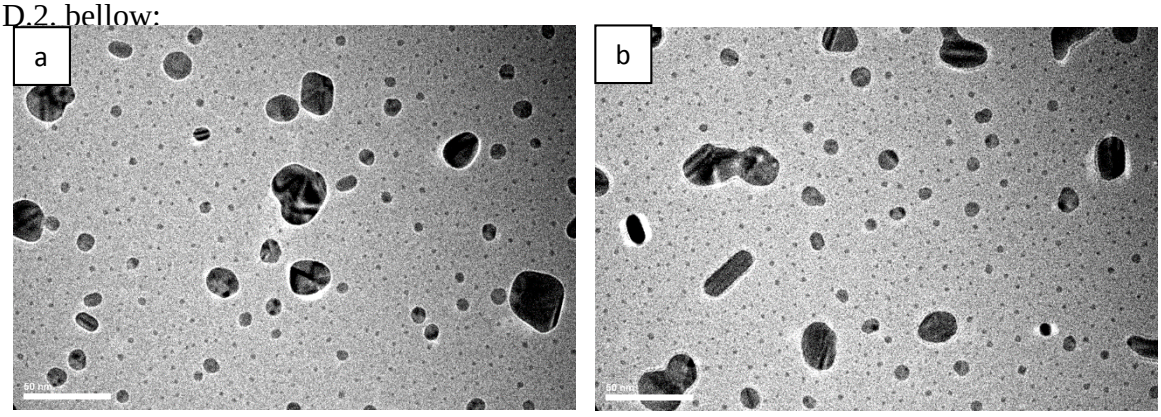

Figure Appendix D.2. (a) Initial as sputtered Ag particles on continuous carbon film (b) After 10hrs UV irradiation in air.

The TEM images of the sample after 10hrs UV irradiation without exposure to liquid water look similar to the as-prepared sample. This characterization suggests the coersening requires the persistence of H_2O. A further control experiment without light irradiation shows the coarsening does not even requires light irradiation.

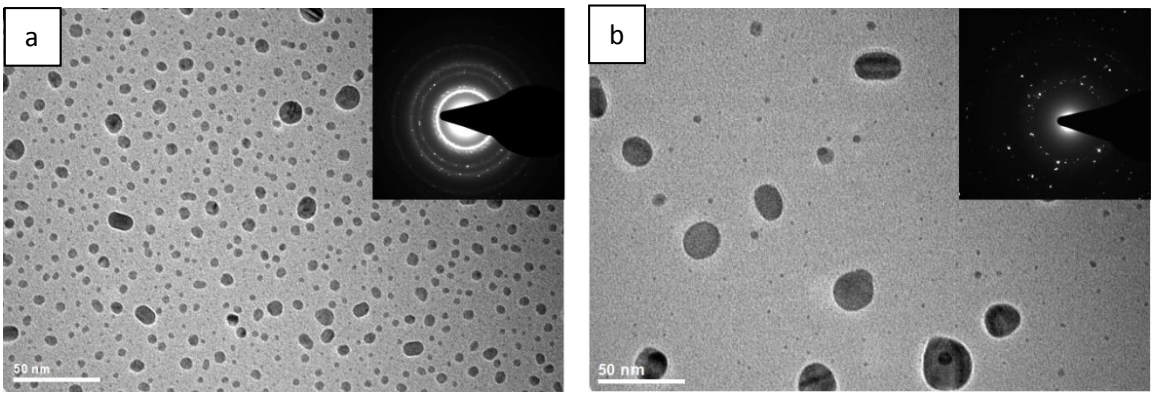

Figure Appendix D.3. (a) Initial as sputtered Ag particles on continuous carbon film (b) After 20hrs in 100% humidity and air without exposure to light. (Insets: Electron diffraction patterns)

Another as-prepared Ag on continuous carbon sample was placed on a stack of slide glass out of the liquid water in a Petri dish. The Petri dish is wrapped and sealed with aluminum foils so a 100% humidity buildup and the sample was kept in dark. The TEM after 20hrs in 100% humidity and air without light irradiation shows coarsening of Ag

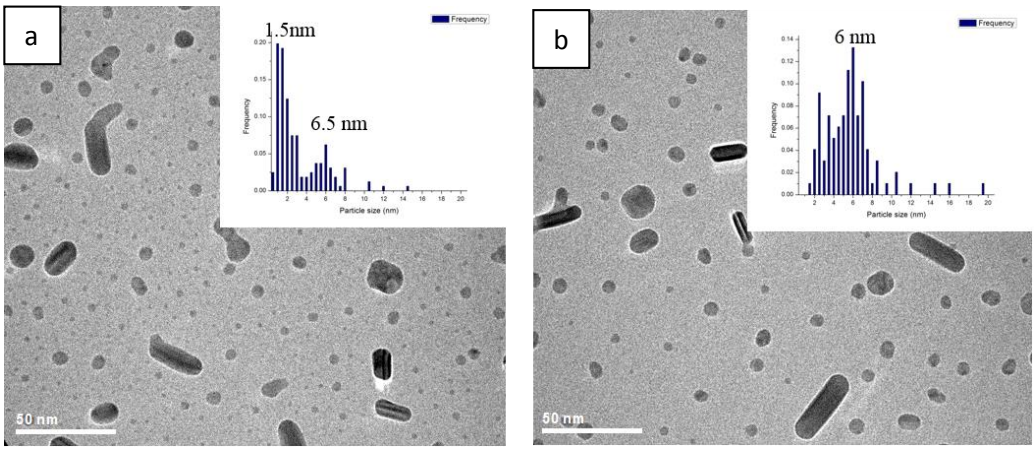

Figure Appendix D.4. (a) Initial as sputtered Ag particles on continuous carbon film (b) After 10hrs light exposure in 18 Torr water in TEM with insets particle size histograms.

particles. It suggests the coarsening of Ag on continuous carbon film does not require light irradiation nor immersion in liquid H_2O. The water vapor may have been condensed on the carbon film in a saturated sealed atmosphere. The Ag particles are connected by thin layers of H_2O molecules. When this experiment was repeated *in-situ* in the environmental TEM with 18 Torr H_2O vapor flowing, a less significant coarsening was observed shown as in Figure D. 4. This is due to much less H_2O condensation onto TEM grid under continuous flowing H_2O vapor with simultaneous pumping.

All the results shown above are consistent with the Ag particles coarsening on conductive substrate reported by Redmond, P. L.et al. The continuous carbon on TEM grid is conductive so it avoids the charging issue for TEM characterizations. Ag particle size grows when exposed to pure water through an electrochemical Ostwald ripening mechanism. The small Ag particles have larger negative potential shift due to Gibbs-Thompson effect so they are easier to be oxidized than larger Ag particles when connected by conductive carbon film. Ag is oxidized to Ag^+ at small Ag particles and transferred to large ones through liquid H_2O. The electrons were transferred through conductive carbon film from small Ag particles to large ones to maintain the charge neutral.

The Ag was also sputtered on TiO_2 anatase particles and characterized with or without light and H_2O exposure. Figure Appendix D.5 shows significant coarsening of Ag particles on anatase after 17hrs UV exposure in 100% humidity. While after 10 hrs in dark in H_2O, no significant coarsening was observed (see Figure Appendix D.6). This is consistency with what we have observed on Pt/TiO_2 where the coarsening is a photo-induced electrochemical Ostwald ripening.

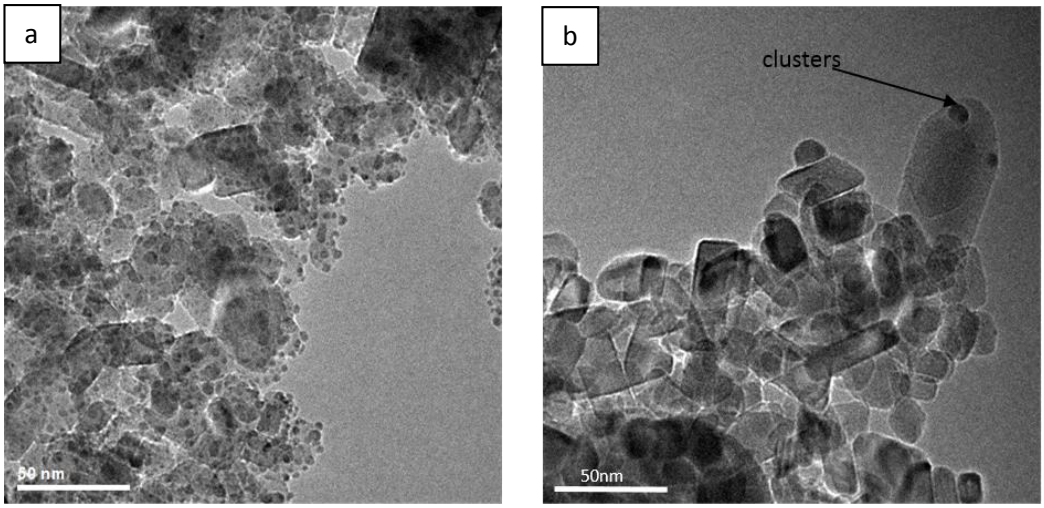

Figure Appendix D.5. (a) As sputtered Ag particles on anatase; (b) After 7hrs exposure to UV light in 100% humidity

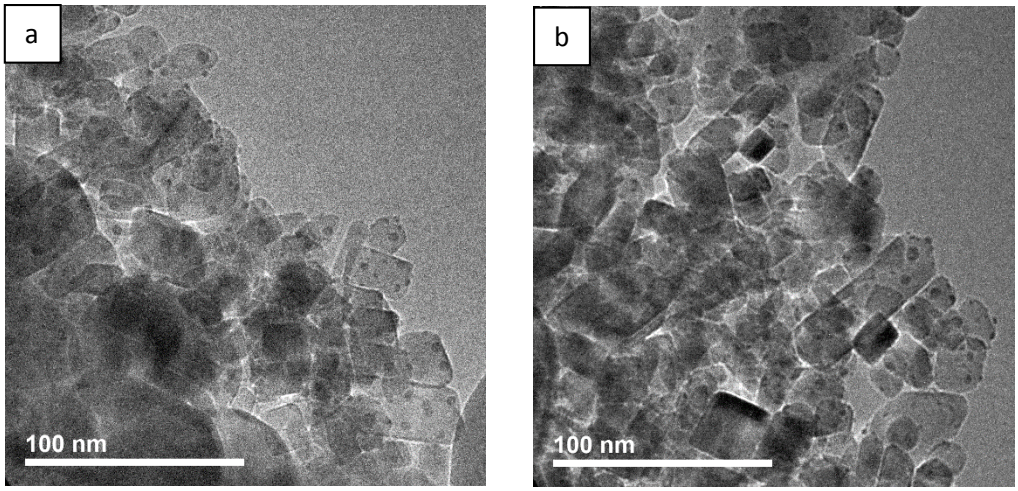

Figure Appendix D.6. (a) As sputtered Ag particles on anatase; (b) After 10hrs in liquid H_2O in dark.

Another discovery is Ag is very sensitive to the contaminants in air. Analysis using electron diffraction found the as prepared sample was fcc Ag metal while the coarsened Ag particles show diffraction patterns of bcc AgS. There was a sewer gas leaking problem in the building of our lab. The AgS may result from the reaction of Ag with H_2S in the sewer gas. The experiments on Ag coarsening have to be carried out in a controlled atmosphere.

Redmond, P. L.; Hallock, A. J.; Brus, L. E. Electrochemical Ostwald Ripening of Colloidal Ag Particles on Conductive Substrates. *Nano Lett*. **2005**, 5(1), 131-135.

APPENDIX E

GRAPHENE LIQUID CELL

Yuk et al invents the method to prepare graphene liquid cell using two layers of graphene film to trap liquid in between directly on TEM. Wang et al has expanded this technique to study ferritin in graphene liquid cells. We followed Wang's method which is written in details in the supplemental material of his paper. Some of the preliminary results have been obtained.

Figure Appendix E.1 shows a liquid cell before and after exposure to focused electron beam. Bubbles appear during electron irradiation which is a typical sign of H_2O presence between the graphene sheets. As shown in Figure Appendix E.2, EELS acquired from the liquid cell shows O K-edge peaks further confirming the presence of H_2O. However, even though liquid cells were successfully prepared, the reproducibility is very low. And the liquid cells always contain Fe, Cu and Cl ions from the copper etchant used for preparation of free floating graphene films which causes unwanted contaminations. Efforts are being made to increase the success rate and minimize the contamination.

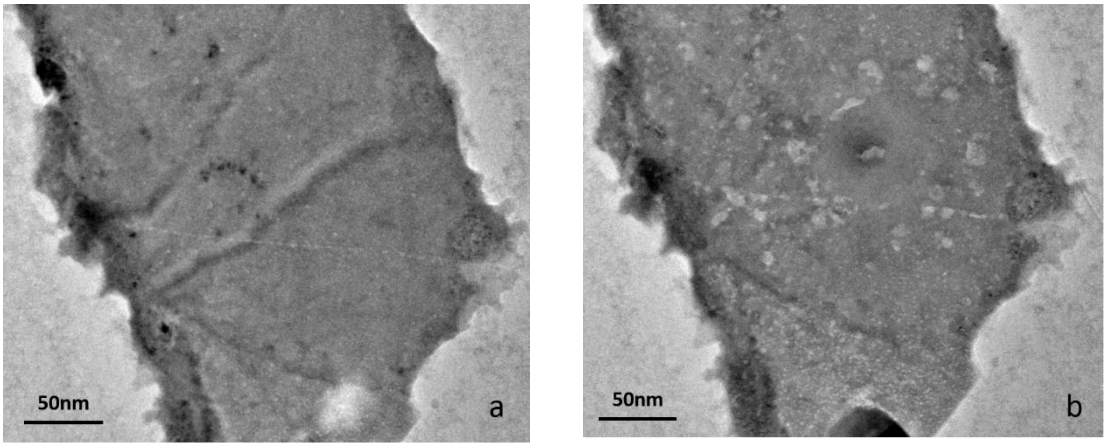

Figure Appendix E.1 Graphene liquid cell a) before focused electron beam; b) after focused electron beam.

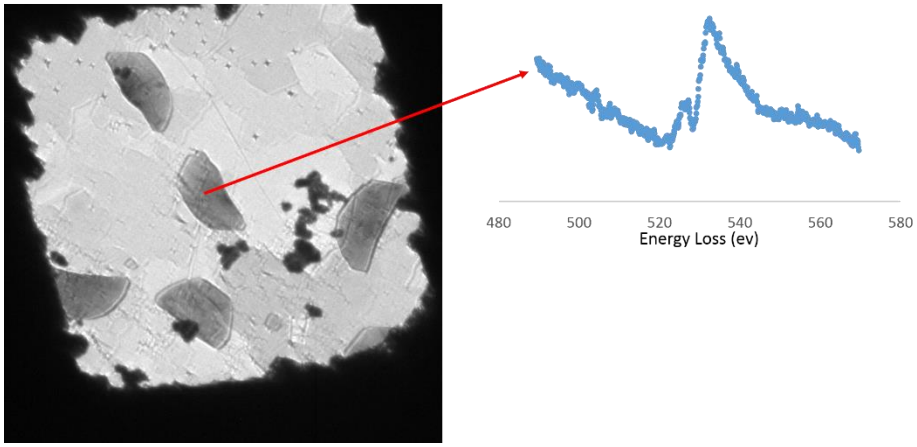

Figure Appendix E.2 EELS taken on liquid cell show O-K edge peaks

Yuk, J.M., Park, J., Ercius, P., Kim, K., Hellebusch, D.J., Crommie, M.F., Lee, J.Y., Zettl, A.& Alivisatos, A.P. (2012), High-Resolution EM of colloidal nanocrystal growth using graphene liquid cells, *Science*,336(6077), 61-64.

Wang, C., Qiao, Q., Shokuhfar, T. & Klie, R. F. (2014). High-Resolution electron microscopy and spectroscopy of ferritin in biocompatible graphene liquid cells and graphene sandwiches. *Advanced Materials*, 2, 3410–3414

APPENDIX F

PRELIMINARY DATA OF TiO_2 LOCAL BANDGAP AND SURFACE STATES

The average measured value of TiO_2 (High Purity) bandgap from more than 6 different spectra is 3.60 eV $\pm$0.01 eV. Figure Appendix F.1a insertion shows an example of how the bandgap is measured by extrapolating the straight portion of the fitted curve to the x axis. 3.60 eV, which may be the direct bandgap measurement, is larger than the well-known ~3.2 eV indirect bandgap for anatase achieved from optical measurements. Figure Appendix F.1a also shows the bandgap of anatase shifts to 3.71 $\pm$0.03 eV as the Ti in the particle was reduced from Ti^{+4} to Ti^{+3} by the electron beam. Here beam-sample interaction was used to reveal bandgap structure change as the oxidation state of the material changed. On Figure Appendix F.1b, inter-band states were clearly observed when beam was on the surfaces of TiO_2 on Ni/TiO_2 (Low Purity) samples. Distinctive interstates peaks were at 2.08 eV, 2.37 eV and 2.85 eV for TiO_2.Those states are believed to be related to the oxygen vacancies produced from the high temperature reduction and/or impurities segregated to surfaces in the commercial TiO_2 after high temperature heat treatment. The energies of these inter-band states vary among different particles depending on their local morphology and impurity concentrations. Theoretical simulations are being carried out to interpret the experimental data.

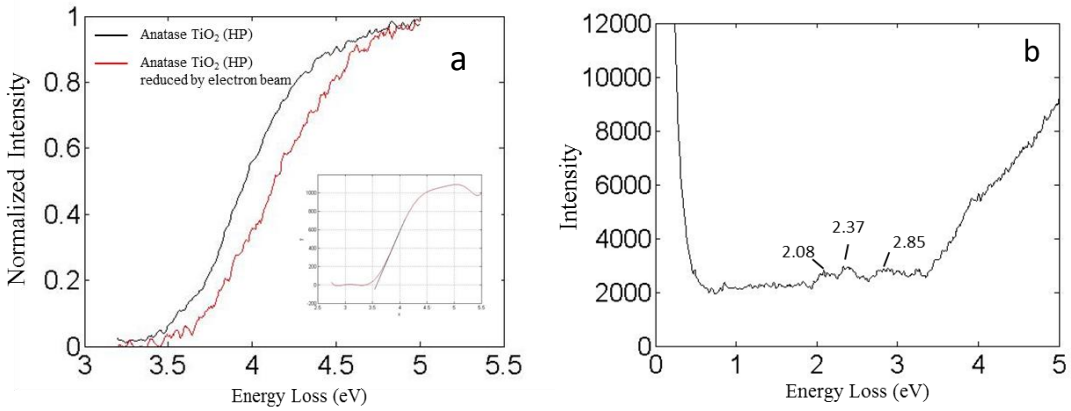

Figure Appendix F.1 a) Bandgap edge from anatase TiO_2 (HP) before and after reduction by electron beam with insertion of curve fitting as example of how the bandgap is measured. b) Inter-band states on surface of TiO_2 from Ni/TiO_2 (LP)